

Chapter 3

Radioactivities in Low- and Intermediate-Mass Stars

Maria Lugaro¹ and Alessandro Chieffi²

Energy in stars is provided by nuclear reactions, which, in many cases, produce radioactive nuclei. When stable nuclei are irradiated by a flux of protons or neutrons, capture reactions push stable matter out of stability into the regime of unstable species. The ongoing production of radioactive nuclei in the deep interior of the Sun via proton-capture reactions is recorded by neutrinos emitted during radioactive decay. These neutrinos escape the inner region of the Sun and can be detected on Earth. Radioactive nuclei that have relatively long half lives may also be detected in stars via spectroscopic observations and in stardust recovered from primitive meteorites via laboratory analysis. The vast majority of these stardust grains originated from Asymptotic Giant Branch (AGB) stars. This is the final phase in the evolution of stars initially less massive than $\simeq 10 M_{\odot}$, during which nuclear energy is produced by alternate hydrogen and helium burning in shells above the core. The long-lived radioactive nucleus ^{26}Al is produced in AGB stars by proton captures at relatively high temperatures, above 60 MK. Efficient production of ^{26}Al occurs in massive AGB stars ($> 4 : 5 M_{\odot}$), where the base of the convective envelope reaches such temperatures. Several other long-lived radioactive nuclei, including ^{60}Fe , ^{87}Rb , and ^{99}Tc , are produced in AGB stars when matter is exposed to a significant neutron flux leading to the synthesis of elements heavier than iron. Here, neutron captures occur on a timescale that is typically slower than β -decay timescales, resulting in a process known as *slow* neutron captures (the *s*-process). However, when radioactive nuclei with half lives greater than a few days are produced, depending on the temperature and the neutron density, they may either decay or capture a neutron, thus branching up the path of neutron captures and defining the final *s*-process abundance distribution. The effect of these *branching points* is observable in the composition of AGB stars and stardust. This nucleosynthesis in AGB stars could produce some long-living radioactive nuclei in relative abundances that resemble those observed in the early solar system.

¹ Monash University, Victoria 3800, Australia

² I.N.A.F., 00133 Roma, Italy

3.1 The Missing Element

The element with 43 protons in its nucleus, lying between molybdenum and ruthenium, was known for a long time as the *missing* element. Since the 19th century there had been many unsuccessful attempts at its discovery. Finally, in 1937 Italian physicist Emilio Segré and chemist Carlo Perrier found two isotopes of the missing element through measurements of radioactivity from discarded cyclotron parts: they observed several decay periods and proved they were occurring at $Z=43$. Hence the missing element did not exist in nature because of its instability against nuclear decay. The discoverers named the missing element technetium (Tc), from $\tau\epsilon\chi\nu\eta\tau\acute{o}\varsigma$, which means artificial in Greek, since it was the first element produced artificially. Fifteen years later, it was shown that Tc is not only made by men but also by stars. In 1952, astronomer Paul Merrill observed the absorption lines corresponding to the atomic structure of Tc in the spectra of several giant stars. Merrill was at first cautious about this result. To start with, the element he identified did not even exist on Earth. Second, up to then it was assumed, and not proved wrong, that all stars had the same chemical composition. This was in agreement with the accepted theory of the time that the elements were all produced during the Big Bang and their abundances in the Universe were not modified by any further process. Merrill's discovery in that respect was truly revolutionary: given the relatively short half lives of the Tc isotopes (a few Myrs at most), the Tc lines were the first indisputable demonstration that this radioactive element was made *in situ* in the stars where it was observed. This finding brought a radical change in the way we understand the origin of the elements, and the theory of stellar nucleosynthesis introduced in Chapter 2 began to take shape and garnered authority. In this chapter we discuss the life of those stars that, like our Sun, evolve twice through Red Giant stages. We describe how they produce long lived radioactive nuclei, like Tc, in their interiors, how the signature of such radioactivity is carried outside the star, and how it can be observed.

3.2 The Production of Radioactive Nuclei in Stellar Interiors

In Subsection 3.2.1 we first derive the four basic equations that control the quasi-equilibrium configuration of a self-gravitating gas sphere, namely, the hydrostatic equilibrium equation (that describes the balance between the pressure gradient and gravity) and the energy transport equation (due to photons and/or convection), plus the two associated continuity equations for mass and energy flux. Then, we show that energy losses, which occur mainly from the stellar surface in stars of mass less than $\sim 10 M_{\odot}$, force the gas to contract and to heat, in accordance with the virial theorem. The progressive increase of the central temperature allows the activation of nuclear processes and we describe two sequences that convert protons into ${}^4\text{He}$ nuclei (α particles): the PP chain and the CNO cycle. Since proton capture inevitably pushes matter out of the stability, both these sequences produce radioactive nuclei that decay by emitting neutrinos.

In Subsection 3.2.2 we briefly describe the quest for solar neutrinos and the various experiments that eventually allowed the demonstration that the lower than predicted neutrino flux from the Sun (the so-called Solar Neutrino Problem) is the consequence of neutrino oscillations among their three different flavors.

3.2.1 The Stellar Energy Source and Radioactive Isotopes

A star is, in first approximation, a spherically symmetric, gaseous cloud contracting under its own gravity and progressively heating up while losing energy from its surface in the form of photons. A strong temperature gradient, with the temperature decreasing from the centre to the surface, pushes the photon flux outward until the *mean free path*³ of the photons eventually becomes larger than their distance from the surface, allowing their escape. The Virial theorem links the energy gained by the gravitational field $\Delta\Omega$ to that absorbed by the gas ΔU : $\Delta U = -\Delta\Omega/3(\gamma - 1)$, where γ is the ratio between two specific heats, that at constant pressure and that at constant volume, of the contracting gas. A stable quasi-equilibrium configuration exists for such a structure provided that $\gamma > 4/3$. In this case, a fraction of the energy gained by the gravitational field must be liberated from the structure before the gas cloud can contract further. In the case of a perfect gas ($\gamma = 5/3$) we obtain the classical result $\Delta U = -(1/2)\Delta\Omega$, stating that half of the gravitational energy liberated by each infinitesimal contraction is absorbed by the gas and half must be lost before an additional contraction can occur. The timescale over which the energy is lost from the system drives the timescale of contraction and keeps the structure in a quasi-equilibrium configuration. If, instead, γ drops to $4/3$, all the gravitational energy is absorbed by the gas and no time delay is required before a new contraction can occur. This is an unstable situation leading to collapse. In the evolutionary phases we discuss in this chapter γ remains well above $4/3$ and hence a stable quasi-equilibrium configuration is always assured.

The balancing forces required to maintain a stable stellar quasi-equilibrium configuration are due to pressure gradients and gravity. So, the first main equation of stellar structure describes the equilibrium between these two forces, at any given distance from the center of the star r :

$$dP/dr = -GM\rho/r^2 \quad (3.1)$$

where P is the pressure, G the gravitational constant, M the cumulative mass inside r , and ρ the density. Associated to this equation is a continuity equation for mass:

³ The average distance a particle travels between collisions.

$$dM/dr = 4\pi r^2 \rho. \quad (3.2)$$

By assuming, to zero order, that ρ is constant within the star, the integration of eq. 3.2 implies that:

$$\rho \propto M/R^3 \quad (3.3)$$

Since the pressure at the surface of the star is much lower than where the radius approaches zero, the center of the star, the equation of hydrostatic equilibrium, 3.1, basically says that

$$P_c \propto M\rho/R_s \quad (3.4)$$

where P_c is the central pressure and R_s the stellar radius. By inserting the relation 3.3 into 3.4 one obtains:

$$P_c \propto M^2/R_s^4 \quad (3.5)$$

If the equation of state is that of a perfect gas, i.e. $P \propto \rho T/\mu$, relation 3.5 becomes:

$$T_c \propto \mu M/R \quad (3.6)$$

where T is the temperature and μ is the mean molecular weight. This equation provides an important basic relationship among central temperature (T_c), mass, and radius of a star, which only relies on the assumption of hydrostatic equilibrium.

The second major equation describing the structure of the quasi-equilibrium configuration of a star determines the energy flux through the structure. In stationary situations the energy is transported by photons or electrons and application of the first Fick's law leads to the well known equation:

$$dT/dr = -3\kappa\rho L/(16ac\pi r^2 T^3) \quad (3.7)$$

where κ is the opacity coefficient representing the impenetrability of a gas to light, L the luminosity representing the amount of energy radiated per unit time, a the radiation constant, and c the speed of light. Furthermore, in this case a continuity equation

$$dL/dr = 4\pi r^2 \rho \varepsilon \quad (3.8)$$

controls the conservation of energy, where ε represents the net local energy budget, i.e., the sum of the nuclear energy production rate ε_{nuc} , the neutrino energy loss rate ε_{ν} , and the gravitational energy rate ε_g . Since the central temperature T_c is much higher than the surface temperature, it is possible to obtain a basic relationship between central temperature, mass, luminosity and radius of a star, i.e.:

$$T_c^4 \propto ML/R^4 \quad (3.9)$$

By combining this relation with the previous relation 3.6, derived from hydrostatic equilibrium 3.1, one eventually obtains the fundamental relation between mass and luminosity:

$$L \propto \mu^4 M^3 \quad (3.10)$$

Frequently, the energy produced locally cannot be transported quickly enough by radiation or conduction, and interior shells formally in an equilibrium condition can become unstable in the sense that a displacement from their equilibrium position is not fully counteracted by a restoring force. Instead, matter is accelerated even further from its original position and large scale motions of matter (*convection*) is established. Under these conditions energy is predominantly transported by buoyancy-driven motions of bulk material due to their much larger mean free path with respect to that of photons. A temperature gradient quite different from that described by equation 3.7 must then be used in these regions. A direct consequence of these large scale motions is that matter is mixed throughout an unstable region.

The system formed by the two basic equations related to hydrostatic equilibrium and energy transport plus the two associated continuity equations and the equation of state (supplemented by an opacity coefficient $\kappa = f'(\rho, T, \text{chem.comp.})$ and a total energy generation coefficient $\varepsilon = f(\rho, T, \text{chem.comp.})$) constitutes the basic set of equations that describes the internal structure of a quasi-equilibrium (non rotating) stellar configuration at a given time. The temporal evolution of such a structure is determined by the rate at which energy is lost to the surroundings: the faster the energy is lost, the faster the structure evolves. Typical stellar luminosities range between $\sim 4 \times 10^{33}$ erg/s for a star of $1 M_{\odot}$ and $\sim 4 \times 10^{36}$ erg/s for a star of $6 M_{\odot}$ and the associated lifetimes can be estimated by dividing the total amount of available energy by the loss rate L , i.e. the stellar luminosity. If the only energy source was the gravitational field, the lifetime of a contracting gas cloud would be of the order of a few tens of millions of years (the Kelvin-Helmholtz timescale). Instead, as was known since the 1920s from radioactive dating of terrestrial rocks, that the age of the Earth is several Gyrs, much longer than the Kelvin-Helmholtz

timescale. Thus, the Sun must be powered by different means. The lifetime of most stars is much larger than permitted by their gravitational energy reservoir alone. Instead of simple contraction, energy losses are replaced by the activation of nuclear fusion reactions among charged nuclear particles near the stellar core.

The efficiency of nuclear reactions, i.e., their *rate*, depends on the abundances of the reactant nuclei and the cross section of each reaction averaged over a Maxwellian distribution of relative velocities between the target and the projectile nuclei. For charged particle reactions the rate is mainly controlled by the Coulomb barrier generated by the number of protons in a nucleus. The nuclear reactions that activate at the lowest temperatures are those involving capture of protons, i.e., the nucleus of the lightest and most abundant element: hydrogen (H). Nature, however, does not allow the build up of stable nuclei made only of protons because in order to glue nucleons (i.e., proton and neutrons) together in a nucleus via the strong nuclear force, the repulsive electromagnetic force acting between protons needs to be diluted with a certain number of neutrons. The distribution of stable nuclei in the [N=number of neutrons, Z=number of protons] plane, the *chart of nuclides*, clearly shows that the region where nuclei are stable lies close to the N=Z line (the *valley of β stability*) up to the element Ca, and then bends slightly towards the neutron-rich side as the repulsion between higher number of protons needs to be diluted with more and more neutrons. Nuclei outside this valley are radioactive, i.e., unstable, and decay towards their closest stable daughter through β -decay weak interaction reactions (as described in Chapters 1, 2, 4, and 9). It follows that the build up of progressively heavier nuclei through the addition of protons naturally pushes the matter out of the stability valley, producing radioactive nuclei that decay back towards stability via β^+ decay.

A detailed analysis of the nuclear reactions involving the fusion of protons (H burning) foresees the existence of two processes. The PP chain activates at temperatures $\simeq 10$ MK and operates through a sequence of proton captures and β decays starting with a weak interaction p+p fusion. The processes involved in the PP chain are listed in Table 3.1 together with the mass defect (Q_{tot} values) in MeV and the energy carried away by neutrinos (Q_ν). If the neutrino emission is described by an energy continuum, the maximum energy of this spectrum is reported. A direct build up of progressively heavier nuclei through successive proton captures stops very early, at ^3He , because of the low cross section of the $^3\text{He}+\text{p}$ reaction. Also, proton captures on the second most abundant isotope, ^4He (or α particle, $N = Z = 2$), cannot even begin, because nuclei with atomic mass number $A = N+Z = 5$ do not exist.⁴ In order to proceed with proton captures beyond ^3He it is necessary to build up enough ^3He nuclei to activate the capture of this nucleus by either another ^3He nucleus, or ^4He . The activation of ^3He captures allows to overcome the non-existence of nuclei with $A=5$, though it still does not allow the build up of an appreciable amount of nuclei heavier than He. In fact, the product of the $^3\text{He}+^3\text{He}$ reaction is an α particle plus two protons, while the product of the $^3\text{He}+^4\text{He}$ reaction is ^7Be , whose fate, either proton or electron capture leads to the formation of ^8Be , which very quickly de-

⁴ Their half lives are of the order of 10^{-22} s.

cays in two α particles. In synthesis, the fusion of H mainly produces He, together with a number of radioactive nuclei that decay into their respective stable daughter nuclei emitting a neutrino. The energies and the number of neutrinos produced in these decays reflect the relative importance of the various PP-chain branches and the efficiency of the nuclear reactions in stars.

Table 3.1 The PP chain

reaction	Q_{tot} (MeV)	Q_ν (MeV)
$p + p \rightarrow d + e^+ + \nu$	1.442	0.42(spectrum)
$d + p \rightarrow {}^3\text{He}$	5.494	
${}^3\text{He} + {}^3\text{He} \rightarrow {}^4\text{He} + 2p$	12.860	
${}^3\text{He} + {}^4\text{He} \rightarrow {}^7\text{Be}$	1.587	
${}^7\text{Be} + e^- \rightarrow {}^7\text{Li} + e^+ + \nu$	0.862	0.861(90%)-0.383(10%) (lines)
${}^7\text{Be} + p \rightarrow {}^8\text{B} \rightarrow {}^8\text{Be} + e^+ + \nu \rightarrow \alpha + \alpha$	18.209	14.060(spectrum)
${}^7\text{Li} + p \rightarrow {}^8\text{Be} \rightarrow \alpha + \alpha$	17.347	

The second process converting protons to α particles is the CNO cycle. Given the high Coulomb barrier of the CNO nuclei, this cycle becomes efficient at temperatures ($T > 20$ MK), significantly higher than those relevant to the PP chain. The main section of this sequence is characterized by the continuous conversion of C to N and viceversa. Let us start, e.g., with the capture of a proton by a ${}^{12}\text{C}$ (Table 3.2). The outcome of this fusion is the radioactive nuclide ${}^{13}\text{N}$ that quickly decays β^+ into ${}^{13}\text{C}$. Efficient proton captures by ${}^{13}\text{C}$ lead to the synthesis of ${}^{14}\text{N}$. Proton captures by ${}^{14}\text{N}$ produce ${}^{15}\text{O}$, a radioactive nuclide that quickly decays in ${}^{15}\text{N}$. The fusion of a proton and a ${}^{15}\text{N}$ particle has, as the main outcome, a ${}^{12}\text{C}$ nucleus plus an α particle. The sequence sketched above is called the CN cycle. If the temperature exceeds $T \sim 25 - 30$ MK, also oxygen enters the game and the full CNO cycle activates: ${}^{16}\text{O}$ begins to capture protons forming radioactive ${}^{17}\text{F}$ that decays to ${}^{17}\text{O}$. The capture of a proton by this particle leads to a compound nucleus that preferentially splits into ${}^{14}\text{N}$ and an α particle, and that partly turns into ${}^{18}\text{F}$, which quickly decays to ${}^{18}\text{O}$. Proton captures on ${}^{18}\text{O}$ produce preferentially ${}^{15}\text{N}$ plus an α particle. The activation of the channel ${}^{15}\text{N}(p,\gamma){}^{16}\text{O}$ closes the NO cycle, processing material back into oxygen. The total abundance by number of the CNO isotopes remains constant with time because the proton capture on any of them (and the subsequent β^+ decays) just produce another isotope in the same set.

For $T > 25 - 30$ MK, the full CNO cycle becomes efficient and quickly reaches a quasi-equilibrium in which the abundance of each nucleus settles on a steady state value determined by the balance between its production and destruction. For example, the equilibrium abundance of ${}^{13}\text{C}$ (assuming that ${}^{13}\text{N}$ decays instantaneously) is given by:

$$\frac{dY_{13\text{C}}}{dt} = Y_{12\text{C}} Y_p \rho N_A \langle \sigma v \rangle_{12\text{C}+p} - Y_{13\text{C}} Y_p \rho N_A \langle \sigma v \rangle_{13\text{C}+p} = 0$$

Table 3.2 The CNO cycle

reaction	Q_{tot} (MeV)
$^{12}\text{C} + p \rightarrow ^{13}\text{N}$	1.944
$^{13}\text{N} \rightarrow ^{13}\text{C} + e^+ + \nu$	2.220
$^{13}\text{C} + p \rightarrow ^{14}\text{N}$	7.551
$^{14}\text{N} + p \rightarrow ^{15}\text{O}$	7.297
$^{15}\text{O} \rightarrow ^{15}\text{N} + e^+ + \nu$	2.754
$^{15}\text{N} + p \rightarrow ^{12}\text{C} + \alpha$	4.966
$^{15}\text{N} + p \rightarrow ^{16}\text{O}$	12.127
$^{16}\text{O} + p \rightarrow ^{17}\text{F}$	0.600
$^{17}\text{F} \rightarrow ^{17}\text{O} + e^+ + \nu$	2.761
$^{17}\text{O} + p \rightarrow ^{14}\text{N} + \alpha$	1.192
$^{17}\text{O} + p \rightarrow ^{18}\text{F}$	5.607
$^{18}\text{F} \rightarrow ^{18}\text{O} + e^+ + \nu$	1.656
$^{18}\text{O} + p \rightarrow ^{15}\text{N} + \alpha$	3.981
$^{18}\text{O} + p \rightarrow ^{19}\text{F}$	7.994

where Y_i refers to the abundance by number of a given species i , t is time, ρ is the density, N_A is Avogadro's number and $\langle \sigma v \rangle_{i+j}$ is the Maxwellian averaged product of the velocity v times the nuclear cross section σ for a given reaction between nuclei i and j . The equilibrium condition immediately gives:

$$\frac{Y_{^{12}\text{C}}}{Y_{^{13}\text{C}}} = \frac{\langle \sigma v \rangle_{^{13}\text{C}+p}}{\langle \sigma v \rangle_{^{12}\text{C}+p}}$$

which means that the relative abundances between isotopes of the CNO cycle depend only on the ratio between the respective cross sections for proton capture. Typical isotopic and elemental ratios obtained in the temperature range $30 \leq T \leq 100$ MK are reported in Table 3.3.

Table 3.3 Typical isotopic ratios from CNO cycling

isotopic ratio	value	solar value
$Y_{^{12}\text{C}}/Y_{^{13}\text{C}}$	$\simeq 4$	89
$Y_{^{14}\text{N}}/Y_{^{15}\text{N}}$	$\simeq 4 \times 10^4 - 10^5$	272
$Y_{^{17}\text{O}}/Y_{^{16}\text{O}}$	$\simeq 10^{-2} - 10^{-3}$	3.8×10^{-4}
$Y_{\text{C}}/Y_{\text{N}}$	$\simeq 7 \times 10^{-3} - 2.5 \times 10^{-2}$	3.2
$Y_{\text{N}}/Y_{\text{O}}$	$\simeq 60 - 350$	0.13
$Y_{^{18}\text{O}}/Y_{^{16}\text{O}}$	$\simeq 2 \times 10^{-6}$ for $T < 50 : 60 \text{ MK}$	2×10^{-3}
$Y_{^{18}\text{O}}/Y_{^{16}\text{O}}$	declines to $\simeq 5 \times 10^{-8}$ at $T \simeq 100 \text{ MK}$	2×10^{-3}

The neutrinos emitted by the decay of radioactive nuclei synthesized by the CNO cycle have characteristic energies different from those emitted by the PP chain. Their detection would provide precious information about the relative efficiency of the various reactions involved in the CNO cycle.

In addition to the PP chain and the CNO cycle there is another sequence of proton captures that can become efficient in stars, although it does not play a role in the energy budget. In the temperature range 40-50 MK the proton captures listed in the upper part of Table 3.4 quickly bring to their equilibrium values the abundances of ^{20}Ne , ^{21}Ne , ^{22}Ne , and ^{23}Na , forming also in this case a *NeNa* cycle. For temperature in excess of 50 MK the $^{23}\text{Na}(p,\gamma)^{24}\text{Mg}$ channel competes with the $^{23}\text{Na}(p,\alpha)^{20}\text{Ne}$ so that matter from the NeNa cycle leaks towards more massive nuclei. At temperatures of order of 60 MK also the proton captures listed in the lower part of Table 3.4 fully activate so that all the nuclei between ^{20}Ne and ^{27}Al reach their equilibrium abundances. Is it worth noting that ^{26}Al , a long-lived radioactive nucleus with half life $7.17 \cdot 10^5$ yr, is included within this sequence. ^{26}Al can be ejected into the interstellar medium by stellar outflows (winds) and its decay into ^{26}Mg can be detected as diffuse γ -ray emission (Chapter 7, Section 4) when the metastable ^{26}Mg relaxes towards its ground state. Moreover, it can be included in dust grains that form around stars and decay within the already formed minerals. This nucleus is thoroughly discussed in Section 3.6.1, Chapter 7 Section 4, and Chapters 4 and 9. Typical $Y_{26\text{Al}}/Y_{27\text{Al}}$ equilibrium ratios produced by H burning range between $3 \cdot 10^{-2}$ at 60 MK and 0.8 at 100 MK. We refer the reader to the book by Cox and Giuli (1968) for a derivation of the basic stellar structure equations and detailed discussions of the physics involved in the study of stellar evolution.

Table 3.4 The NeNaMgAl sequence

reaction	Q_{rot} (MeV)
$^{20}\text{Ne} + p \rightarrow ^{21}\text{Na}$	5.979
$^{21}\text{Na} \rightarrow ^{21}\text{Ne} + e^+ + \nu$	3.548
$^{21}\text{Ne} + p \rightarrow ^{22}\text{Na}$	6.739
$^{22}\text{Na} \rightarrow ^{22}\text{Ne} + e^+ + \nu$	2.842
$^{22}\text{Ne} + p \rightarrow ^{23}\text{Na}$	8.794
$^{23}\text{Na} + p \rightarrow ^{20}\text{Ne} + \alpha$	2.377
$^{23}\text{Na} + p \rightarrow ^{24}\text{Mg}$	11.693
$^{24}\text{Mg} + p \rightarrow ^{25}\text{Al}$	6.548
$^{25}\text{Al} \rightarrow ^{25}\text{Mg} + e^+ + \nu$	4.277
$^{25}\text{Mg} + p \rightarrow ^{26}\text{Al}$	6.307
$^{26}\text{Al} \rightarrow ^{26}\text{Mg} + e^+ + \nu$	4.004
$^{26}\text{Al} + p \rightarrow ^{27}\text{Si}$	12.275
$^{26}\text{Mg} + p \rightarrow ^{27}\text{Al}$	8.271
$^{27}\text{Si} \rightarrow ^{27}\text{Al} + e^+ + \nu$	4.812
$^{27}\text{Al} + p \rightarrow ^{28}\text{Si}$	11.585
$^{27}\text{Al} + p \rightarrow ^{24}\text{Mg} + \alpha$	1.601

Although the sequences of nuclear reactions that power stellar luminosity are now considered to be well understood, a wise Galilean approach suggests to verify experimentally (whenever possible) their occurrence in stars. Our Sun provides a unique opportunity to accomplish such verification via the detection of neutrinos produced by radioactive decay in its deep interior.

3.2.2 Solar Neutrinos – a Unique Opportunity

The long-term stability of characteristic solar properties, in particular its luminosity and surface temperature, can be explained only if the solar energy source is of nuclear origin and specifically involves proton captures, which are associated with abundant fuel and a long time scale. As discussed above, such an energy source inevitably results in the production of radioactive nuclei, which decay into their stable daughter nuclei through weak processes, hence emitting neutrinos. Modeling of the internal structure of the Sun predicts a central temperature at present of about 15 MK, and hence that the PP chain dominates (99.6%) over the CNO cycle (0.4%) converting H into ^4He . The relative importance of the nuclear reactions in the PP chain in the Sun leads to the result that the majority (93%) of the neutrinos produced should come from $p(p, e^+ \nu_e) d$ reactions (where d =deuterium, $N=Z=1$) and be of relatively low energy ($E \leq 0.42$ MeV, see Table 3.1), while only a minor fraction of the total neutrino spectrum is expected to be contributed by the decay of ^7Be ($\simeq 7\%$, $E \simeq 0.86$ MeV) and ^8B (0.0075%, $E < 15$ MeV).

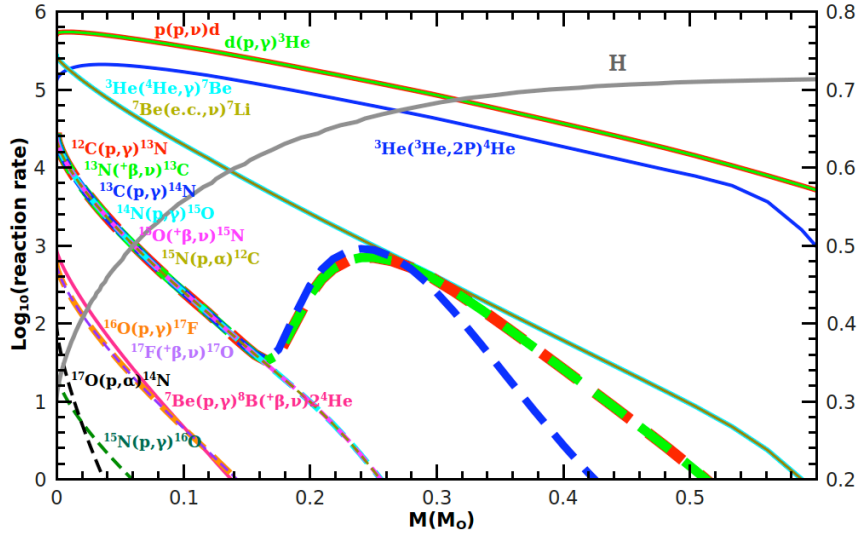


Fig. 3.1 Rates of the reactions involved in the PP chain and the CNO cycle as a function of the mass coordinate in a solar-like stellar model having approximately the age of the Sun of 4.6 Gyr. The H abundance is also plotted and its range shown on the right-side y-axis.

Figure 3.1 shows the rates of the nuclear reactions involved in the PP chain and CNO cycle as a function of the mass coordinate for a $1 M_{\odot}$ stellar model of solar

*metallicity*⁵ and an age close to the present age of the Sun, i.e., 4.6 Gyr. All the β^+ decays are concentrated near the center where the bulk of the synthesis of unstable nuclei takes place. The relative importance of the various PP reactions, and hence of the associated neutrino fluxes, depends on the rates of the nuclear reactions involved, which, in turn, are a function of density, temperature, and chemical composition. Since the internal structure of a model of the Sun depends on the adopted and somewhat uncertain input physics - e.g., the nuclear cross sections, the equation of state, the opacity, and the chemical composition of the gas from which the Sun formed - the detection of neutrinos from the Sun is fundamental not only to experimentally verify the nuclear origin of the solar luminosity, but also to confirm the overall reliability of the modeling of the internal structure of the Sun and the adopted input physics.

It is therefore understandable that the quest for the solar neutrinos started early, more than 40 years ago, with the Davis experiment (1967-1985) (Bahcall et al, 1985; Cleveland et al, 1998). This experiment, based on the interaction between an electron neutrino and ^{37}Cl , has a threshold energy of roughly 0.8 MeV and hence could essentially only detect the ^8B neutrinos, which constitute a minor fraction of the neutrino flux from the Sun. The Davis experiment provided two basic results, one very encouraging and another very stimulating. First, it detected solar neutrinos, demonstrating beyond any doubt that proton captures are occurring in the interior of the Sun. Second, the detected neutrino flux was roughly one third of the predicted value. Such a result stimulated much further work and a large number of papers on this puzzle were written over the decades. The discrepancy was considered by many physicists as a strong indication that the basic modeling of the Sun was wrong, however, it must be recalled that it was confined to a very minor branch of the PP chain. The discrepancy became more serious with the advent of the GALLEX experiment (Hampel et al, 1998) - a collaboration among France, Germany, Italy, Israel, Poland, and USA, led by MPIK Heidelberg, 1991-1997 - and the SAGE experiment (Abdurashitov et al, 1999) - a Russian-American collaboration, 1990-2000. These modern sophisticated experiments were designed to detect the bulk of the neutrinos produced in the Sun, i.e., the low energy neutrinos produced by the p+p reaction. They confirmed both the detection of a neutrino signature from the Sun and the existence of a discrepancy between theoretical and observed fluxes. This result plunged the basics of solar modeling into a crisis because these experiments were sensible to the total number of electron neutrinos emitted by the Sun. This number is theoretically robust, depending only on the basic assumption that the solar luminosity comes from the conversion of protons into α particles, and not on the details of the modeling of the internal structure of the Sun or of the cross sections of the nuclear reactions involved. If the solar luminosity is powered by the conversion of protons into α particles, the total number of electron neutrinos emitted per second by the Sun must be 2.38×10^{39} (L_\odot in MeV/s) / 25 (energy provided per α nucleus in

⁵ The term *metallicity* indicates the abundance of metals in a star, where metals corresponds to all elements heavier than He. The metallicity of the Sun is $\simeq 0.014$ by mass fraction, where abundances are normalised to a total of 1, which means that 1.4% of the solar matter is composed of elements heavier than He. The most abundant of these is oxygen, followed by carbon.

MeV) $\times 2$ (number of ν_e produced per α nucleus) [$\nu_e \text{ s}^{-1}$], which corresponds, at a distance of one astronomical unit, to a flux of $6.78 \times 10^{10} \nu_e \text{ s}^{-1}$. Instead, the neutrino flux detected by GALLEX and SAGE was only half of this prediction.

The solution to this puzzling discrepancy arrived when it was shown that neutrinos oscillate among three different species: ν_e , ν_μ and ν_τ . None of the Davis, GALLEX, or SAGE experimental set-ups could detect the ν_μ and ν_τ neutrinos so that all these experiments simply missed the fraction of neutrinos that reach the Earth as ν_μ and ν_τ . The Sudbury Solar Neutrino Observatory (SNO) experiment (a Canadian, USA, and UK collaboration that started in 1999, McDonald et al, 2002) was designed to detect all three neutrino flavors. In 2001 this experiment finally showed that there is agreement between the observed and predicted neutrino fluxes and hence demonstrated that our modeling of the interior of the Sun is basically correct. In 2008, the Borexino instrument finally also opened up the sub-MeV range for solar neutrinos and detected ^7Be neutrinos (BOREXINO Collaboration et al, 2008). For comprehensive reviews on the solar neutrino problem and current status, see Bahcall and Peña-Garay (2004); Bahcall (2005); Oberauer (2010).

3.3 Evolution to and through the First Giant Branch

In Subsection 3.3.1 we discuss the main evolutionary properties of stars once they leave the long lasting phase of central H burning described above, commonly referred to as the Main Sequence, and enter the phase known as the First, or Red, Giant Branch (RGB). At the end of central H burning a star is composed of a H-exhausted core made primarily of He and a H-rich envelope. Hydrogen burning shifts from the center to the base of the H-rich mantle while the envelope expands causing the surface of the star to reach radii 10-1000 times the solar radius and to cool down to a few thousand K. This expansion triggers the formation of large scale convective motions extending from the surface down to deep regions in the star where partial H burning occurred during the Main Sequence. Some products of this H burning are thus brought to the surface in a process known as the 1st dredge-up. In this phase the He core grows in mass because the H-burning shell continuously converts H-rich matter into He-rich matter and deposits the ashes onto the He core. The temporal evolution of the He core depends on its initial size, i.e., the size it had just after the central H exhaustion, which is in turn mostly determined by the initial stellar mass. If the mass of the He core is less than $\simeq 0.35M_\odot$, which occurs for initial stellar masses less than $\sim 2M_\odot$, an *electron degenerate core* forms where matter reaches such extraordinarily high density, up to $\simeq 10^6 \text{ g/cm}^3$, that the dominant contribution to its pressure arises from the Pauli exclusion principle, which prevents the electrons from occupying identical quantum states. This leads to an increase of the lifetime of this phase up to about 100 Myr, and forces the subsequent He ignition to occur quite far from the center. If the He core is instead more massive than $0.35 M_\odot$, the electrons remain far from the degeneracy regime.

In Subsection 3.3.2 we discuss the conditions under which ${}^7\text{Li}$, the stable daughter of radioactive ${}^7\text{Be}$, may be produced, preserved, and brought to the stellar surface. This nucleus is typically destroyed in the PP chain (Table 3.1), because its destruction rate is efficient at temperatures lower than its production rate. A way to produce ${}^7\text{Li}$ was proposed in 1971 by Cameron and Fowler (1971): if freshly synthesized ${}^7\text{Li}$ is quickly brought to very low temperatures by mixing, then it can be preserved. If H burning occurs in a convective environment it is in principle possible to find a high Li abundance on the surface of a star, as observed in some stars belonging to the First Giant Branch. However, these observations are in fact difficult to explain because H burning occurs in a formally stable region well below the base of their convective envelopes. Additional mechanisms of mixing must be invoked to bring ${}^7\text{Li}$ -rich material into the convective envelope.

3.3.1 The First Giant Branch

During the Main Sequence phase of stellar evolution described in the previous section conversion of H into He via H burning in the centre of the star leads to a progressive increase of the mean molecular weight combined with a decrease of the amount of available fuel. The net result is a slight increase of the luminosity (because L scales with the fourth power of the molecular weight, equation 3.10 in Subsection 3.2.1), and a mild expansion of the surface of the star because of the formation of a molecular weight gradient (Stancliffe et al, 2009). Once H is exhausted in the central region of the star, the H-exhausted core, or He core, begins to contract on a gravitational timescale while the region of active nuclear burning smoothly shifts above the He core, where H is still abundant. Further evolution of the He core depends on its mass, which, in turn, depends on the initial total mass of the star. If the He-core is more massive than a threshold value of $\sim 0.35 M_{\odot}$, which happens for an initial total mass of $\sim 2 M_{\odot}$, its contraction induces strong heating of the He core itself, which quickly reaches a temperature of ~ 100 MK at which fusion reaction of α particles (He burning) is activated. If, instead, the core is less massive than $0.35 M_{\odot}$ the high densities reached render the electron gas degenerate, hence supporting the structure against gravity without the need for additional contraction.

This difference has a large impact on further evolution of the star because, in the latter case, the He core tends towards an almost isothermal configuration due to the large mean free path of degenerate electrons relative to that of photons. If the structure was isolated, as in the case of white dwarves, it would progressively cool down losing its stored energy through the surface. Instead, in the case discussed here, the degenerate structure heats up because it is surrounded by the H-burning shell, which continuously deposits freshly synthesized He onto the He core. The rate at which the maximum temperature increases with time in the degenerate He core is controlled by the growth rate of the He-core mass, which obviously coincides with the rate at which the H-burning shell converts H into He. Strong neutrino production (Itoh et al, 1989) in the center of the electron degenerate core, due to the interaction

of photons with the plasma and/or to the scattering of photons on electrons, carries away energy from the core pushing the location of the maximum temperature outward in mass. The off-center location of the maximum temperature is the result of the balance between energy loss due to the neutrino emission, which scales directly with the density and pushes the maximum temperature outward, and the energy gain due to the compressional heating, which scales inversely with the density and pushes the temperature maximum back towards the center. The key stellar parameters that control the location of the maximum temperature are the CNO abundance and the initial mass of the star. The higher the CNO abundance, the faster the conversion of protons into α particles in the H-burning shell, the stronger the heating of the degenerate He core, and the closer the maximum temperature is to the center. The higher the initial mass of the star, the lower is the degree of electron degeneracy and the density in the He core, and hence the efficiency of neutrino production.

While the H-burning shell influences the evolution of the He core, the growth of the He core influences the evolution of the H-burning shell as well. In fact, the progressive heating of the core raises the temperature at the surface of the core, where H burning occurs. This results in a continuous positive feedback: the H burning shell deposits He onto the He core, which therefore heats up. Such a heating leads to an increase of the temperature and density in the H-burning shell, accelerating the H burning rate and increasing the conversion rate of H into He, and therefore the heating of the He core. As a consequence, the progressive increase of the H burning rate determined by the growth of the He core mass forces the H rich mantle of the star to expand and to cool. The cooling of the stellar envelope triggers a large increase of the opacity because atoms become partially ionised. The temperature gradient steepens, favoring the growth of convective instabilities that very quickly extend over a major part of the H-rich mantle from the surface down to near the outer border of the H-burning shell. A consequence of the growth of these convective motions within most of the H rich mantle is a large increase of the surface luminosity caused by the continuous increase of the H burning rate coupled to the fact that the convective envelope does not absorb or release energy but just transports it outward.

Since convective motions play a fundamental role in the physical and chemical evolution of any star, we briefly sketch the basic physical reason that leads to the growth of these large scale motions. The equilibrium condition provided by counterbalancing pressure gradients and gravity in stars does not necessarily imply stationary matter: a bubble of stellar matter may be considered stable against motion if a restoring force pushes it back towards its rest position when, for any reason, it is slightly displaced from its equilibrium location. Such a restoring force is simply given by Archimede's force, i.e., it depends on the density contrast between that of the environment and that of the bubble. If the density of an element of matter displaced towards a lower/higher density region turns out to be even lower/higher than that of its new surroundings, the element will continue to *raise/sink* and move away from its rest position, otherwise it will move back towards its equilibrium location.

Changes in the physical structure of the bubble during its motion play an important role in determining its density and thus its behavior. Mechanical equilibrium with the environment is certainly well verified so that it can be safely assumed that

the internal pressure within the bubble instantaneously readjusts to that of the environment. More difficult is to determine the amount of heat that the bubble can exchange with the environment while moving. In the simplest case in which the bubble does not exchange any heat with the surroundings until it has covered a certain distance (adiabatic approximation), and assuming that the region is chemically homogeneous, the critical condition for the onset of large scale motions of the matter is that the temperature gradient of the environment must exceed the adiabatic gradient (Schwarzschild criterion). While the radiative temperature gradient remains less than the adiabatic temperature gradient, an element of matter will remain more/less dense than its surroundings if displaced towards less/more dense regions (within stars these displacements are typically connected to movements outward/inward in mass), and hence it will experience a restoring force that will keep it anchored to its rest location. On the contrary, when the radiative temperature gradient exceeds the adiabatic temperature gradient stochastic motion of the matter is not hampered by a restoring force, but it is amplified leading to the growth of large scale motions. Hence, convective regions are associated with steep temperature gradients, which typically occur either close to regions where energy production is strongly concentrated, or in regions where the mean free path of the photons, which scales with the inverse of the opacity, becomes so small that radiation energy transport becomes inefficient.

The determination of the temperature gradient in convective regions is quite complex. Here it suffices to say that while in the interior of a star the temperature gradient in a convective region remains very close to the adiabatic gradient, in a convective envelope the temperature gradient becomes much steeper (intermediate between the radiative and adiabatic case) because the low density in the outer envelope makes energy transport by convective eddies inefficient, so that both photons and eddies contribute to the outwards transport of thermal energy.

Since convective eddies have a very large mean free path with respect to that of photons, convection is a very efficient energy transport mechanism. In the specific case of the extended convective motions that form above the H-burning shell in Red Giant stars, energy transport is so efficient that virtually all the energy produced by the burning shell is transmitted to the surface without essentially any absorption by the convective layers. It follows that a star in the H-burning shell evolutionary phase is forced to increase in size to be able to get rid of the extra energy influx, while the drop of the surface temperature is limited by the presence of a maximum temperature gradient: the adiabatic temperature gradient, which cannot be overcome by much in the largest fraction of the envelope mass.

The mere existence of stars in the RGB phase constitutes evidence of a) the presence of an active H-burning shell, demonstrated by the breaking of the mass-luminosity relation $L \propto M^3$ that holds during the Main Sequence phase, b) the presence of a maximum temperature gradient, demonstrated by the only minor change of the surface temperature along the RGB, c) the continuous increase of the energy production by the H-shell burning, demonstrated by the continuous increase of the surface luminosity, and d) the presence of an electron degenerate core (for stars with initial mass less than $\simeq 2 M_{\odot}$), demonstrated by the existence of a relatively long

lasting, $\sim 10^8$ yr, and thus observable RGB phase, which would be prevented if the He core was gravitationally contracting.

Soon after the formation of the H-burning shell, the large scale motions that grow in the H-rich envelope and rapidly extend from the surface down to just above the top of the H-burning shell, bring to the stellar surface matter partially processed by proton-capture reactions during the Main Sequence phase. This mixing, referred to as the 1st dredge-up, modifies the stellar surface composition. The amplitude of these modifications depends on the initial stellar mass and metallicity, the general rule being that the amplitude of the changes of the surface composition scales with the initial stellar mass, directly up to $3 M_{\odot}$ and then inversely for higher masses, and inversely with the metallicity. Figure 3.2 shows the abundance profiles of several nuclear species as a function of the mass location for a solar-like stellar model evolved to the RGB, just before the convective envelope deeply penetrates into the star. The solid vertical line shows the maximum inward penetration of the convective envelope. Since the convective motions reach layers in which the local chemical composition has previously been modified by nuclear burning, also the surface chemical composition is modified by the mixing induced by these large scale motions. In particular the surface He abundance is slightly increased by 5%, ^3He increases by one order of magnitude, ^7Li is destroyed, the $^{12}\text{C}/^{13}\text{C}$ ratio drops from the solar value of 89 to roughly 30, the $^{14}\text{N}/^{15}\text{N}$ ratio increases from the terrestrial value of 272 to $\simeq 500$, while the oxygen isotopic ratios and those of heavier nuclei remain at their solar values. In stars more massive than the Sun the oxygen isotopic ratios are also modified with $^{16}\text{O}/^{17}\text{O}$ decreasing by up to one order of magnitude, from solar $\simeq 2700$ to ~ 250 and $^{18}\text{O}/^{16}\text{O}$ increasing mildly up to $\simeq 700$ from the solar value of 500. A detailed quantitative determination of these changes depends on the specific stellar model considered.

The evolution of the star after the 1st dredge-up is characterized by the H-burning shell progressively converting H from the convective envelope into He, which is deposited onto the inert He core. The continuous mass transfer from the envelope to the core progressively reduces the mass of the envelope while its chemical composition does not change any more because the temperature within the convective envelope is too low to activate nuclear reactions.

The evolution along the RGB ends when the maximum temperature in the core is high enough, $\simeq 100$ MK, to activate the burning of He via 3α reactions, during which three α particles join into a ^{12}C nucleus. If the pressure is dominated by degenerate electrons the energy released by these reactions cannot be immediately balanced by an expansion of the core. Hence, He ignition occurs through a series of *flashes*, which progressively remove the degeneracy, shifting the burning towards the center. Once the electron degeneracy is fully removed, a quiescent central He-burning phase settles in.

All along the complex, and partly still mysterious, RGB evolutionary phase that links central H to central He burning, radioactive nuclei are produced by H-shell burning mainly via the CNO cycle. Most of them, however, have negligible lifetimes, so they could only be detected through the neutrinos they emit. Unfortunately,

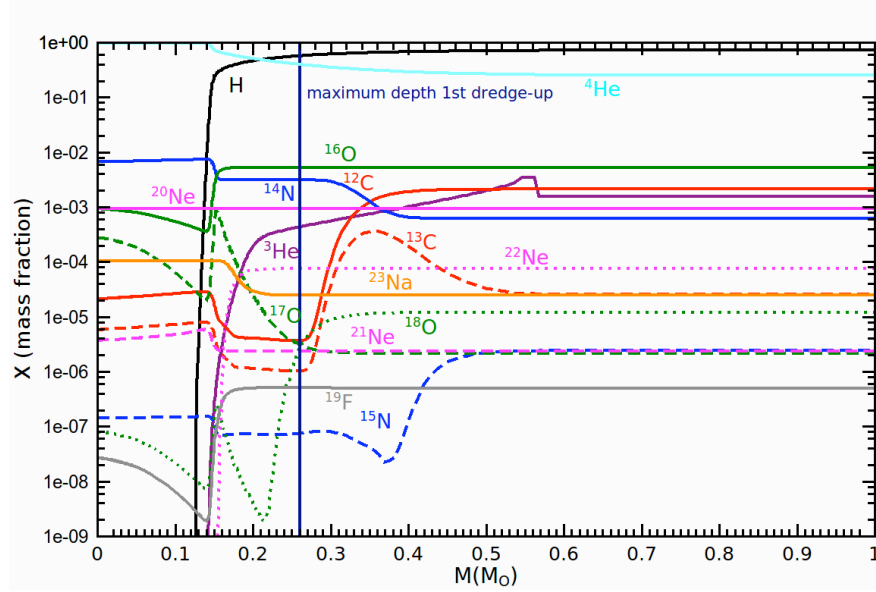


Fig. 3.2 Snapshot of the abundances of several nuclear species in a solar-like stellar model just before the onset of the 1st dredge-up. The maximum inward penetration of the convective envelope during the 1st dredge-up is marked by the vertical solid blue line.

no Red Giant star is close enough to the Earth to allow the detection of neutrinos of nuclear origin produced in its interior. However, there are two unstable nuclei, ^7Be and ^{13}N , whose half life may be comparable or even larger than some stellar timescales: for ^7Be the half life is comparable to the envelope mixing turnover time, for ^{13}N the half life is comparable to proton-capture timescale in extremely metal-poor stars, because stars of lower metallicity are more compact and hotter, due to their lower opacity.

In the next section we discuss specifically the abundance of ^7Li , the stable daughter of ^7Be , in giant stars, which could provide important clues about the presence of additional motions extending below the base of the convective envelope. This is important because, as we described above, the modeling of large scale motions within stars is still crude and their growth, timescale, and efficiency not yet well understood.

3.3.2 The Production of Li

Lithium (Li) isotopes⁶ in stars are fragile as they are easily destroyed by proton-capture reactions once the temperature exceeds 3 MK. The destruction timescale drops from 100 Myr at 3 MK to only 0.3 Myr at 5 MK while their production through fusion reactions only occurs at much higher temperatures, between 10 MK and 25 MK. The lower limit is due to the fact that the synthesis of ${}^7\text{Li}$ is initiated by the ${}^3\text{He}(\alpha, \gamma){}^7\text{Be}$ reaction, which becomes efficient only at temperature of the order of 10 MK, while the upper value is due to activation of the ${}^7\text{Be}(p, \gamma){}^8\text{B}$ reaction, which overcomes the electron-capture reaction ${}^7\text{Be}(e^-, \nu){}^7\text{Li}$ above a temperature of the order of 25 MK. Hence, Li is efficiently produced in a temperature range where it is also efficiently destroyed and therefore there seems to be no room for Li production in a star. However, there are a number of Red Giant stars observed to be Li rich (Castilho et al, 2000; Balachandran, 2005; Uttenthaler et al, 2007).

A possible way out of such a puzzling situation was recognized by Cameron and Fowler (1971) and is based on the idea that instabilities, such as convection, rotation-induced instabilities, thermohaline mixing, etc., may bring freshly made ${}^7\text{Be}$ from its production site to more external regions, where the temperature is low enough to inhibit proton captures on ${}^7\text{Li}$, on a timescale shorter than that of electron capture of ${}^7\text{Be}$. Note that the electron-capture rate of ${}^7\text{Be}$ shows a mild increase as the temperature decreases.

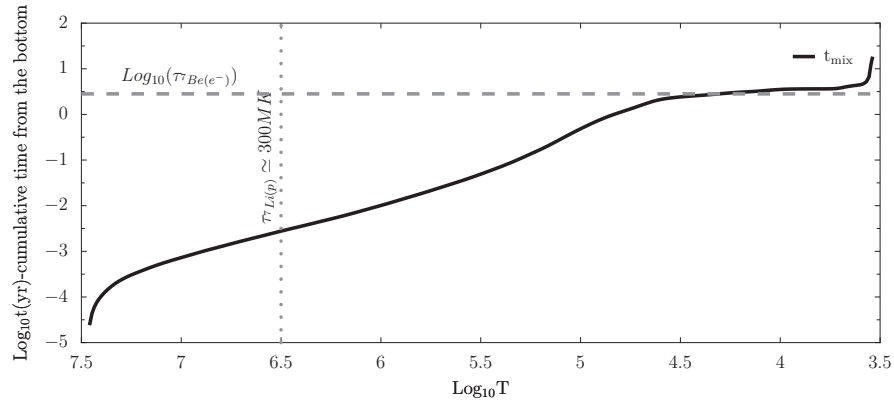


Fig. 3.3 The cumulative turnover time of the convective eddies computed from the base of the convective envelope up to the surface as a function of temperature, T . The star is a $6M_{\odot}$ star of solar metallicity some time after the beginning of the AGB phase. The horizontal dashed grey line marks the typical timescale of the ${}^7\text{Be}(e^-, \nu){}^7\text{Li}$ reaction while the vertical dotted grey line shows the threshold temperature below which the timescale of the proton capture on ${}^7\text{Li}$ becomes larger than 300 Myr.

⁶ Lithium has two stable isotopes ${}^6\text{Li}$ and ${}^7\text{Li}$, of which ${}^7\text{Li}$ is the more abundant representing 92% of solar Li.

A typical environment in which the Cameron-Fowler mechanism operates is during the Asymptotic Giant Phase (AGB) phase (Section 3.4.1), if the star is more massive than $4.5 M_{\odot}$. These stars develop large scale motions in the H-rich mantle that extend from the surface down to regions where the temperature is high enough (> 40 MK) for some nuclear burning to occur (Hot Bottom Burning), in particular via the ${}^3\text{He}(\alpha, \gamma){}^7\text{Be}$ reaction. Fig. 3.3 shows the cumulative turnover time from the base of the convective envelope to the region of temperature T given in the abscissa for a $6 M_{\odot}$ star of solar metallicity sometimes after the beginning of the AGB phase. The horizontal dashed grey line marks the typical timescale of the ${}^7\text{Be}(e^-, \nu){}^7\text{Li}$ reaction while the vertical dotted grey line shows the threshold temperature below which the timescale of the proton capture on ${}^7\text{Li}$ becomes larger than 300 Myr. In this environment ${}^7\text{Be}$ produced above 10 MK is successfully transferred before decaying to a region where its daughter ${}^7\text{Li}$ can survive.

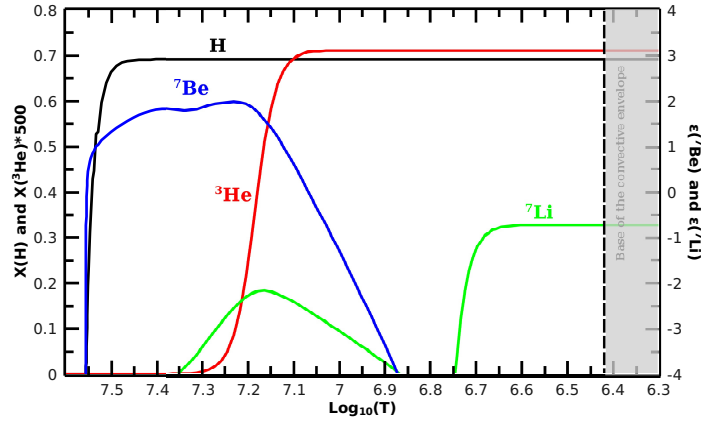


Fig. 3.4 Abundance profiles for H, ${}^3\text{He}$, ${}^7\text{Be}$, and ${}^7\text{Li}$ as function of the internal temperature in the region between the H-burning shell and the base of the convective envelope (grey area) for a solar-like stellar model on the RGB. The abundances of both ${}^7\text{Be}$ and ${}^7\text{Li}$ are given in the widely adopted logarithmic scale in which $\epsilon(X) = \text{Log}_{10}(N_X/N_H) + 12$, where N_X and N_H represent the abundances of element X and of hydrogen by number. In this scale the hydrogen abundance is equal to 12. $X(\text{H})$ and $X({}^3\text{He})$ represent the mass fraction of H and ${}^3\text{He}$.

An increase of the Li abundance at the surface of RGB stars is more difficult to achieve. Though the turnover time scale within the convective envelope is also in this case rather short ($\simeq 1$ yr at $\text{Log}_{10}(L/L_{\odot}) \simeq 2$), the temperature at the base of the convective envelope always remains well below 5 MK, too low to lead to an appreciable production of ${}^7\text{Be}$. Nonetheless, as mentioned above, observations show the existence of a small number of Li-rich RGB stars. Fig. 3.4 shows the internal structure of the region around the H-burning shell from a solar-like stellar model on the RGB. Here, ${}^7\text{Be}$ is synthesized well below the region where large scale motions

of the matter and hence mixing of the chemical composition occur. In this environment the Cameron-Fowler mechanism could operate only by assuming the presence of presently unidentified instabilities able to drive some mixing between the region rich in ${}^7\text{Be}$ and the base of the convective envelope. The main constraint on this *extra* mixing is that it must get close enough to the active H-burning shell to reach the layers where the ${}^7\text{Be}$ production occur, but it must not enter the region of the main nuclear burning. The reason is that the speed at which a star climbs along the RGB is regulated by the speed at which H is converted into He (see above) which, in turn, also depends on the amount of fuel that continuously enters the burning region. If this extra mixing reached the active burning region, it would inevitably bring fresh H into the burning region, therefore altering the rate at which H is consumed by the H-burning shell and hence the timescale of evolution along the RGB. This evolutionary timescale is observationally well established from counting the number of stars on the RGB in many Galactic globular clusters, and already very well reproduced by current models of these stars without extra mixing.

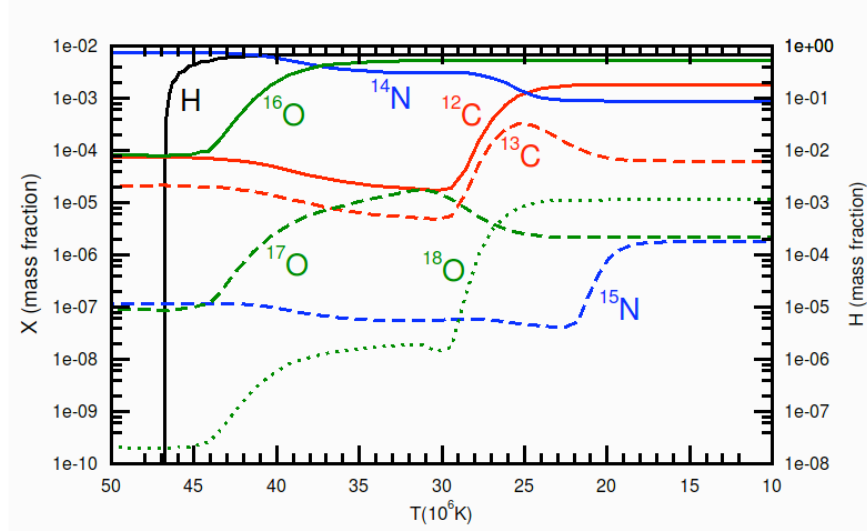


Fig. 3.5 Abundance profiles of the CNO isotopes as function of the temperature on the RGB in a solar-like stellar model.

There are other hints that point towards the presence of extra-mixing phenomena in RGB stars (and perhaps in AGB stars too, as discussed in Sections 3.6.1 and 3.6.2). The observed surface ${}^{12}\text{C}/{}^{13}\text{C}$ ratio and N abundance are, respectively, too low and too high with respect to the values predicted by the 1st dredge-up. Extra mixing would naturally lower the first ratio and raise the N abundance, this being the signature of H burning (see Table 3.3). A deeper mixing than predicted by current

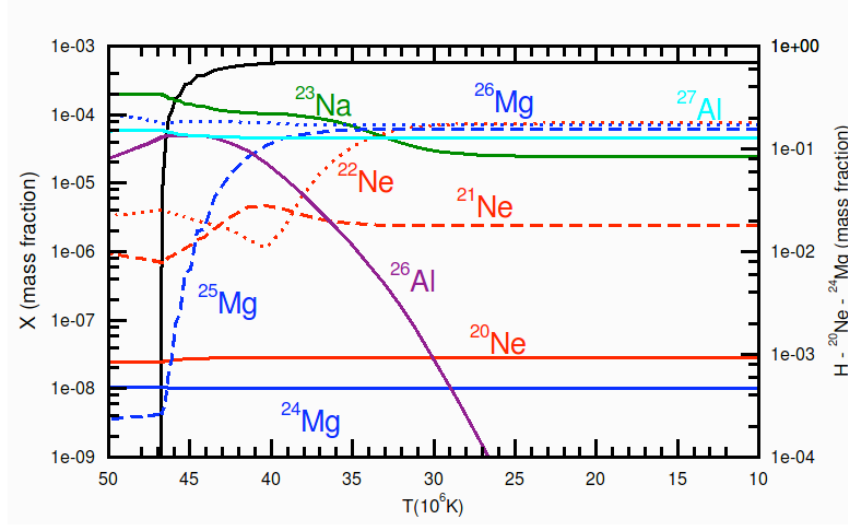


Fig. 3.6 Abundance profiles of the Ne, Na, Mg and Al isotopes as function of the temperature on the RGB in a solar-like stellar model.

models would also reduce the abundance of ^3He in the stellar envelope, which is increased by the 1st dredge-up, by bringing this nucleus down to regions where it is destroyed. This reduction is needed to avoid an increase of the ^3He abundance in the interstellar medium, which is not observed, due to the material expelled by low-mass stars over the lifetime of the Galaxy.

Figs 3.5 and 3.6 show the isotopic abundances of several nuclei up to Al within a solar-like star while climbing the RGB (at $\text{Log}(L/L_\odot) \simeq 3$). Note that we chose to use the temperature as the abscissa instead of mass to better clarify the temperature at which each nuclear species varies. The figures clearly shows that, for each given depth reached by an extra mixing process, a few nuclei are expected to be modified. For example, a drop of the oxygen abundance at the surface of an RGB star due to an extra mixing process (the depth reached by the extra mixing should extend down to at least 40 MK in this case), would also imply an increase of the surface abundances of both N and Na. Isotopes like ^{18}O and ^{22}Ne are expected to be fully destroyed, while the $^{12}\text{C}/^{13}\text{C}$ ratio should drop and the $^{14}\text{N}/^{15}\text{N}$ increase. Note that in any case it would be very difficult to obtain a surface change of the Ne and the Mg abundances because their most abundant isotopes, ^{20}Ne and ^{24}Mg , are not modified unless the mixing reaches down to the location of main H burning.

In summary, our modeling of mixing in stars is still oversimplified and unrealistic as it is based on a simple buoyancy model. Observational evidence of stellar abundances also involving radioactive nuclei and their daughters points out that mixing of matter outside the standard convective boundaries should occur in stars. These observations can be used to improve our description of mixing phenomena in stars.

3.4 Evolution in the Double Shell Burning Phase

We start Subsection 3.4.1 by describing the central He-burning phase and the direct scaling of the mass of the convective core resulting from He burning with the mass of the He core. The mass of the convective core determines the size of the initial He-exhausted core, an important parameter for subsequent evolutionary phases. As it happens previously when H burning shifts from the centre to a shell, also when He is exhausted in the core and He burning shifts from the centre to a shell, the envelope is forced to expand and convective motions extend from the external layers deeply inward into the star. In stars more massive than $4.5 M_{\odot}$ the convective envelope even penetrates within the He core reducing its mass size and carrying to the stellar surface material processed by nuclear reactions (2^{nd} dredge-up). If the He-exhausted core does not grow above $\sim 1.1 M_{\odot}$, an electron degenerate core forms again, this time made of C and O, on top of which are located two burning shells: the He-burning and the H-burning shells. This marks the beginning of the double burning shell phase: the Thermally Pulsing Asymptotic Giant Branch (TP-AGB) phase.

The two key features of this phase are that (1) the two burning shells can not be simultaneously active, but they alternate within a cycle in producing the required energy and (2) He ignition within each cycle occurs through a thermal runaway (or thermal pulse, TP) that ends when enough energy is injected in the He-burning zone to convert its temperature and density profiles into a configuration that allows stable burning. The frequency of these thermal instabilities scales directly with the He-core mass. Such an abrupt injection of a quite large amount of energy ($\sim 10^{48}$ erg) induces first the growth of a convective shell within the *intershell* zone, located between the two shells, and second, soon after this convective region is extinguished, the expansion of the base of the H-rich envelope, which forces the convective envelope to penetrate well within the intershell zone (3^{rd} dredge-up). The combination of these two successive convective episodes allows nuclei freshly synthesized by He burning to be carried up to the stellar surface. Moreover, the temperature at the base of the convective envelope scales directly with the He-core mass, and, in stars more massive than $4\text{--}5 M_{\odot}$, reaches high enough values that H burning activates (Hot Bottom Burning, HBB).

In Subsection 3.4.2 we discuss Super-AGB stars, i.e., stars with initial mass that locates them in the interval between stars that develop an electron degenerate core after He is exhausted in the center and enter the AGB regime, and more massive stars that do not develop an electron degenerate core. Super-AGB stars ignite carbon out of center in semidegenerate conditions and go through a central C-burning phase. However, the C-exhausted core is not massive enough to heat up to the Ne burning, so an electron degenerate ONeMg core forms. These stars then go through a thermally pulsing phase. The final fate of these stars depends on the capability of their ONeMg core to reach the critical mass of $\sim 1.35 M_{\odot}$ required to activate electron captures on ^{24}Mg and ^{20}Ne . Stars with a core that does not reach this critical mass lose all their H-rich envelope and end their life as ONeMg white dwarves, while stars with a core that reaches this critical mass explode as *electron-capture supernovae*.

We continue by briefly discussing mass loss during the AGB phase in Subsection 3.4.3. The strong increase in surface luminosity, coupled to luminosity variations and formation of dust grains in the atmospheres of AGB stars, strongly enhances the mass-loss rate in this phase with the consequence that all AGB stars lose their H-rich envelope, leaving behind the naked electron degenerate core as a cooling CO white dwarf. Finally, in Subsection 3.4.4, we discuss the different species of dust grains that form in the atmosphere of an AGB star. The key role here is played by the C/O number ratio in the atmosphere because the strong bond of the CO molecule results in trapping all of the atoms of the least abundant of the two elements. In an oxygen-rich gas ($O > C$) the species of dust are oxide grains, for example, Al_3O_2 (corundum) and many different types of silicates (SiO , SiO_2 , etc). In a carbon-rich gas ($C > O$), the species of dust are, for example, SiC (silicon carbide) and C itself (graphite). Some of this stellar AGB dust is now recovered from primitive meteorites, representing a real speck of an ancient AGB star that we can analyse in the laboratory.

3.4.1 Asymptotic Giant Branch (AGB) Stars

As anticipated at the end of Subsection 3.3.1, once the central temperature in a RGB star exceeds 100 MK, He in the core starts being converted into ^{12}C via 3α reactions, and subsequently into ^{16}O via $^{12}C(\alpha, \gamma)^{16}O$ reactions. The cross section of the 3α reaction has a tremendous dependence on the temperature: it scales roughly as T^{23} in the range 100-300 MK, so that the energy produced by these reactions is very strongly concentrated towards the centre of the star where the temperature is at its maximum. The very large photon flux that forms in these conditions triggers the formation of large scale motions of the matter, which mix the material in the central part of the star (the convective core) in order to efficiently carry the energy outward. The mass of the convective core depends on the luminosity produced by the 3α reactions. This luminosity scales with the mass of the He core because the larger its mass, the larger is the amount of energy required to maintain the hydrostatic equilibrium (see Section 3.2). Hence, the size of the convective core scales directly with the mass of the He core. The mass of the He core, in turn, scales directly with the initial mass of the star, thus, in conclusion, the mass of the convective core scales directly with the initial mass of the star. Analogously to the Main Sequence central H-burning phase, the energy production in the core is dictated by the mass of the star (see Section 3.2.1). However, the role played by the total stellar mass in central H burning in the central He-burning phase is replaced by the He-core mass because the density contrast between the He core and the H-rich mantle is so large that the core does not feel the presence of the H rich mantle and evolves as if it was a naked He core.

In the meantime, the temperature at the He/H interface is high enough that also an efficient H-burning shell is active leading to continuous deposition of fresh He onto the He core. Moreover, large convective motions develop (in most cases) in the outer

H-rich envelope. The actual extension and temporal variation of these convective regions depends on the initial mass and chemical composition of the star.

At variance with H burning, no radioactive nuclei are produced by the 3α and the $^{12}\text{C}(\alpha, \gamma) ^{16}\text{O}$ reactions because they convert matter along the valley of β stability. Radioactivity during He burning is produced instead via the sequence of reactions that convert ^{14}N into ^{22}Ne via a double α capture and the radioactive decay of ^{18}F : $^{14}\text{N}(\alpha, \gamma) ^{18}\text{F}(e^+ + \nu) ^{18}\text{O}(\alpha, \gamma) ^{22}\text{Ne}$. In H-exhausted regions, ^{14}N is by far the most abundant nuclear species after He because a main effect of the CNO cycle, which operated in the previous H-burning phase (see Section 3.2.1) is to convert most of the initial C and O, the two most abundant elements beyond H and He, into N. Hence, during He burning ^{22}Ne becomes the most abundant isotope, after C and O, once ^{14}N is fully consumed by α captures.

When He is exhausted in the centre, He burning moves smoothly outward in mass leaving behind a CO core that begins to contract on a Kelvin-Helmholtz timescale. Similar to the H-burning shell, also the He-burning shell produces more energy than required to balance gravity because energy production is controlled by the size of the underlying core, and not by the mass of the star. The CO core increases progressively in mass because of the continuous deposition of CO-rich material made in the He-burning shell and the He-burning shell increases its energy production accordingly. As a consequence, the overlying He+H-rich mantle is forced to expand substantially and to cool down so much that the H-burning shell switches off. As during the RGB phase, this expansion progressively inhibits energy transport by radiation and large scale motions of the matter progressively extend inward from the outer envelope. In stars initially more massive than $4\text{--}5 M_{\odot}$ the convective envelope penetrates even inside the He core (2^{nd} dredge-up). The main consequences of this are a change of the surface abundances and a reduction of the He-core mass. Similar to what happens during the RGB, the formation of an extended convective envelope forces the star to expand at roughly constant surface temperature (because the onset of convective motions fixes a maximum value for the temperature gradient, see Section 3.2.1) and increasing luminosity. This phase is called Asymptotic Giant Branch (AGB). The specific phase when the He-burning shell advances in mass eroding the border of the He core from within is called Early Asymptotic Giant Branch (E-AGB).

The competition between the advancing He-burning shell and the sinking of the convective envelope during the 2^{nd} dredge-up fixes the maximum mass that the CO core (M_{CO}) reaches in this phase. If M_{CO} is larger than roughly $1.1 M_{\odot}$, the core heats up to the C ignition temperature ($\sim 8 \times 10^8$ K), otherwise it turns into an electron degenerate CO core able to self-sustain against gravity without the need of additional contraction. The maximum initial stellar mass for which an electron degenerate CO core forms is of the order of $7\text{--}8 M_{\odot}$, for solar metallicity stars. While the evolution of stars without an electron degenerate core is dictated by the self gravity of the core, the evolution of stars with an electron degenerate core is controlled by the burning shells. In the following we concentrate on the further evolution of the latter case, i.e., the AGB, while Chapter 4 describes the further evolution of the first case.

On the AGB three main regions may be identified: the electron degenerate CO core, a He-rich layer (also referred to as *intershell* since it is located between the He- and the H-burning shells), and a H-rich mantle, most of which forms an extended convective envelope. As the He-burning shell approaches the border of the He core, it quenches because of the steep temperature drop associated with the drastic reduction of the mean molecular weight caused by the change from a He-dominated to a H-dominated chemical composition. Being less and less supported by the extinguishing He burning shell, the mantle is forced to shrink, heat up, and progressively re-activate the H-burning shell at its base. The H-burning shell starts to deposit fresh He onto the He shell forcing the intershell to heat up again. At this point a fascinating evolutionary phase begins in which nuclear burning and instabilities coexist, realizing a unique *habitat* in which a large number of nuclear species may be synthesized: the Thermally Pulsing AGB (TP-AGB) phase.

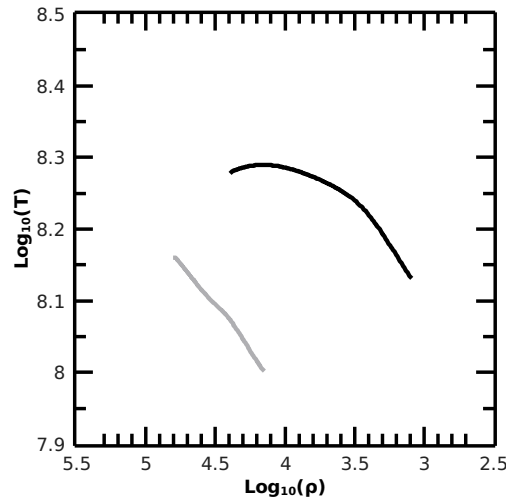


Fig. 3.7 The gray thick solid line shows the typical $\text{Log}(T)$ - $\text{Log}(\rho)$ profile in the intershell (in the range $10^{-3} < X_{\text{He}} < 0.9$) just prior the onset of a thermal pulse in a $3 M_{\odot}$ of solar metallicity while the black thick solid line shows the typical profile in the same region at the end of the thermal runaway when the steady He burning occurs.

Quite schematically, the TP-AGB phase consists of a sequence of cycles each of which may be divided in two main phases: a quiescent H-burning phase during which the He-burning shell is inactive, and a He-burning phase during which the H-burning shell is inactive. Though the two shells do not operate simultaneously, they process roughly the same amount of mass per cycle so that the intershell mass changes (shrinks) slowly in time. The transition from the active He-burning phase to the active H-burning phase occurs quiescently in the sense that the energy provided

by the H-burning shell progressively replaces that provided by the dimming He-burning shell. Instead, the transition from the active H-burning phase to the active He-burning phase occurs in a traumatic way, which is responsible for the peculiar sequence of events that characterizes the TP-AGB phase.

The reason for such a traumatic He ignition is that the pileup of fresh He on top of an inert intershell leads to a T, ρ profile in the intershell that is controlled by the compressional heating caused by the accretion of fresh He. This T, ρ profile is quite different from the typical one determined by the presence of an active burning shell. The large amount of energy required to turn the T, ρ profile from that determined by the accretion and that required by the steady He burning, coupled to the very steep dependence of the cross section of the 3α nuclear reaction on the temperature, determines the growth of a thermal runaway (or *thermal pulse*, TP) in which a huge amount of energy is released over a very short timescale. This runaway comes to an end when enough energy has been deposited in the intershell to turn the T, ρ profile into a profile suited for quiescent He burning. As an example, Figure 3.7 shows as a gray line the typical $\text{Log}(T), \text{Log}(\rho)$ profile produced by the advancing H-burning shell just prior to 3α ignition, while the black line shows the typical profile at the end of the thermal runaway during steady He burning. In this specific example roughly $\sim 10^{48}$ erg must be deposited in the intershell to perform the transition between the two configurations. This amount of energy is determined by the fact that the needed change of the T, ρ structure in the intershell requires a reduction of the binding energy of the intershell.

The main effect of the rapid injection of energy into the intershell during the TP is the production of a very strong energy flux, which forces the growth of convective instabilities to efficiently carry the energy outward. This convective shell extends over most of the intershell region and plays a fundamental role in reshuffling the chemical composition within this region and hence influencing the detailed nucleosynthesis that occurs at this stage (see next Sections). Once the TP comes to an end, the convective shell disappears and the quiescent He-burning shell phase begins. Another important side effect of the rapid energy injection caused by the TP is the expansion of the region above the He-burning shell, which forces a cooling of this region. The consequence is that the H-burning shell switches off, and the temperature gradient steepens. This favors the penetration of the convective envelope down into the intershell so that nuclei freshly synthesized in the deep interior of the star are efficiently brought up to the stellar surface (3^{rd} dredge-up). Similar to what happens towards the end of the E-AGB phase, the He-burning shell progressively runs out of power as it approaches the border of the He-rich layer, where the temperature drops below the value necessary for the He burning. The overlying layers are forced to contract and heat so that a H-burning shell activates again and a new cycle starts.

To visually illustrate the sequence of events making up a full TP cycle and to make clear the peculiarity of the TP-AGB phase, Fig. 3.8 shows the temporal evolution of the internal structure of a typical AGB star through three consecutive TPs.

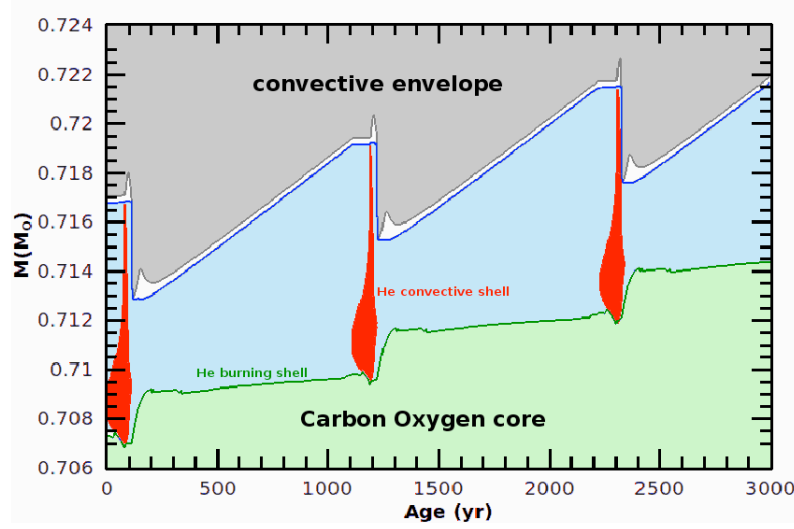


Fig. 3.8 Temporal evolution of the internal structure of a typical AGB star through three consecutive TPs. The He convective shell is shown in red while the convective envelope is grey. The H and He burning shells are shown in dark blue and dark green, respectively, while the intershell is light cyan. The timescale between the end of the He convective shell episode and the beginning of the successive one has been rescaled in order to improve readability. In particular it has been changed according to this formula: $t = t_{\text{end conv sh}} + (t - t_{\text{end conv sh}}) / (\Delta t_{\text{interpulse}} \times 10^3)$. In this way the interpulse phase is rescaled to last 10^3 yr.

The quantitative characteristics of the TPs depend on the core and envelope masses, the general rule being that larger CO core masses correspond to higher frequencies of thermal pulses, higher temperatures, and shorter lifetimes of the He convective shell. Typical TP frequencies (determined after the first 20 TPs or so) range between 2 and 3 TPs per 10^5 yr for a $3 M_{\odot}$ star having $M_{\text{CO}} \sim 0.7 M_{\odot}$ and more than 50 TPs per 10^5 yr for a $6 M_{\odot}$ star having $M_{\text{CO}} \sim 0.96 M_{\odot}$, while the peak luminosity ranges between 1 and $10^8 L_{\odot}$.

Since the two burning shells process about the same amount of matter per cycle, the average growth rate of the CO core per cycle roughly equates that of the He core. This, coupled to the fact that He burning produces (per unit mass) roughly 10% of the energy produced by H burning, and that the luminosity of these stars does not change appreciably between the two burning phases, allows us to estimate the relative burning lifetimes ($t_{\text{He}}/t_{\text{H}}$). The amount of energy produced by He burning per cycle must balance the surface losses, i.e., $\epsilon_{\text{He}} \times \Delta M_{\text{He}} = L_{\text{surface}} \times t_{\text{He}}$, where ϵ_{He} represents the amount of energy liberated by the He burning per unit mass, ΔM_{He} the amount of mass processed by the He burning, L_{surface} the luminosity of the star and t_{He} the lifetime of the He burning phase. Similar for the H burning one may write that $\epsilon_{\text{H}} \times \Delta M_{\text{H}} = L_{\text{surface}} \times t_{\text{H}}$. If the amount of mass processed is similar in the two cases (i.e., $\Delta M_{\text{He}} \simeq \Delta M_{\text{H}}$), the relative lifetimes scale roughly as the two nuclear burning rates, i.e., $t_{\text{He}}/t_{\text{H}} \sim 1/10$. The amount of He burnt during each He-

burning episode is only partial, corresponding to about 25%-30% of the He present in the intershell. Of this, roughly 25% burns during the TP and the remainder during the quiescent He burning phase. The final nucleosynthetic result is that carbon is produced via the 3α reaction, but it is only marginally converted into oxygen. The typical composition of the intershell after this partial He burning is represented by matter made by roughly 75% He and 23% ^{12}C , while the remaining few percent are made up of ^{22}Ne (from conversion of ^{14}N as detailed above) and of ^{16}O . The ^{22}Ne nuclei are of interest as they act as a neutron source in the TPs when the temperature reaches 300 MK. The lifetime of the He convective shell varies between 100 yr and 10 yr for the $3 M_{\odot}$ and $6 M_{\odot}$ stellar models, respectively. Typically, the He burning shell is located between 7×10^{-3} and $1.5 \times 10^{-2} R_{\odot}$ from the center of the star, while the H-burning shell is located between 1×10^{-2} and $2 \times 10^{-2} R_{\odot}$. The intershell mass ranges roughly between 10^{-3} and $10^{-2} M_{\odot}$. The surface radii of AGB stars vary between hundreds to thousands times the solar radius.

The final fate of AGB stars is to lose all their H-rich mantle before the electron degenerate core may grow to its most massive stable configuration (i.e., the Chandrasekhar mass). Such a destiny is due to the strong dependence of the mass-loss rate on the luminosity of the star and on its surface chemical composition (see Section 3.4.3). The maximum mass size reached by the CO core, which equates the mass of the newborn white dwarf, is determined by the competition between the speed at which the burning shells advance in mass and the efficiency of the mass loss that erodes the H-rich mantle from the surface.

The occurrence of the 3rd dredge-up significantly affects the evolutionary properties of an AGB star. First, it reduces the size of the He core anticipating the quenching of the quiescent He burning phase and hence its lifetime. Second, it slows down the overall growth rate of the CO core and the He-rich shell. Third, it carries to the stellar surface a fraction of the material freshly synthesized by partial He burning, i.e., C, ^{22}Ne , and *slow*-neutron capture (*s*-process) elements heavier than iron (see Section 3.5), drastically modifying the chemical composition of the star. In some cases, the star even changes from the usual oxygen-rich ($\text{O} > \text{C}$) composition to carbon-rich ($\text{C} > \text{O}$), with important consequences on the types of molecules and dust that can form and the ensuing mass loss (see Section 3.4.4). Unfortunately, the question of the maximum depth reached by the convective envelope during the 3rd dredge-up has always been highly debated and different results have been obtained over the years by different authors for AGB stars over the whole mass interval from $1.5 M_{\odot}$ up to the more massive thermally pulsing stars. The reason is that, once the convective envelope enters the He core, a discontinuity in the opacity (H is much more opaque than He) determines the formation of a positive difference between the effective and adiabatic temperature gradients just at the border of the convective envelope. This is an unstable situation because the possible mixing of matter located just below the base of the convective envelope with the H-rich convective mantle is an irreversible process in the sense that these *additional* mixed layers become intrinsically convective because of the drastic increase of the opacity due to the mixing. It is therefore clear that even small different numerical techniques adopted by different authors may lead to quite different results.

Furthermore, the occurrence of the 3rd dredge-up is important because it creates a sharp discontinuity between the convective envelope and the radiative intershell. Since a sharp discontinuity is not a realistic configuration in these conditions, the occurrence of the 3rd dredge-up allows the possibility that some kind of *diffusion* of protons occurs below the formal border of the convective envelope when it reaches its maximum inward extension at the end of the 3rd dredge-up smoothing out the discontinuity (though this is not obtained by applying the standard stability criteria for mixing). However, the shape, extent, and timescale over which the diffusion of protons in the He/C intershell may occur is unknown, its modeling is still artificial and not based on self-consistent computations.

This diffusion allows the formation of regions where a small amount of protons come in contact with matter that is predominantly composed of He and C, so that the ratio $Y(H)/Y(C) \ll 1$, but does not contain any ^{14}N , since this nucleus has been fully converted into ^{22}Ne in the previous TP. When these proton-enriched layers begin to contract and to heat because of the quenching of the He burning, the CN cycle activates, but it can not go beyond the synthesis of ^{13}C due to the low proton concentration. As the temperature increases to roughly 90 MK, the $^{13}\text{C}(\alpha, n)^{16}\text{O}$ reaction becomes efficient and a significant neutron flux is produced. Hence, this diffusion plays a pivotal role in the nucleosynthesis of species beyond the Fe peak via neutron captures. A detailed description of the properties of this neutron source and of its nucleosynthetic signature will be presented in Section 3.5.1. The lack of ^{14}N is crucial here, since this nucleus is a strong neutron poison and its presence would inhibit neutron captures by Fe and the elements heavier than Fe.

As already discussed in Section 3.3.2, typical temperatures at the base of the convective envelope do not exceed a few MK at most in the evolutionary phases prior to the AGB. Instead, another peculiarity of AGB stars is that during the H-burning phase the temperature at the base of the convective envelope may reach values in excess of several tens MK, and even exceed 100 MK, so that H-burning reactions activate within the convective envelope. The efficiency of this phenomenon, known as Hot Bottom Burning (HBB), scales directly with the temperature at the base of the envelope and hence with the CO-core mass, which in turn scales with the initial stellar mass. Hence, HBB is efficient in stars more massive than $4.5 M_{\odot}$, depending on the metallicity. As the energy produced in the convective envelope sums to that produced by the H-burning shell, the core mass - luminosity relation changes (even strongly) in the presence of HBB. From a nucleosynthetic point of view the occurrence of an active H burning in a convective environment implies a redistribution of the processed material over all the convective zone, so the surface abundances turn towards the relative abundances typical of the H burning at high temperature. For example, an increase of the surface abundances of nuclei like ^{14}N and ^{26}Al (discussed in detail in Section 3.6.1), a temporary increase of ^7Li , a reduction of ^{12}C and of the $^{12}\text{C}/^{13}\text{C}$ ratio and the signatures of the CNO, NeNa and the MgAl sequences.

We refer the reader to the review paper by Herwig (2005) and to the book chapter on the evolution of AGB stars by Lattanzio and Wood (2004) for a thorough presentation of the evolution of these cool giant stars.

3.4.2 Super-AGB Stars

In the previous section we identified stars that go through the double shell burning of the TP-AGB phase as those that develop an electron degenerate CO core where carbon burning fails to occur. There is, however, another class of stars that experience the double shell burning phase: those with initial total mass between the maximum mass that forms an electron degenerate CO core where C does not ignite (M_{up}) and the minimum mass that does not form an electron degenerate CO core (M_{mas}). Stars more massive than M_{mas} evolve up to the final core collapse as described in Chapter 4. Depending on the initial chemical composition and the adopted physics, M_{up} ranges between $6\text{--}8M_{\odot}$, and M_{mas} ranges between $9\text{--}12M_{\odot}$. It is important at this point to recall that these limiting masses are somewhat uncertain because they depend on the size of the convective core, the carbon to oxygen ratio left by the He burning, the efficiency of the 2^{nd} dredge-up and the cross section of the $^{12}\text{C}+^{12}\text{C}$ nuclear reaction. Unfortunately, all these quantities are still subject to severe uncertainties.

Stars falling between these two limits form a partially electron degenerate core, but are massive enough to ignite C in the core, lift the degeneracy, and go through the C burning in the core. They are not massive enough, however, to avoid the electron degeneracy of the ONeMg core left by C burning. The evolution of stars in this relatively small mass interval, called Super-AGB stars, has not been studied extensively up to now because of the difficulty in computing the C-burning phase due to the removal of the degeneracy that occurs through a series of successive flashes, and the lack of massive computer power, which is needed to study this complex situation. This situation is rapidly changing and progress is currently under way on the computational modeling of Super-AGB stars (Siess, 2006, 2007).

Since these stars form an electron degenerate core after core C burning, they also go through a double shell burning phase similar to the AGB phase experienced by their less massive counterparts. Because their degenerate cores are more massive, following the trend shown by AGB stars, the frequency of the thermal pulses is higher (up to 500 TPs per 10^5 yr), the He peak luminosity is lower than in the normal AGB stars (up to $\sim 4 \times 10^6 L_{\odot}$), while the base of the convective envelope may reach temperatures as high as 110 MK, hence, H burning occurs within the convective envelope (Hot Bottom Burning). Similar to what happens in the more massive AGB stars, but quantitatively more pronounced, the luminosity produced in the convective envelope adds to that produced by the radiative H burning significantly altering the core mass - luminosity relation and the surface composition is modified by the signature of H burning. The possible occurrence of the 3^{rd} dredge-up would also shuffle the surface chemical composition with the typical products of the partial He burning, i.e. C, and s-process elements. The efficiency of the 3^{rd} dredge-up is very uncertain also for these stars. In principle, one could expect a lower efficiency of the 3^{rd} dredge-up because the amount of energy released by a TP is lower and the overall temperature is much higher than in a standard AGB star, so that it could be more difficult to expand the base of the mantle and to steepen the temperature gradient up to a value that would allow the convective envelope to

penetrate the He core. Quantitative estimates of the yields of the nuclei specifically produced by the TP Super-AGB stars are in progress (Doherty and Lattanzio, 2006).

The final fate of a Super-AGB star depends on the competition between the advancing burning shells, which increase the size of the ONeMg core, and the mass loss, which limits its growth. Also an efficient 3rd dredge-up would contribute to limiting the growth of the core. Stars more massive than a critical value reach the threshold electron degenerate core mass for the onset of electron captures on ²⁴Mg and ²⁰Ne after a certain number of TPs and eventually explode as *electron-capture supernovae*. Stars less massive than the critical value, instead, end their life as ONeMg white dwarfs. An estimate of the electron degenerate core mass above which electron captures become efficient in an ONeMg environment can be determined by considering that the threshold energy for electron capture is 6 MeV for ²⁴Mg and 8 MeV for ²⁰Ne and that the mass of a fully electron degenerate core having a Fermi energy of the order of 6 MeV is $\simeq 1.35 M_{\odot}$. Thus, if the electron degenerate core grows to the threshold value of $\simeq 1.35 M_{\odot}$ or so, electron captures are activated on ²⁰Ne and ²⁴Mg.

This process removes electrons and hence pressure from the center of the star, starting a runaway process that leads to the core collapse and final explosion as electron-capture supernova. The explosion of these electron-capture supernovae is similar to that of core collapse supernovae (see Chapter 4), with a few distinct features. During the initial collapse of the degenerate core, electron captures increase significantly the degree of neutronization of the matter, i.e., raise the global neutron over proton ratio because of the capture of the electrons by the protons. The nuclear species produced by explosive burning depend significantly on the neutron over proton ratio so that the higher the degree of neutronization of the matter the higher the production of neutron-rich nuclei: in particular ⁵⁸Ni becomes favored with respect to ⁵⁶Ni. Since the luminosity peak of a supernova correlates with the amount of ⁵⁶Ni produced during the explosion, a natural feature of these electron-captures supernovae is a lower luminosity with respect to typical core collapse supernovae. Also, the final kinetic energy of the ejecta is expected to be of the order of 0.1×10^{51} erg, roughly one order of magnitude lower than in typical core collapse supernovae (see, e.g., Hoffman et al, 2008; Wanajo et al, 2009).

3.4.3 Winds from AGB Stars

An observed peculiarity of AGB stars is that they show strong stellar winds, which carry material away from the surface of the star into its surroundings. Nuclei newly synthesised during the AGB phase and carried to the stellar surface by the 3rd dredge-up are shed into the interstellar medium so that AGB stars contribute to the chemical make-up of their environments and of new generations of stars. The mass loss rate due to winds in AGB star increases as the star evolves along the AGB and can reach values as high as $10^{-4} M_{\odot}/\text{yr}$ (to be compared, for example, to the solar mass loss rate of $10^{-11} M_{\odot}/\text{yr}$) at the end of the AGB, which is known as the

superwind (Iben and Renzini, 1983). This is a strong and dense but slow wind, with material leaving the star at relatively low speeds of 5-30 km/s.

The winds are caused by two main factors. First, large quantity of dust form around AGB stars and radiation pressure acting on this dust contributes to driving the winds. The extended envelopes of red giant and AGB stars, where the temperature drops down to $\sim 1,000$ K, are an ideal location for the formation of a large variety of molecules like CO, TiO, VO, as well as ZrO, when the gas has been enriched in heavy elements such as Zr by the *s*-process and the 3rd dredge-up, and C₂, CN, and CH, when the gas has been enriched in carbon by the 3rd dredge-up. In the case of refractory elements, which have the property of condensing at high temperatures directly from gas into the solid state, the gas condenses into tiny particles, which then can grow into dust grains. Because of the large quantity of dust around them, AGB stars become obscured toward the end of their life and can only be seen as mid-infrared sources, since the dust absorbs the energy of the visual light coming from the star and reemits it as infrared light. Second, AGB stars are variable stars, meaning that their luminosity varies with time with changes occurring over relatively long periods >100 days. These luminosity variations are due to stellar pulsations, in the sense that the whole star expands and contracts. Pulsations produce changes in the stellar radius and temperature, which cause the variations in the stellar luminosity. When the pulsations attain a large amplitude they lead to strong stellar winds and a large mass-loss rate. Pulsation levitates matter above the photosphere and increases the wind density by about two orders of magnitude (Wood, 1979; Sedlmayr and Dominik, 1995; Dorfi et al, 2001).

The strong stellar winds driven by the combined effects of radiation pressure acting on dust and pulsation eventually erode the whole stellar envelope (Dupree, 1986; Willson, 2000). Hence, the winds govern the lifetime of AGB stars because when the envelope is almost completely lost the star moves away from the AGB phase into the hotter post-AGB phase. Toward the end of the post-AGB phase, the shell of material ejected by the AGB star may become illuminated by the radiation coming from the central star, and produce a planetary nebula. The former AGB stars is now referred to as a *planetary nebula nucleus* and finally turns into a cooling CO white dwarf.

3.4.4 Dust from Giant Stars and the Origin of Stardust

The specific dust species that form in the atmosphere of AGB stars depends mainly on the C/O ratio. The difference in the type of dust that can form in a carbon-rich or oxygen-rich gas is due to the strong bond of the CO molecules: if $O > C$, all carbon atoms are locked into CO and only oxygen-rich dust can form, viceversa, if $C > O$, all oxygen atoms are locked into CO and only carbon-rich dust can form⁷. In an oxygen-rich gas ($O > C$) dust species are, for example, Al₃O₂ (corundum),

⁷ This general rule is debated in the case of dust formation in supernova ejecta, see Chapter 2, Section 2.5.3

CaAl_2O_4 (hibonite), MgAl_2O_4 (spinel), as well as many different types of silicates (SiO , SiO_2 , etc). In a carbon-rich gas ($\text{C} > \text{O}$), dust species are, for example, SiC (silicon carbide), TiC (titanium carbide), and C itself (graphite).

Formation of dust around AGB stars is well documented by spectroscopic observations in the infrared (e.g., Treffers and Cohen, 1974; Speck et al, 2000, 2009) and predicted to occur by theoretical models (e.g., Fleischer et al, 1992; Lodders and Fegley, 1995; Gail and Sedlmayr, 1999; Ferrarotti and Gail, 2002). It is now widely accepted that AGB stars are the most prolific source of dust in the Galaxy. When summing up the contribution of the different families of late red giant and AGB stars: i.e., spectroscopically, the M stars, the OH/IR stars⁸, and the carbon stars, it results that $\sim 90\%$ of all dust of stellar origin in the interstellar medium came from these sources (Whittet, 1992).

Table 3.5 Meteoritic stardust grain types, populations, and origins^a

Type	Population	Origin
oxide and silicate grains	I	AGB stars
	II	AGB stars
	III	undetermined
	IV	supernovae
silicon carbide (SiC)	mainstream	AGB stars
	Y	AGB stars
	Z	AGB stars
	X	supernovae
	A+B	undetermined
	nova grains	novae
silicon nitride		supernovae
graphite	low-density	supernovae
	high-density	AGB, post-AGB
diamond		undetermined

^aTable 5.2 (Chapter 5) gives complementary information to this table.

Thus, it is not surprising that the vast majority of stardust grains extracted from meteorites (Chapter 2, Section 2.4. and Chapter 10, Section 2) show the signature of an origin in AGB stars (Table 3.5. The main signatures of AGB nucleosynthesis imprinted in meteoritic stardust grains are: (1) the O isotopic composition of the majority of oxide and silicate grains showing excess in ^{17}O and deficits in ^{18}O , and known as Population I and II of stardust oxide grains (Nittler et al, 1997), which match the O isotopic ratios observed around AGB stars via spectroscopic observations of CO molecular lines (e.g., Harris et al, 1987), and (2) the distribution of the $^{12}\text{C}/^{13}\text{C}$ ratios of $>90\%$ of SiC grains showing a peak between 50 and 60 (solar value is 89) and known as the *mainstream* SiC population, which match the distribution derived from spectroscopic observation of CO molecular lines in C-rich AGB stars (see Fig. 3 of Hoppe and Ott, 1997). The Ne composition measured in stardust SiC grains - corresponding to the Ne-E(H) component rich in ^{22}Ne is also

⁸ OH/IR stars are cool red giants with strong hydroxyl (OH) masers and infrared (IR) emissions.

a clear signature of material from the intershell of AGB stars, where ^{22}Ne is abundant. Moreover, the elemental and isotopic abundances of the heavy elements Kr, Sr, Zr, Ru, Xe (the Xe-S component), Ba, Nd, Sm, W, and Pb present in trace amount and measured in SiC grains clearly show the imprint of the *s*-process, which make inevitable their connection to AGB stars. Smaller SiC Populations Y and Z ($\simeq 1\%$ each of the total recovered stardust SiC grains) are also attributed to AGB stars, but of metallicity down to 1/3-1/5 of the solar value (Hoppe et al, 1997; Amari et al, 2001b; Zinner et al, 2006).

With regards to the remaining types and populations of stardust grains, core-collapse supernovae have been invoked as the origin site of Population X of SiC grains ($\sim 1\%$) and the few recovered silicon nitride grains (Nittler et al, 1995), showing excesses in ^{28}Si and evidence of the early presence of ^{44}Ti , as well as low-density graphite grains and Population IV of oxide and silicate grains (with excess in ^{18}O and ^{18}Si Vollmer et al, 2008; Travaglio et al, 1999, see Chapter 4). Novae are invoked for a few SiC grains of unusual composition (excesses in ^{13}C and ^{15}N Amari et al, 2001a, see Chapter 5, Section 2), while the origin of SiC grains of Populations A+B ($\simeq 5\%$ of all SiC grains, showing $^{13}\text{C}/^{12}\text{C} < 10$) is still unclear (Amari et al, 2001c). Oxide and silicate grains with deficits in both ^{17}O and ^{18}O , known as Population III, have been attributed to stars of metallicity lower than solar, however, the Si isotopic composition of the silicate grains belonging to this population is very close to solar, which does not support this interpretation. The origin of this population remains to be ascertained, together with the origin of high-density graphite grains and of the very abundant and extremely tiny (10^{-9} m) meteoritic diamond grains, the majority of which probably formed in the solar system. For more details in meteoritic stardust see, e.g., Clayton and Nittler (2004) and Lugaro (2005).

Given compelling evidence that most stardust came from AGB stars, the composition of these grains can be used as a stringent constraint for theoretical models of AGB stars and, viceversa, the models can be used to identify the mass and metallicity range of the parent stars of the grains. Data from the laboratory analysis of stardust are usually provided with high precision, down to a few percent errors, and for isotopic ratios. In comparison, data from spectroscopic observations of stellar atmospheres usually are provided with lower precision, errors typically $>50\%$, and mostly for elemental abundances. Thus, the information from stardust grains represents a breakthrough in the study of AGB nucleosynthesis. Also, given that the abundances and isotopic compositions of elements heavier than Al and lighter than Fe, such as Si and Ti, are mostly unaltered by AGB nucleosynthesis, laboratory analysis of these elements in AGB stardust can be used to constrain in great detail the initial composition of the parent star of the grains, and in turn the chemical evolution of the Galaxy (e.g., Zinner et al, 2006).

Meteoritic stardust provides us with abundant and precise information on radioactive nuclei in stars because the initial abundance of radioactive nuclei at the time of the formation of the grains is recorded by the signature of their radioactive decay inside the grains, which is easily derived from measurements of the excesses in the abundances of their daughter nuclei. An important example is that of ^{26}Al , where the initial ^{26}Al abundance in a stardust grain is revealed by excesses in ^{26}Mg .

This will be discussed in detail in Section 3.6.1. In general, radioactive signatures in stardust have the potential to be used as clocks for the timescale of dust formation around stars and supernovae (Hoppe and Besmehn, 2002). Finally, stardust isotopic data provide a unique way to investigate the operation of the s -process in AGB stars, as will be discussed in Section 3.5.5.

3.5 Neutron-Capture Nucleosynthesis in AGB Stars

In this section we show that:

- Free neutrons are produced in the TP-AGB phase by the $^{22}\text{Ne}(\alpha, n)^{25}\text{Mg}$ reaction, which activates at $\sim 300\text{MK}$ and operates during He burning in the intershell convective region during thermal pulses, and the $^{13}\text{C}(\alpha, n)^{16}\text{O}$ reaction, which activates at $\sim 90\text{MK}$ and operates in a radiative (and hence stable) region of the intershell during the H-burning phases. The free neutrons trigger the s -process, which produces half of the cosmic abundances of the elements heavier than iron via neutron captures mostly occurring on stable and long-lived radioactive nuclei.
- Unstable isotopes with half lives higher than a few days can also suffer neutron captures during the s -process, producing a wide variety of *branching points* on the s -process path, which define the details of the abundance distribution produced by the s -process as a function of neutron density and temperature.
- The overall s -process abundance distribution is defined by stable nuclei with a magic number of neutrons at the three s -process peaks at Sr, Ba, and Pb, and by the total amount of free neutrons available.
- Several long-lived unstable isotopes are produced by the s -process (details in Section 3.6.5). Among them are ^{93}Zr and ^{99}Tc . Observations of monoisotopic stable Nb (the daughter nucleus of ^{93}Zr) and of Tc itself can be used as discriminant between intrinsic (on the AGB) and extrinsic (with a former AGB binary companion) s -process-enhanced stars.

3.5.1 Neutron Sources in AGB Stars

In the double burning shell phase a nuclear reaction that may produce a copious neutron flux is $^{22}\text{Ne}(\alpha, n)^{25}\text{Mg}$. ^{22}Ne is abundantly present in the intershell because it directly derives from the initial abundance of O (the most abundant nucleus after H and He) as a consequence of the operation of the CNO cycle first and of a double α capture on ^{14}N later. This means that this neutron production channel is of *secondary* origin, i.e., its efficiency scales with the initial metallicity of the star. The relatively high Coulomb barrier of Ne ($Z=10$) pushes the threshold temperature for α capture above 300 MK so that this process can activate only within a hot He-burning region.

Since the temperature at the base of the He convective shell during thermal pulses scales directly with the mass of the H-exhausted core, only stars initially more massive than $\simeq 3 M_{\odot}$ (Iben, 1975; Iben and Truran, 1978) can efficiently activate this nuclear reaction. Panel b) in Fig. 3.9, shows a typical profile of the neutron density versus time associated with this neutron source. Its shape reflects the sharp rise of the temperature caused by the growth of the thermal instability and the following quite rapid decline due to the quenching of the instability. The high activation temperature and its very short duration (a few years) lead to a very high initial neutron density (reaching up to $N_n \simeq 10^{14} \text{ n/cm}^3$ in AGB stars of initial mass $\sim 6 M_{\odot}$) but to a small total amount of ^{22}Ne burnt per cycle, so that the total number of neutrons released, i.e., the time-integrated neutron flux, or *neutron exposure* $\tau = \int_0^t N_n v_{th} dt$, remains quite small, of the order of a few hundredth of $1/\text{mbarn} = 1/10^{-27} \text{ cm}^2$ (see Section 3.5.2). The signature of such an impulsive neutron flux on neutron-capture nucleosynthesis will be discussed in the next section. We only remark here an important difference between the neutron-capture nucleosynthesis occurring during AGB thermal pulses and that occurring in the He-convective shell of a massive star (other than the fact that in the AGB case the exposure to neutrons occurs recurrently): the mass of the He-convective shell in AGB stars is orders of magnitude smaller than that of a massive star so that the smaller dilution induced by the mixing allows, in the former case, many unstable nuclei to reach a higher equilibrium concentration. This occurrence favors the synthesis of stable nuclei on the neutron-rich side of the valley of β stability.

The problem with the ^{22}Ne neutron source is that AGB stars observed to be enriched in *s*-process elements have been identified as AGB stars of masses lower than $\sim 3 M_{\odot}$ because a) their relatively low luminosities (Frogel et al, 1990) match those of low-mass AGB models; b) their surface is generally C enriched, an occurrence that rules out a significant HBB and hence an initial mass greater than $3 M_{\odot}$; c) excesses of ^{25}Mg , predicted to be produced by $^{22}\text{Ne}(\alpha, n)^{25}\text{Mg}$, and of ^{26}Mg , predicted to be produced by the twin channel $^{22}\text{Ne}(\alpha, \gamma)^{26}\text{Mg}$, with respect to ^{24}Mg are not observed (Smith and Lambert, 1986; McWilliam and Lambert, 1988); d) the high neutron density produced by the ^{22}Ne channel, see Panel b) in Fig. 3.9, would favor the synthesis of neutron-rich nuclei like ^{96}Zr and elements as Rb, at odds with spectroscopic observations (Lambert et al, 1995; Abia et al, 2001) and the solar abundance distribution (Despain, 1980). Thus, for the vast majority of *s*-enhanced AGB stars, another nuclear fuel for the production of neutrons has to be invoked.

Nuclei of ^{13}C are the best candidate for this role, given that the $^{13}\text{C}(\alpha, n)^{16}\text{O}$ reaction activates at temperatures from approximately 90 MK, which are easily reached in low-mass AGB stars. The achievement of the threshold temperature is, however, a necessary but not sufficient condition for a nuclear reaction to be effective: an additional requirement is the presence of a sufficient amount of reactants, in this case ^{13}C . Models in which no mixing is allowed in the layers in radiative equilibrium do not naturally produce a significant concentration of ^{13}C in the intershell region (see end of Section 3.4.1). In fact, the ^{13}C available in the H-exhausted zone is that corresponding to the equilibrium value provided by the CNO cycle. As a neutron source for the *s*-process, this ^{13}C suffers two major problems: its abundance is too

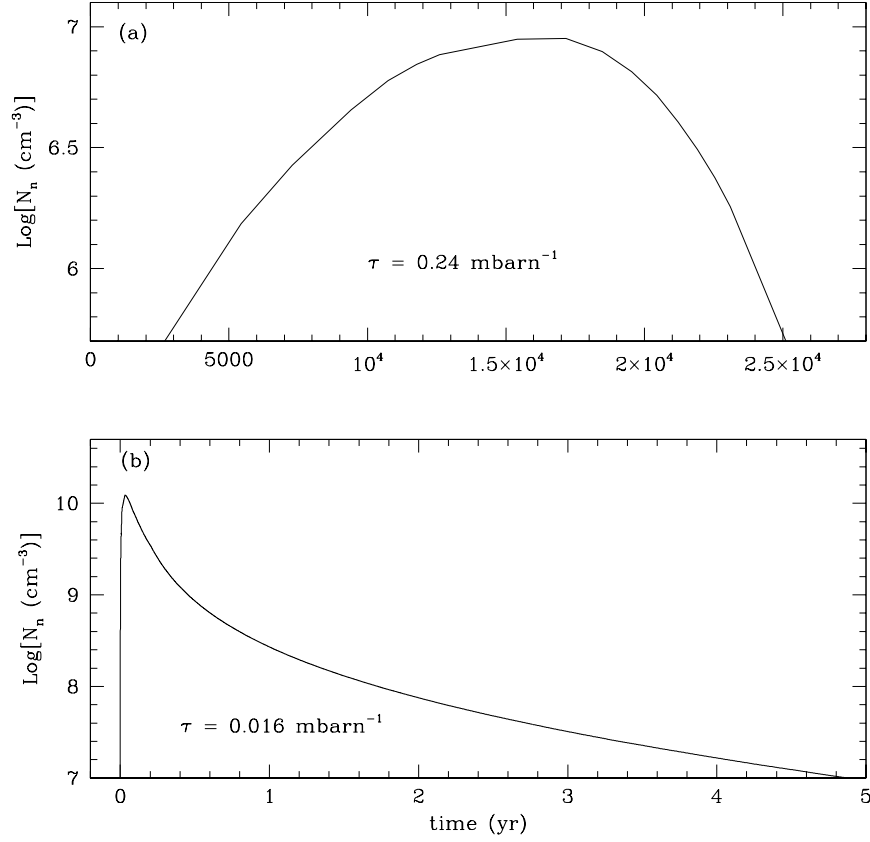


Fig. 3.9 Neutron densities as functions of time corresponding to the activation of the two neutron sources in a $3 M_{\odot}$ AGB star model of solar metallicity during the last interpulse-pulse cycle: (a) the ^{13}C neutron source (the zero point in time represent the time from the start of the interpulse period, about 10,000 yr, when the temperature reaches 79 MK); (b) the ^{22}Ne neutron source (the zero in time corresponds to the time when the temperature in the TP reaches 250 MK).

low to power a significant neutron flux and its ratio with respect to ^{14}N is too low ($^{13}\text{C}/^{14}\text{N} \ll 1$). The $^{14}\text{N}(n, p)^{14}\text{C}$ reaction⁹ has a relatively high neutron-capture cross section of $\simeq 2$ mbarn, with respect to typical cross section of the order of 0.1-0.01 mbarn for the light nuclei. Hence, it is a formidable poison that can even completely inhibit the s -process. Hence, the ^{13}C neutron source represents a valid alternative to the ^{22}Ne neutron source only if additional ^{13}C is produced in an environment depleted in ^{14}N . A way out of this problem is to assume that at the end

⁹ This reaction produces ^{14}C , a radioactive nucleus with a half life of 5730 yr. This nucleus is not carried to the stellar surface by the 3rd dredge-up because it is destroyed by $^{14}\text{C}(\alpha, \gamma)^{18}\text{O}$ reactions during He-burning in the thermal pulse.

of each 3^{rd} dredge-up episode a small amount of protons penetrates the intershell region. The amount of protons engulfed in the He/C rich intershell must be small ($Y_p/Y_{12C} \ll 1$) because they must allow the conversion of ^{12}C into ^{13}C , but not the conversion of ^{13}C in ^{14}N . (Note that the intershell is essentially free of ^{14}N at the end of a thermal pulse because ^{14}N nuclei have all been destroyed by α captures.) Once a small amount of protons has penetrated the intershell, the progressive heating caused by the deposition of fresh He synthesized by the H-burning shell induces the conversion of ^{12}C in ^{13}C . We can estimate the concentration of protons that allows the build up of ^{13}C , but not of ^{14}N , by considering that the production rate of ^{14}N equates that of ^{13}C when the concentration of ^{13}C rises to a value of the order of 1/4 of that of ^{12}C . Since the mass fraction of ^{12}C in the intershell is about 0.2, the two rates equate each other for a ^{13}C concentration of $X_{13C} \simeq 0.20 (13/12)/4 = 5 \cdot 10^{-2}$. If one requires the ^{13}C production rate to dominate that of ^{14}N , the ^{13}C concentration must be reduced by at least a factor of 10, so that $X_{13C} \simeq 5 \cdot 10^{-3}$. This abundance of ^{13}C corresponds to a proton concentration of the order of $X_p = X_{13C}/13 = 4 \cdot 10^{-4}$.

A self-consistent scenario able to produce this small amount of protons penetrating below the base of the convective envelope has not been found yet: several mechanisms have been proposed (e.g., Iben and Renzini, 1982; Herwig et al, 1997; Langer et al, 1999; Denissenkov and Tout, 2003) but none of them can presently be considered as widely accepted. A discussion of these alternative scenarios goes well beyond the purposes of the present discussion. What matters, and what modelers often pragmatically assume, is that a small amount of protons definitely penetrates in the intershell at the end of 3^{rd} dredge-up. The detailed features of the ^{13}C pocket obtained with such a procedure are subject to large uncertainties.

Nonetheless the basic properties of the neutron flux that is obtained in this way are considered relatively well understood (Gallino et al, 1998; Goriely and Mowlavi, 2000; Lugaro et al, 2003b). The activation of the $^{13}\text{C}(\alpha, n)^{16}\text{O}$ occurs well before the onset of the next thermal pulse and the s -process nucleosynthesis triggered by this neutron source occurs at low temperature in a radiative environment (see Section 3.5.2). Panel a) in Fig. 3.9 shows the temporal evolution of this neutron flux. The rather long timescale over which this neutron flux remains active is determined by the speed at which the H-burning shell accretes matter on the He core, which means a typical timescale of the order of 10^4 yr. Given such a long timescale, ^{13}C is totally consumed so that the total number of neutrons released is very large, with neutron exposures of the order of a tenth to a few mbarn $^{-1}$. The neutron density, instead, keeps to low values, up to $N_n \simeq 10^8$ n/cm 3 . Let us finally remark that the neutron flux produced by the ^{13}C neutron source is of *primary* origin, i.e., independent on the initial stellar metallicity, since the ^{13}C is made from ^{12}C synthesized starting from the initial H and He.

3.5.2 The *s*-Process in AGB Stars

A fraction of the free neutrons produced in AGB stars by the ^{13}C and ^{22}Ne neutron sources described above is captured by Fe seed nuclei, leading to production of elements with large atomic mass numbers up to Pb ($A = 208$) and Bi ($A = 209$) via the *s*-process. In general, a neutron flux that irradiates the surrounding matter reproduces a situation analogous to that occurring during H burning, where matter is irradiated by a flux of protons. While during a proton flux matter is pushed out of the valley of β stability toward the proton-rich side, during a neutron flux matter is pushed out of the valley of β stability valley toward the neutron-rich side. Thus, the presence of a neutron flux is inevitably associated to the synthesis of radioactive nuclei that, sooner or later, decay back towards the valley of β stability.

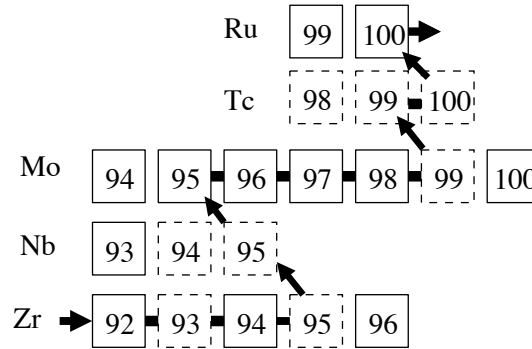


Fig. 3.10 The main *s*-process path along the valley of β stability from Zr to Ru is indicated by the thick solid line and arrows. Solid and dashed boxes represent stable and unstable nuclei, respectively. The radioactive nuclei ^{93}Zr and ^{99}Tc behave as stable during the *s*-process as their half lives (of the order of 10^5 - 10^6 yr) are longer than the timescale of the *s*-process.

During the *s*-process, by definition, the timescale against β decay of an unstable isotope is shorter than its timescale against neutron captures. Thus, neutron captures occur only along the valley of β stability (Fig. 3.10). For this condition to hold neutron densities must be of the order of $N_n \sim 10^7 \text{ n/cm}^3$. By comparison, during the *rapid* neutron-capture process (*r*-process), neutron densities reach values as high as 10^{25} n/cm^3 so that neutron captures occur on a time scale less than a second (typically much shorter than that of radioactive decays) pushing matter towards very neutron-rich material. When the neutron flux is extinguished, the neutron-rich radioactive nuclei quickly decay back towards their stable isobars on the valley of β stability. As presented in Chapter 4, the *r*-process is believed to occur in explosive conditions in supernovae.

In stellar conditions, though, neutron densities during the *s*-process can reach values orders of magnitude higher than 10^7 n/cm^3 . Depending on the peak neutron density, as well as on the temperature and density, which can affect β -decay rates, conditions may occur for the neutron-capture reaction rate of an unstable isotope to

compete with its decay rate. These unstable isotopes are known as *branching points* on the *s*-process path. To calculate the fraction of the *s*-process flux branching off the main *s*-process path at a given branching point a *branching factor* is defined as:

$$f_{branch} = \frac{p_{branch}}{p_{branch} + p_{main}},$$

where p_{branch} and p_{main} are the probabilities per unit time associated to the nuclear reactions suffered by the branching point nucleus and leading onto the branch or onto the main path of the *s*-process, respectively.

There are several types of branching points: in the *classical* case p_{main} corresponds to λ , i.e., the probability per unit time of the unstable isotope to decay, and p_{branch} corresponds to p_n , i.e., the probability per unit time of the unstable isotope to capture a neutron $\langle \sigma v \rangle N_n$, where N_n is the neutron density and $\langle \sigma v \rangle$ is the Maxwellian averaged product of the velocity v and the neutron-capture cross section σ .¹⁰ A typical example of this case is the isotope ^{95}Zr in Fig. 3.10, which has a half life of 64 days, and can capture neutrons and produce the neutron-rich isotope ^{96}Zr , classically a product of the *r*-process, even during the *s*-process. When the branching point is a long-lived, or even stable isotope, but its β -decay rate increases with temperature, the opposite applies: $p_{branch}=\lambda$ and $p_{main}=p_n$. In even more complex situations, a radioactive isotope may suffer both β^+ and β^- decays, as well as neutron captures. In this case, three terms must be considered at denominators in the definition of the branching factor above: p_n , and λ for both β^+ and β^- decays.

Branching points have been fundamental in our understanding of the *s*-process conditions in AGB stars and will be discussed in more detail in Section 3.5.3. The low neutron density associated with the ^{13}C neutron source does not typically allow the opening of branching points. On the other hand, the high neutron density associated with the ^{22}Ne neutron source activate the operation of branching points on the *s*-process path, defining the details of the final abundance distribution.

It is possible to identify nuclei that can be produced only by the *s*-process (*s-only* nuclei), which are shielded from *r*-process production by a stable isobar, or only by the *r*-process (*r-only* nuclei), which are not reached by neutron captures during the *s*-process as isotopes of the same element and same atomic mass number $A - 1$ are unstable. Examples of *s*-only nuclei are ^{96}Mo and ^{100}Ru shown in Fig. 3.10, which are shielded by the *r*-only nuclei ^{96}Zr and ^{100}Mo , respectively. These, in turn, are not typically produced by the *s*-process as ^{95}Zr and ^{99}Mo are unstable. Proton-rich nuclei which cannot be reached by either the *s*- or the *r*-process must be produced via the *p*-process, i.e., proton captures or photodisintegration of heavier nuclei, and are labelled as *p-only* nuclei (e.g., ^{94}Mo in Fig.3.10).

¹⁰ Note that σ is usually given in mbarn, corresponding to 10^{-27} cm^2 , and that $\langle \sigma v \rangle$ can be approximated to $\sigma \times v_{thermal}$, where $v_{thermal}$ is the thermal velocity. Neutron-capture cross sections for (n, γ) reactions throughout this chapter are given at a temperature of 350 million degrees, corresponding to an energy of 30 keV, at which these rates are traditionally given. Values reported are from the KADONIS database (Karlsruhe Astrophysical Database of Nucleosynthesis in Stars, <http://www.kadonis.org/>) and the JINA reaclib database (<http://groups.nsl.msu.edu/jina/reaclib/db/index.php>), unless stated otherwise.

Models for the s -process have historically been tested against the solar system abundances of the s -only isotopes, as these were the first precise available constraints. Once a satisfactory fit is found to these abundances, the selected theoretical distribution can be used to determine the contribution from the s -process to each element and isotope. By subtracting this contribution to the total solar system abundance, an r -process contribution to each element can be obtained¹¹ (e.g., Kaeppeler et al, 1982; Arlandini et al, 1999), which has been widely used to test r -process models, and to compare to spectroscopic observations of stars showing the signature of the r -process (Snedden et al, 2008). For example, it is found that $\simeq 80\%$ of the solar abundance of Ba is due to the s -process, which is then classified as a typical s -process element, while $\simeq 5\%$ of the solar abundance of Eu is due to the s -process, which is then classified as a typical r -process element.

Already B²FH had attributed to the operation of the s -process the three peaks in the solar abundance distribution at magic numbers of neutrons $N=50$, the Sr, Y, and Zr peak, $N=82$, the Ba and La peak, and $N=126$, the Pb peak. This is because nuclei with a magic number of neutrons behave with respect to neutron-capture reactions in a similar way as atoms of noble gases do with respect to chemical reactions. Their energy levels, or shells, are fully populated by neutrons, in the case of magic nuclei, or by electrons, in the case of noble gases, and hence they are very stable and have a very low probability of capturing another neutron, in the case of magic nuclei, or of sharing electrons with another atom, in the case of noble gases. Nuclei with magic numbers of neutrons have small neutron-capture cross sections (of the order of a few to a few tens mbarn) with respect to other heavy nuclei, and they act as bottlenecks along the s -process path, leading to the observed abundance peaks. Nuclei located between the peaks, instead, have much higher neutron-capture cross sections (of the order of a few hundred to a few thousand mbarn). The neutron-capture chain in these local regions in-between magic nuclei quickly reaches equilibrium during the s -process. During a neutron-capture process the abundance N_A of a stable isotope with atomic mass A varies with time as:

$$\begin{aligned}\frac{dN_A}{dt} &= \text{production term} - \text{destruction term} \\ &= N_{A-1}N_n\sigma_{A-1} \times v_{\text{thermal}} - N_A N_n \sigma_A \times v_{\text{thermal}}.\end{aligned}$$

When replacing time with the neutron exposure τ one has:

$$\frac{dN_A}{d\tau} = N_{A-1}\sigma_{A-1} - N_A\sigma_A,$$

which, in steady-state conditions $\frac{dN_A}{d\tau} \rightarrow 0$ reached in between neutron magic nuclei, yields the simple rule to derive relative s -process abundances away from neutron magic numbers¹²:

¹¹ The p -process contribution to elemental abundances is comparatively very small, $\simeq 1\%$, except in the case of Mo and Ru, which have magic and close-to-magic p -only isotopes, where it is up to $\simeq 25\%$ and $\simeq 7\%$, respectively.

¹² For a detailed analytical description of the s -process refer to Chapter 7 of Clayton (1968).

$$N_A \sigma_A \simeq \text{constant}.$$

It follows that the relative abundances of nuclei in-between the peaks are only constrained by their neutron-capture cross sections and do not provide information on the *s*-process neutron exposure. On the other hand, the relative abundances of the elements belonging to the three different peaks almost uniquely constrain the *s*-process neutron exposure. This is the reason behind the introduction and wide usage, both theoretically and observationally, of the *s*-process labels *light s* (*ls*) and *heavy s* (*hs*), corresponding to the average abundances of the *s*-process elements belonging to the first and second peak, respectively, as well as behind the importance of the determination of the abundance of Pb, representing the third *s*-process peak. In AGB stars, the high neutron exposure associated with the ^{13}C neutron source drive the production of *s*-process elements even reaching up to the third *s*-process peak at Pb in low-metallicity AGB stars. On the other hand, the lower neutron exposure associated with the ^{22}Ne neutron source typically produces *s*-elements only up to the first *s*-process peak at Sr.

It is now ascertained that the *s*-process is responsible for the production of about half the abundances of the elements between Sr and Bi in the Universe (see, e.g., Kaeppeler et al, 1982) and that it occurs in AGB stars¹³. The first direct evidence that the *s*-process occurs in AGB stars - and, more generally, that nucleosynthesis is happening inside stars - was the identification in the 1950s of the absorption lines of atoms of the radioactive element Tc in the atmospheres of some cool giant stars. The longest-living isotopes of Tc are ^{97}Tc and ^{98}Tc , with a half life of 4.0 and 4.2 million years, respectively. Since these stars would have taken billions of years to evolve to the giant phase, the observed Tc could have not been present in the star initially. It follows that the Tc must have been produced by the *s*-process inside the stars. Actually, neutron captures do not produce $^{97,98}\text{Tc}$, but the third longest-living isotope of this element: ^{99}Tc (Fig. 3.10), which has a terrestrial half life of 0.21 million years. The presence of ^{99}Tc in AGB stars has been confirmed by measurements of the Ru isotopic composition in stardust SiC grains, as will be discussed in Section 3.6.5.

The observation of Tc in giant stars has also been used to classify different types of *s*-process enhanced stars. If a given observed *s*-process enriched giant star shows the lines of Tc, then it must be on the AGB and have enriched itself of *s*-process elements. In this case it is classified as *intrinsic s*-process enhanced star and typically belongs to one of the reddest and coolest subclasses of the spectroscopic class M: MS, S, SC, and C(N), where the different labels indicate specific spectral properties - S stars show zirconium oxide lines on top of the titanium oxide lines present in some M stars and C(N) stars have more carbon than oxygen in their atmospheres - or the transition cases between those properties - MS is the transition case between M stars and S stars and SC is the transition case between S and C(N) stars. On the other hand, if an *s*-process enriched giant star does not show the lines of

¹³ Cosmic abundances of nuclei between Fe and Sr are also contributed by the *s*-process, but in this case by neutron captures occurring in massive stars during core He burning and shell C burning (Chapter 4 and, e.g., Raiteri et al, 1992).

Tc, it is classified as *extrinsic s*-process enhanced star. In this case its *s*-process enhancements have resulted from mass transfer from a binary companion, which was more massive and hence evolved first on the AGB phase. Stars belonging to the class of *extrinsic s*-process enhanced stars range from Ba stars in the Galactic disk, to the older halo populations of carbon-rich CH and Carbon-Enhanced Metal-Poor (CEMP) stars (e.g., Jorissen et al, 1998; Bond et al, 2000; Lucatello et al, 2005). Observations of Nb can also be used to discriminate intrinsic from extrinsic *s*-process enhanced stars as Nb is destroyed during the *s*-process, but receives a radiogenic contribution over time due to the β^- decay of ^{93}Zr , with half life 1.5 million yr, which is on the *s*-process path (see Fig. 3.10).

3.5.3 Branchings and the *s*-Process in AGB Stars

Branching points at radioactive nuclei have provided for the past 50 years important tools to learn about conditions during the *s*-process in AGB stars. This is because branching factors depend on the neutron density and can also depend on the temperature and density of the stellar material. This happens in those cases when the decay rate of the branching nucleus is temperature and/or density dependent. These branching points are referred to as *thermometers* for the *s*-process. Traditionally, the solar abundances of isotopes affected by branching points were used to predict the neutron density and temperature at the *s*-process site using parametric models where parameters representing, e.g., the temperature and the neutron density were varied freely in order to match the observed abundances (e.g., Kaeppeler et al, 1982). Later, detailed information on branching points became available from spectroscopic observations of stellar atmospheres and from laboratory analyses of meteoritic stellar grains. At the same time, models for the *s*-process in AGB stars have evolved from parametric into stellar models, where the temperature and neutron density parameters governing the *s*-process are taken from detailed computation of the evolution of stellar structure (Gallino et al, 1998; Goriely and Mowlavi, 2000; Cristallo et al, 2009). For these models branching points are particularly useful to constrain neutron-capture nucleosynthesis and conditions inside the thermal pulse because, typically, they open at high neutron densities during the high-temperature conditions that allow the activation of the ^{22}Ne neutron source in the convective intershell region.

As the temperature, density, and neutron density vary with time in the convective intershell region, branching factors also change over time. For example, a classical branching point, where the branching path corresponds to neutron capture, progressively opens while the neutron density reaches its maximum, and then closes again while the neutron density decreases and the main *s*-process path is restored. Of special interest is that toward the end of the thermal pulse the neutron density always decreases monotonically with the temperature and thus with time (Fig. 3.9) so that a *freeze out* time can be determined for a given nucleus, which represents the time after which the probability that the nucleus captures a neutron is smaller than unity

and thus the abundances are *frozen* (Cosner et al, 1980). This can be calculated as the time when the neutron exposure τ left before the end of the neutron flux is $1/\sigma$, where σ is the neutron-capture cross section of the nucleus. Hence, the abundances determined by branching points defined by unstable isotopes with higher σ freeze out later during the neutron flux.

As a general rule of thumb, branching points that have the chance of being activated at the neutron densities reached in AGB stars are those corresponding to radioactive nuclei with half lives longer than at least a couple days. These correspond to similar half lives against capturing a neutron for neutron densities $\simeq 10^9 - 10^{11}$ n/cm³, at AGB *s*-process temperatures. Isotopes with half lives longer than approximately 10,000 yrs can be considered stable in this context as the *s*-process flux in AGB stars typically lasts less than this time. We refer to these isotopes as long-lived isotopes and we discuss their production in AGB stars in detail in Section 3.6.5. Very long-lived isotopes - half lives longer than ~ 10 Myr - include for example ⁸⁷Rb, and are considered stable in our context.

A list of unstable isotopes at which branching points that become relevant in the *s*-process reaction chain in AGB stars is presented in Appendix B of this book as a complete reference to be compared against observational information and as a tool for the building of *s*-process networks. Worth special mention are the branching points at ⁷⁹Se, ⁸⁵Kr, and ¹⁷⁶Lu for the involvement of isomeric states of these nuclei, at ¹⁵¹Sm, one among a limited number of branching points for which an experimental estimate of the neutron-capture cross section is available, at ⁸⁶Rb, responsible for the production of the very long-living ⁸⁷Rb, and at ¹⁶³Dy and ¹⁷⁹Hf, which are stable nuclei in terrestrial conditions that become unstable in AGB stellar interiors.

Taken as a whole, the list of branching points that may be operating during the *s*-process in AGB stars sets a powerful group of constraints on our theoretical *s*-process scenarios. They are particularly effective when each of them is matched to the most detailed available observations of its effects. For example, some elemental abundance ratios and isotopic ratios that are affected by branching points can be measured from a stellar spectrum via identification and analysis of different emission or absorption lines. In these cases, model predictions can be compared directly to stellar observations of *s*-process enhanced stars (Section 3.5.4). Isotopic ratios affected by branching points involving isotopes of refractory elements, but also of noble gases, have been or have the potential to be measured in meteoritic stardust SiC grains from AGB stars and provide unique constraints due to the large and expanding high-precision dataset available on the composition of stardust (Section 3.5.5). The values of the solar abundance ratios of *s*-only isotopes affected by branching points (e.g., ¹³⁴Ba/¹³⁶Ba, ¹²⁸Xe/¹³⁰Xe, and ¹⁷⁶Hf/¹⁷⁶Lu) must be matched by any *s*-process model. When these involve nuclei with peculiar structure, such as ¹⁷⁶Lu, combined investigation of nuclear properties and *s*-process models drives progress in our understanding of both.

One advantage of the computation of branching points in AGB stars is that the activation of one branching point is almost completely independent from the activation of all the other branching points because the overall neutron flux is only very marginally affected by the details of the *s*-process path. Thus, it is possible to

include in a s -process nuclear network only the branching points of interest for a specific problem, or a specific element, hence keeping it simple and saving computational time.

One overall drawback of using branching points to understand the s -process is that for the vast majority of the radioactive nuclei involved there exist only theoretical or phenomenological determinations of their neutron-capture cross sections and of the temperature and density dependence of their decay rates. This is due to the difficulty of producing experimental data for radioactive targets (see Chapter 9) and means that there are always some uncertainties associated to model predictions of the effect of branching points. These errors and their effect need to be carefully evaluated in every single case.

3.5.4 Signatures of s -Process Branching Points in Stars: Rb, Zr, Eu

The abundance of ^{87}Rb , which can be produced in AGB stars via activation of the branching point at ^{86}Rb , is a famous example of how detailed comparison of theoretical s -process abundances to the abundances observed in s -process enhanced stars provide a stringent test to our understanding of the s -process and AGB stars. The abundance of ^{87}Rb is particularly interesting because the element Rb can be spectroscopically identified and its abundance determined in AGB stars. Overall, Rb is an r -process element - only 22% of its solar abundance can be ascribed to the s -process (Arlandini et al, 1999) - made up of two isotopes: ^{85}Rb and the very long-lived ^{87}Rb , which is treated as a stable isotope in this context. Specifically, 92% of solar ^{85}Rb is made by the r -process because this nucleus has a relatively large neutron-capture cross section of 234 mbarn and thus it does not accumulate to high abundances during the s -process. On the other hand, ^{87}Rb , as described in Appendix B, has a magic number of neutrons $N=50$, and thus a relatively small neutron-capture cross section of 15.7 mbarn. Hence, if it is reached by the s -process reaction chain via the activation of the branching points at ^{85}Kr and ^{86}Rb , it accumulates and is significantly produced. It follows that when these branching points are activated during the s -process, the abundance ^{87}Rb represents a fraction of the total abundance of s -process Rb larger than the initial solar fraction. This is illustrated in the top panel of Fig. 3.11. In the case of the massive AGB model, where the ^{22}Ne neutron source is activated, the s -process occurs at high neutron density, and branching points are open, almost half of the final total abundance of Rb is made by ^{87}Rb . In the case of the low-mass AGB model, instead, where the ^{13}C neutron source is activated, the s -process occurs at low neutron density, and branching points are closed, only a quarter of the final total abundance of Rb is made by ^{87}Rb .

The ratio of the abundance of Rb to that of a neighbouring s -process element, such as Sr, or Zr, whose overall abundance is instead not affected by the activation of branching points, can be determined in AGB stars and has been widely used as an indicator of the neutron density at which the s -process occurs. Observations of Rb/Zr ratios lower than solar in MS, S, and C stars have strongly supported the

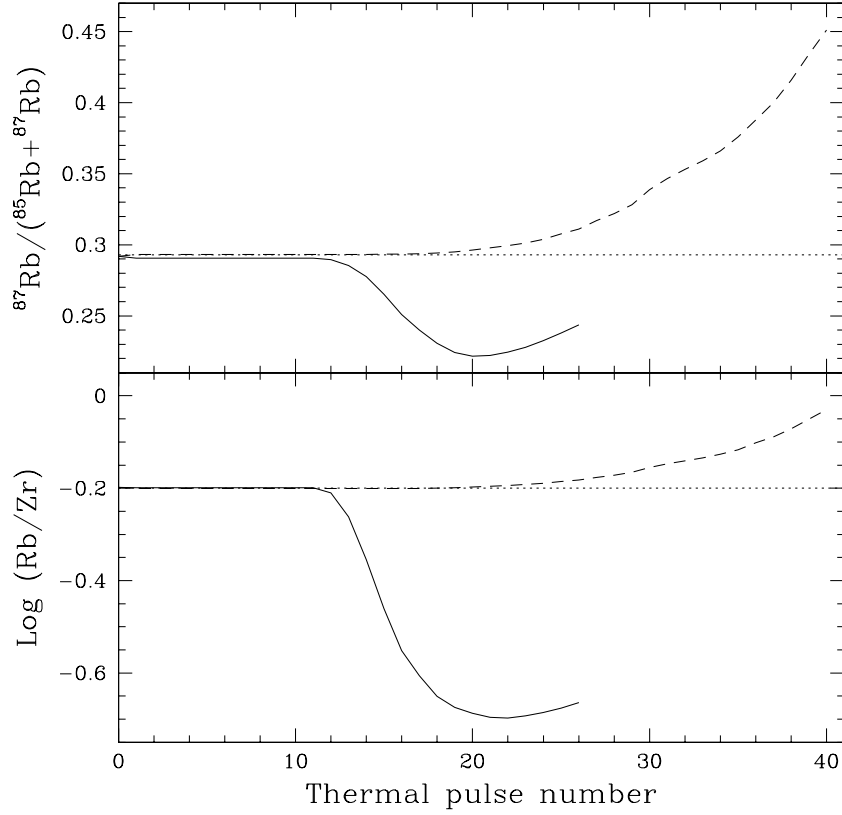


Fig. 3.11 Ratio of ^{87}Rb to the total abundance of Rb (top panel) and the Rb/Zr ratio (lower panel) computed in two solar metallicity AGB models (from van Raai et al, 2008a). The dotted lines represent the initial solar ratios. The evolution lines represent a massive ($6.5 M_{\odot}$) AGB model experiencing the activation of the ^{22}Ne neutron source only (long-dashed lines), and a low-mass ($3 M_{\odot}$) model experiencing the activation of the ^{13}C neutron source only (solid lines, except for a marginal activation of the ^{22}Ne neutron source in the latest thermal pulses leading to the small final increase in the ^{87}Rb and Rb abundances).

theoretical scenario where the main neutron source in these low-mass AGB stars is the $^{13}\text{C}(\alpha, n)^{16}\text{O}$ reaction. This is because this neutron source produces neutron densities too low to increase the Rb/Zr ratio above the solar value (see lower panel of Fig. 3.11 and Lambert et al, 1995; Abia et al, 2001).

Massive AGB stars ($> 4.5 M_{\odot}$) have only recently been identified in our Galaxy (García-Hernández et al, 2006, 2007). They belong to the group of OH/IR stars and they have been singled out as massive AGB stars on the basis of their location closer to the galactic plane, which indicates that they belong to a younger and thus more massive stellar population, and their longer pulsation periods ($\simeq 400$ days). Rb/Zr

ratios in these stars are observed to be well above the solar value, which has given ground to the theoretical scenario where the main neutron source in these massive AGB stars must be the $^{22}\text{Ne}(\alpha, n)^{25}\text{Mg}$ reaction, which produces neutron densities high enough to increase the Rb/Zr ratio above the solar value (see lower panel of Fig. 3.11).

Another indicator of the neutron density in AGB stars is the isotopic abundance of ^{96}Zr , which is produced if the branching point at ^{95}Zr is activated. Zr isotopic ratios were determined via observations of molecular lines of ZrO in a sample of S stars (Lambert et al, 1995). No evidence was found for the presence of ^{96}Zr in these stars. This result provides further evidence that the neutron density in low-mass AGB stars must be low. A low ^{96}Zr abundance has been confirmed by high-precision data of the Zr isotopic ratios in stardust SiC grains, which are discussed in the following Section 3.5.5.

Isotopic information from stellar spectra has also been derived for the typical r -process element Eu in old Main Sequence stars belonging to the halo of our Galaxy and enhanced in heavy neutron-capture elements (Snedden et al, 2008). This has been possible because the atomic lines of Eu differ significantly if the Eu atoms are made of ^{151}Eu instead of ^{153}Eu , the two stable isotopes of Eu. In old stars showing overall enhancements of r -process elements, the total Eu abundance is roughly equally divided between ^{151}Eu and ^{153}Eu . This fraction is consistent with the solar fraction, and it is expected by Eu production due to the r -process (Snedden et al, 2002; Aoki et al, 2003a). On the other hand, in two old stars showing overall enhancements in s - and r -process elements, roughly 60% of Eu is in the form of ^{151}Eu (Aoki et al, 2003b). How these stars gained enhancements in the abundances of both r - and s -process elements is an unsolved puzzle of the study of the origin of the elements heavier than iron in the Galaxy (Jonsell et al, 2006). This is because according to our current knowledge, the r - and the s -process are completely independent of each other, and occur in very different types of stars, core-collapse supernovae and AGB stars, respectively. During the s -process, the Eu isotopic fraction is determined mostly by the activation of the branching point at ^{151}Sm , and the observed 60% value is consistent with low neutron densities $\simeq 10^8 \text{ n/cm}^3$ during the s -process. As more observations become available, the role of branching points during the s -process in AGB stars becomes more and more crucial to answering the questions on the origin of the heavy elements.

3.5.5 SiC Grains from AGB Stars and Branching Points

Stardust SiC grains from AGB stars represent a unique opportunity to study s -process conditions in the parent stars of the grains through the effect of the operation of branching points because SiC grains contain trace amounts of atoms of elements heavier than iron, which allow high-precision measurements of their isotopic ratios. Refractory heavy elements, such as Sr, Ba, Nd, and Sm, condensed from the stellar gas directly into the SiC grains while the grains were forming. Their isotopic

composition have been determined from samples of meteoritic residual materials containing a large number of SiC grains using TIMS and SIMS (see Chapter 10, Section 2 and Ott and Begemann, 1990; Zinner et al, 1991; Prombo et al, 1993; Podosek et al, 2004). High-resolution SIMS has also been applied to derive data in single stardust SiC grains for Ba with the NanoSIMS (see Chapter 10, Section 2 and Marhas et al, 2007) and Eu with the SHRIMP (Sensitive High Resolution Ion Microprobe, Terada et al, 2006). Isotopic ratios in a sample containing a large number of SiC grains for many elements in the mass range from Ba to Hf were also measured by ICPMS (Chapter 10, Section 2 and Yin et al, 2006).

A general drawback of these experimental methods is that they do not allow to separate ions of same mass but different elements. Hence, interferences by isotopes of the same mass (isobars) are present, which is especially problematic for the elements heavier than iron where a large number of stable isobars can be found. Branching points, in particular, by definition affect the relative abundances of isobars, thus, with the methods above it is difficult to derive precise constraints on the effect of branching points on isotopic ratios. For example, the isobars ^{96}Mo and ^{96}Zr cannot be distinguished in these measurements, and thus it is not possible to derive information on the operation of the branching point at ^{95}Zr .

Exceptions to this problem are the stable Eu isotopes, ^{151}Eu and ^{153}Eu , which do not have stable isobars and thus their ratio can be measured and used to constrain the neutron density and the temperature during the s -process in the parent stars of the grains via the branching points at ^{151}Sm and ^{152}Eu (Terada et al, 2006), and the Ba isotopes, which are not affected by isobaric interferences because their isobars, the isotopes of the noble gas Xe isotopes, are present in very low amounts in the grains and are difficult to ionize and extract from the stardust (see specific discussion below in this section.) The Ba isotopic ratios, in particular the $^{134}\text{Ba}/^{136}\text{Ba}$ and the $^{137}\text{Ba}/^{136}\text{Ba}$ ratios, can be affected by branching points at the Cs isotopes (see below and Prombo et al, 1993; Marhas et al, 2007).

The application of RIMS (Chapter 10, Section 2) to the analysis of heavy elements in SiC grains has allowed to overcome the problem of isobaric interferences, at the same time providing an experimental method of very high sensitivity, which allows the measurements of trace elements in single stardust grains (Savina et al, 2003b). Since RIMS can select which element is ionized and extracted from the grains, mass interferences are automatically avoided. The Chicago-Argonne RIMS for Mass Analysis CHARISMA has been applied to date to the measurement of Zr (Nicolussi et al, 1997), Mo (Nicolussi et al, 1998a), Sr (Nicolussi et al, 1998b), Ba (Savina et al, 2003a) and Ru (Savina et al, 2004) in large single SiC grains (average size $3\text{ }\mu\text{m}$), providing high-precision constraints on the operation of the s -process branching points that may affect the isotopic composition of these elements. A detailed comparison between data and models (Lugaro et al, 2003a) shows that AGB stellar models of low mass and metallicity roughly solar, where the $^{13}\text{C}(\alpha, n)^{16}\text{O}$ reaction is the main neutron source and the $^{22}\text{Ne}(\alpha, n)^{25}\text{Mg}$ is only marginally activated, provide the best match to all measured isotopic ratios affected by branching points. This result is in agreement with the constraints mentioned above provided

by the isotopic data for Ba (Marhas et al, 2007) and Eu (Terada et al, 2006) obtained via high-resolution SIMS.

For example, the $^{96}\text{Zr}/^{94}\text{Zr}$ ratio is observed in all measured single SiC to be lower than solar by at least 50%. Low-mass AGB models can reproduce this constraint due to the low neutron density associated with the main ^{13}C neutron source, in which conditions ^{96}Zr behaves like a typical r -only nucleus and is destroyed during the neutron flux. Massive AGB stars ($> 4.5 M_{\odot}$), on the other hand, experience high neutron densities and produce $^{96}\text{Zr}/^{94}\text{Zr}$ ratios higher than solar. In more detail, the $^{96}\text{Zr}/^{94}\text{Zr}$ ratio at the stellar surface of low-mass AGB stellar models reaches a minimum of $\simeq 90\%$ lower than solar after roughly ten 3^{rd} dredge-up episodes, and then may increase again, due to the marginal activation of the ^{22}Ne neutron source in the latest thermal pulses. This predicted range allows to cover most of the $^{96}\text{Zr}/^{94}\text{Zr}$ of single SiC grains (see Fig. 5 of Lugaro et al, 2003a).

Another interesting example is the $^{134}\text{Ba}/^{136}\text{Ba}$ ratio, where both isotopes are s -only nuclei. During the low-neutron density flux provided by the ^{13}C neutron source the branching point at ^{134}Cs is closed and the $^{134}\text{Ba}/^{136}\text{Ba}$ ratio at the stellar surface reaches up to $\simeq 20\%$ higher than the solar ratio after roughly ten 3^{rd} dredge-up episodes. This value is too high to match the composition of single SiC grains. However, during the marginal activation of the ^{22}Ne in the later thermal pulses, the branching point at ^{134}Cs is activated, ^{134}Ba is skipped during the s -process flux and the $^{134}\text{Ba}/^{136}\text{Ba}$ ratio at the stellar surface is lowered down to the observed values roughly 10% higher than the solar value (see Fig. 14 of Lugaro et al, 2003a).

The $^{137}\text{Ba}/^{136}\text{Ba}$ ratio is another indicator of the neutron density because the activation of the chain of branching points along the Cs isotopes can produce ^{137}Cs , which decays into ^{137}Ba with a half life of 30 yr. Grain data do not show any contribution of ^{137}Cs to ^{137}Ba , indicating that the Cs branching points beyond ^{134}Cs are not activated in the parent stars of the grains (see Fig. 14 of Lugaro et al, 2003a). This, again, excludes massive AGB stars, with an important neutron contribution from the ^{22}Ne neutron source, as the parent stars of the grains.

Another example of the signature of the s -process in meteorites is represented by very small variations, of the order of parts per ten thousand, observed in the osmium isotopic ratios of primitive chondritic meteorites. This fascinating anomaly looks like a *mirror* s -process signature, meaning that they show exactly the opposite behaviour expected if the meteorite had a component carrying an s -process signature. They are thus interpreted as a sign of incomplete assimilation of stardust SiC grains within the meteorite (Brandon et al, 2005). The branching points at ^{185}W and ^{186}Re make the $^{186}\text{Os}/^{188}\text{Os}$ ratio a indicator of the neutron density for the s -process and the value for this ratio observed in chondrites suggest a low neutron density of $N_n = 3 \times 10^8 \text{ n/cm}^3$ (Humayun and Brandon, 2007), in agreement with other evidence discussed above.

Differently from refractory elements, the noble gases He, Ne, Ar, Kr, and Xe are not chemically reactive and can condense from gas into solid only at much lower temperatures than those around AGB stars. Still, they are found in SiC, even if in extremely low quantities. Their atoms could have been ionized by the energy

carried by the stellar winds during the AGB and post-AGB phase. These ions were then chemically reactive enough to be *implanted* into already formed dust grains.

It has been possible to extract noble gases from meteoritic samples by RIMS (see Chapter 11), laser gas extraction (Nichols et al, 1991) and stepped-heating combustion of the sample to high temperatures, up to 2,000 degrees (Lewis et al, 1994). In particular, for the heavy nobler gases Kr and Xe, since their abundances are very low in stardust and the stepped-heating experimental method does not provide high extraction efficiency, it has been possible to extract their ions only from a large amount of meteoritic residual material. The derived Kr and Xe isotopic data is thus the average over a large number - millions - of grains. Differential information as function of the grain sizes can still be obtained by preparing the meteoritical residual in a way that selects the size of the grains to be found in it.

The composition of Xe in SiC corresponds to the famous Xe-S component, one of the first signature of the presence of pure stellar material in primitives meteorites (see Chapter 2, Section 2.5), thus named because of its obvious *s*-process signature: excesses in the *s*-only isotopes $^{128,130}\text{Xe}$ and deficits in the *r*-only and *p*-only isotopes $^{124,126,136}\text{Xe}$ (all with respect to the solar composition). The $^{134}\text{Xe}/^{130}\text{Xe}$ ratio may be affected by the operation of the branching point at ^{133}Xe during the *s*-process. This isotopic ratio in stardust SiC is very close to zero, indicating that the Xe trapped in SiC grains did not experience *s*-process with high neutron density (Pignatari et al, 2004). This again allows the mass and metallicity of the parent stars of the grains to be constrained to low-mass AGB stars of roughly solar metallicity, in agreement with the conclusions drawn from the composition of the refractory elements.

The situation regarding the Kr isotopic ratios measured in SiC grains is much more complex. There are two branching points affecting the Kr isotopic composition: ^{79}Se and ^{85}Kr , changing the abundances of ^{80}Kr and ^{86}Kr , respectively, and both of them are tricky to model (see description in Appendix B). Moreover, the Kr atoms in stardust SiC appear to be consistent with implantation models of this gas into the grains only if these models consider two different components of implanted Kr (Verchovsky et al, 2004). One component was ionized and implanted in SiC at low energy, corresponding to a velocity of $5\text{--}30\text{ km s}^{-1}$, typical of AGB stellar winds, the other component was ionized and implanted at high energy, corresponding to a velocity of a few thousands km/s, typical of the winds driven from the central star during the planetary nebular phase. In the second situation, which is the case also for all the He, Ar, and Ne atoms found in SiC, the isotopic composition of the noble gases indicate that they must have come directly from the deep He-rich and *s*-process rich layers of the star, with very small dilution with the envelope material of initial solar composition. This is consistent with the fact that at this point in time the envelope is very thin as most of the initial envelope material has been peeled away by the stellar winds.

While the Kr AGB component is observed to be prominent in the small grains (of average size $0.4\text{ }\mu\text{m}$) and shows low $^{86}\text{Kr}/^{82}\text{Kr}$ and high $^{80}\text{Kr}/^{82}\text{Kr}$ ratios, in agreement again with low neutron density *s*-process AGB models, the Kr planetary-nebula component is observed to be prominent in the largest grains (average size 3

μm) and shows high $^{86}\text{Kr}/^{82}\text{Kr}$ and low $^{80}\text{Kr}/^{82}\text{Kr}$ ratios, as expected instead in pure He-rich intershell material due to the higher neutron density s -process occurring in the final AGB thermal pulses (Pignatari et al, 2006). Actually, it is difficult to reproduce the $^{86}\text{Kr}/^{82}\text{Kr}$ up to twice the solar value observed in the largest grains even using the final pure s -process intershell composition of low-mass and solar metallicity AGB stellar models. This high $^{86}\text{Kr}/^{82}\text{Kr}$ ratios may be the signature of high-neutron density s -process nucleosynthesis occurring in *late* and *very late* thermal pulses during the post-AGB phase (see, e.g., Herwig et al, 1999), rather than during the AGB phase. Detailed s -process models are currently missing for this phase of stellar evolution.

In summary, the detailed information provided by stardust data on the isotopic ratios affected by branching points at radioactive nuclei on the s -process path has allowed us to pinpoint the characteristics of the neutron flux that the parent stars of stardust SiC grains must have experienced. The vast amount of information on the composition of light and heavy elements in SiC grains has allowed us to infer with a high degree of confidence that the vast majority of these grains came from C-rich AGB stars, i.e., C(N) stars, which have C>O in their envelope, the condition for SiC grain formation, of low mass and metallicity close to solar. In turn, the stardust data has been used to refine our theoretical ideas of the s -process in these stars confirming that ^{13}C nuclei must be the main neutron source, while the ^{22}Ne neutron source is only marginally active.

3.6 Nucleosynthesis of Long-lived Isotopes in AGB Stars

3.6.1 ^{26}Al

The famous long-lived radioactive nucleus ^{26}Al (with half life of 0.7 Myr), of interest from the point of view of γ -ray observations, meteoritic stellar grains, and the composition of the early solar system, can be produced in AGB stars via proton captures on ^{25}Mg , i.e., the $^{25}\text{Mg}(p, \gamma)^{26}\text{Al}$ reaction, when the temperature is above $\simeq 60$ MK (Mowlavi and Meynet, 2000; van Raai et al, 2008b). As detailed in Section 3.4.1, proton captures occur in AGB stars between thermal pulses in two different locations: (1) in the H-burning shell on top of the He-rich intershell, and (2) at the base of the convective envelope in massive AGB stars, above $\simeq 4 M_{\odot}$ (in the process known as Hot Bottom Burning, HBB, Section 3.4.1).

In setting (1), the intershell material is progressively enriched in ^{26}Al as proton captures in the H-burning shell convert 80% of ^{25}Mg into ^{26}Al . The efficiency of this conversion is determined by the fraction of 20% of $^{25}\text{Mg}+p$ reactions producing the isomeric, rather than the ground, state of ^{26}Al , which quickly decays into ^{26}Mg with a half life of $\simeq 6$ s. Most of the intershell ^{26}Al abundance is destroyed by neutron captures before having the chance of being dredged-up to the stellar surface via the 3^{rd} dredge-up. This is because the neutron-capture cross sections of ^{26}Al , in

particular the (n, p) and (n, α) channels, are very efficient: $\sigma \simeq 250$ and 180 mbarn, respectively.

More specifically, already during the interpulse period some ^{26}Al is destroyed by neutron captures. This is because in the bottom layers of the ashes of H burning the temperature reaches 90 MK, high enough for the $^{13}\text{C}(\alpha, n)^{16}\text{O}$ reaction to occur using as fuel the ^{13}C nuclei in ashes of H burning produced by CNO cycling. Then, neutron captures in the following thermal pulse destroy most of the ^{26}Al that was left over in the H-burning ashes. First, the ^{13}C nuclei that had survived in the top layers of the H-burning ashes are engulfed in the convective pulse, where the temperature quickly reaches 200 MK and the $^{13}\text{C}(\alpha, n)^{16}\text{O}$ reaction is very efficiently activated. Second, the neutrons that may be released by the $^{22}\text{Ne}(\alpha, n)^{25}\text{Mg}$ reaction later on in the convective pulse, when the temperature is higher than roughly 250 MK, contribute to further destruction of ^{26}Al . In this phase ^{26}Al can be completely destroyed, depending on the temperature reached at the base of the convective pulse, which controls the efficiency of the $^{22}\text{Ne}(\alpha, n)^{25}\text{Mg}$ reaction. If the temperature reaches up to 300 MK, the ^{26}Al abundance is decreased by two orders of magnitude in the He-rich intershell at the end of the thermal pulse.

When the 3rd dredge-up occurs after the thermal pulse is extinguished, only a small mass of ^{26}Al is carried from the intershell to the stellar surface, of the order of $10^{-8} M_{\odot}$, mostly coming from a tiny region (roughly $10^{-4} M_{\odot}$) at the top of the intershell, which was not ingested in the convective pulse and thus did not experience the availability of free neutrons. This small abundance of ^{26}Al carried into the envelope translates into a small total contribution of the AGB winds to the abundance of ^{26}Al in the interstellar medium (also defined as *yield*) of $10^{-7} M_{\odot}$, for AGB stars of masses between $1 M_{\odot}$ and $4 M_{\odot}$, depending on the metallicity (upper panel of Fig. 3.12), though allowing a noticeable increase in the $^{26}\text{Al}/^{27}\text{Al}$ ratio at the stellar surface, up to a typical value of 2×10^{-3} (lower panel of Fig. 3.12).

The situation is very different for AGB stars of masses higher than approximately $4 M_{\odot}$. Proton captures occurring in setting (2), i.e., HBB at the base of the convective envelope, combined with the 3rd dredged-up of ^{25}Mg produced from efficient activation of the $^{22}\text{Ne}(\alpha, n)^{25}\text{Mg}$ reaction in the thermal pulse, produce large amounts of ^{26}Al . These are directly mixed to the stellar surface via the envelope convection resulting in yields up to $10^{-4} M_{\odot}$, and $^{26}\text{Al}/^{27}\text{Al}$ ratios up to 0.5 (Fig. 3.12). During HBB the main channel for ^{26}Al destruction is proton captures on ^{26}Al itself, i.e., $^{26}\text{Al}(p, \gamma)^{27}\text{Si}$ reactions. Also in Super-AGB stars HBB produces large quantities of ^{26}Al (Siess and Arnould, 2008).

Figure 3.12 shows the yields of ^{26}Al and their ratio with the yield of ^{27}Al for a variety of AGB stars and Super-AGB of different masses and metallicities. The plot shows how the efficiency of ^{26}Al production increases with stellar mass and with decreasing metallicity of the stars. This is because the efficiency of the HBB depends on the temperature at the base of the convective envelope, which is higher for higher masses and lower metallicities. For example, a $3.5 M_{\odot}$ star of metallicity 200 times lower than solar ejects the same amount of ^{26}Al than a $6.5 M_{\odot}$ star at solar metallicity. The reason is that the overall temperature is controlled by the mass of the CO core, which scales directly with the initial mass and inversely with the initial

metallicity (see Section 3.4.1). In addition, the lower opacity in lower metallicity stars keeps the structure more compact and hence hotter.

In the models of Super-AGB presented in Fig. 3.12 the 3rd dredge-up is found to be negligible and HBB produces ^{26}Al via proton captures on the ^{25}Mg initially present in the envelope, without the contribution of ^{25}Mg from the intershell. Still, these stars produce a large amount of ^{26}Al since there is a large initial amount of ^{25}Mg in the envelope due to the large envelope mass. The lower Super-AGB ^{26}Al yield at metallicity solar/200 is due to very high HBB temperatures, at which the rate of the ^{26}Al destruction reaction $^{26}\text{Al}(p, \gamma)^{27}\text{Si}$ is significantly enhanced.

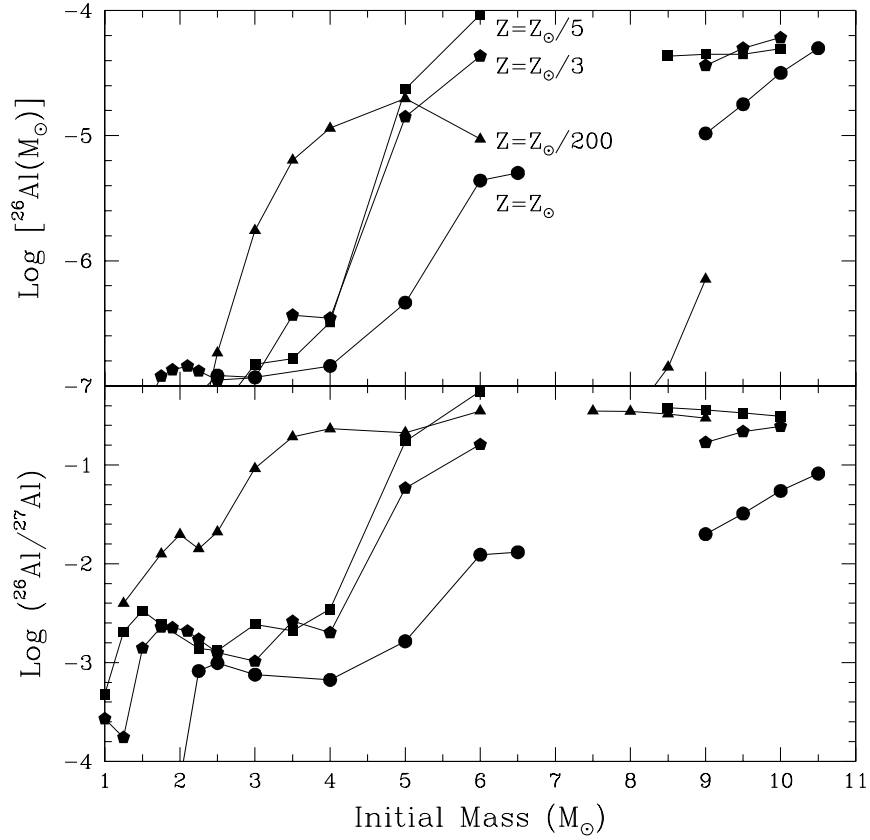


Fig. 3.12 The yields of ^{26}Al (top panel) for stellar models of different masses and metallicities (Z) from Karakas and Lattanzio (2007) for AGB stars of masses up to $6 M_{\odot}$, and from Siess and Arnould (2008) for the more massive Super-AGB stars. Yields are defined as the total mass of ^{26}Al (in M_{\odot}) lost in the wind during the whole evolution of the star (calculated as the average of the time-dependent envelope composition weighed on the mass lost at each time). The ratios of the yield of ^{26}Al to the yield of ^{27}Al are also shown in the bottom panel.

The yields predicted for the ^{26}Al from AGB stars presented in Fig. 3.12 are quite uncertain since there are several stellar and nuclear uncertainties. First, there are uncertainties related to the modelling of HBB. In fact, the temperature reached at the base of the convective envelope, which governs the efficiency of the $^{25}\text{Mg}(p, \gamma)^{26}\text{Al}$ reaction, depends on the modeling of the temperature gradient within the convectively unstable region. Hence, different treatments of the convective layers may lead to significantly different efficiencies of the HBB. Second, the uncertainty in the efficiency of the 3^{rd} dredge-up already discussed in Section 3.4.1 also affects the ^{26}Al yields: in the low-mass models it affects the dredge-up of ^{26}Al itself, in the massive models it affects the dredge-up of ^{25}Mg , which is then converted into ^{26}Al via HBB. Third, the mass-loss rate is another major uncertain parameter in the modelling of AGB stars. The mass-loss rate determines the stellar lifetime and thus the time available to produce ^{26}Al and the final ^{26}Al yield.

Another model uncertainty is related to the possible occurrence of extra mixing at the base of the convective envelope in the low-mass AGB models that do not experience HBB. Such extra mixing in AGB stars would be qualitatively similar to the extra mixing in red giant stars described in Section 3.3.2. In the hypothesis of extra mixing, material travels from the base of the convective envelope inside the radiative region close to the H-burning shell, suffers proton captures, and is taken back up into the convective envelope. If the mixed material dips into the H-burning shell, down to temperatures higher than $\simeq 50$ MK, then this mechanism could produce ^{26}Al and contribute to some amount of this nucleus in the low-mass models (Nollett et al, 2003). Unfortunately, from a theoretical point of view, there is no agreement on which mechanism drives the extra mixing and on the features of the mixing. Some constraints on it, however, can be derived from the composition of MS, S, SC, and C stars as well as meteoritic stellar grains, as will be discussed in detail in Section 3.6.2.

As for nuclear uncertainties, the rate of the $^{26}\text{Al}(p, \gamma)^{27}\text{Si}$ reaction is uncertain by three orders of magnitude in the temperature range of interest for AGB stars (Iliadis et al, 2001), with the consequence that ^{26}Al yields from AGB stars suffer from uncertainties of up to two orders of magnitude (Izzard et al, 2007; van Raai et al, 2008b). New experiments and approaches to estimate this rate are needed to get a more precise determination of the production of ^{26}Al in AGB stars.

In spite of all these important uncertainties, current models do indicate that at least some AGB models produce a significant amount of ^{26}Al . These models cover a small range of stellar masses, only those suffering HBB on the AGB phase. When the yields presented in Fig. 3.12 are averaged over a Salpeter initial stellar mass function, the result is that AGB stars globally do not provide an important contribution to the present abundance of ^{26}Al in the Galaxy. This contribution sums up to only 0.24% of the contribution from massive star winds and core-collapse supernovae (Limongi and Chieffi, 2006; Lugaro and Karakas, 2008). Adding up the contribution of Super-AGB stars only marginally increases the contribution of AGB stars to Galactic ^{26}Al to 0.85% of the contribution coming from the more massive stars (see also Siess and Arnould, 2008).

3.6.2 Evidence of ^{26}Al in AGB Stars

It may be possible to determine the abundance of ^{26}Al in AGB stars using molecular lines of Al-bearing molecules. This was carried out by (Guelin et al, 1995) for the nearest carbon star, CW Leo, using rotational lines of AlF and AlCl molecules with different Al isotopic composition. One observed line was tentatively attributed to ^{26}AlF , and from its observed strength an upper limit of 0.04 for the $^{26}\text{Al}/^{27}\text{Al}$ ratio was inferred. No $^{26}\text{AlCl}$ lines were detected, which led to an upper limit of 0.1. These values cannot be reached by solar metallicity AGB models (Fig. 3.12), however, this detection has not been confirmed so it is doubtful if it can represent a valid model constraint.

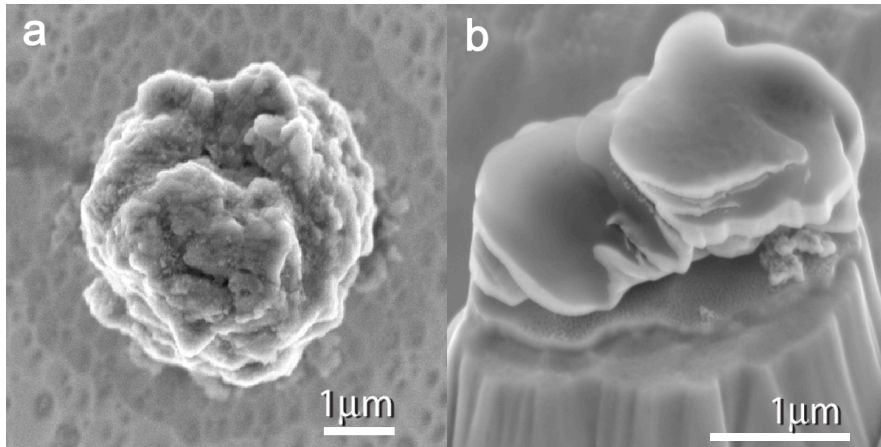


Fig. 3.13 Scanning electron microscope images of dust grains from AGB stars. (a) 4- μm -sized silicon carbide (SiC) grain; ubiquitous excesses in ^{26}Mg in such grains indicate prior presence of ^{26}Al . (b) 2- μm -sized hibonite ($\text{CaAl}_{12}\text{O}_{19}$) grain KH15 (Nittler et al, 2008). The grain is sitting on a gold pedestal created by ion-probe sputtering during isotopic analysis. Excesses of ^{26}Mg and ^{41}K indicate that the grain originally condensed with live ^{26}Al and ^{41}Ca .

The main observational evidence of ^{26}Al in AGB stars comes, instead, from stardust (see Fig. 3.13). Aluminium is one of the main component of most oxide stardust grains recovered to date and the initial amount of ^{26}Al present in each grain can be derived from excesses in its daughter nucleus ^{26}Mg . Magnesium is not a main component in corundum (Al_2O_3) and hibonite ($\text{CaAl}_{12}\text{O}_{19}$) grains, hence, in these cases, ^{26}Mg excesses are all attributed to ^{26}Al decay. In the case of spinel (MgAl_2O_4) grains, instead, Mg is a main component of the mineral and thus the contribution of ^{26}Al to ^{26}Mg needs to be more carefully evaluated by weighing the contribution of the two components. Specifically, there are two atoms of Al per each atom of Mg in spinel, which corresponds to a roughly 25 times higher ratio than in the average solar system material.

The $^{26}\text{Al}/^{27}\text{Al}$ ratios are observed to be different in the different populations of oxide and silicate grains (see, e.g., Fig. 8 of Nittler et al, 1997). Population I grains cover a wide range of ^{26}Al initial abundance, from no detection to $^{26}\text{Al}/^{27}\text{Al} \simeq 0.02$. The presence of ^{26}Al is used to discriminate Population I oxide grains coming from red giant or from AGB stars, since ^{26}Al is expected to be present only in the winds of AGB stars. The $^{26}\text{Al}/^{27}\text{Al}$ ratios of Population II grains lie at the upper end of the range covered by Population I grains, and reach up to $\simeq 0.1$ (see also Fig. 6 of Zinner et al, 2007). This is qualitatively consistent with the strong ^{18}O deficits observed in the Population II grains, since both signatures are produced by H burning. The mysterious Population III show low or no ^{26}Al , which may indicate that these grains did not come from AGB stars. Finally, Population IV grains from supernovae show $^{26}\text{Al}/^{27}\text{Al}$ ratios between 0.001 and 0.01 (see Chapter 4).

The $^{26}\text{Al}/^{27}\text{Al}$ ratios together with the $^{18}\text{O}/^{16}\text{O}$ ratios in Population I and II oxide and silicate grains provide an interesting puzzle to AGB modellers. Low-mass AGB models do not produce $^{26}\text{Al}/^{27}\text{Al}$ ratios high enough and $^{18}\text{O}/^{16}\text{O}$ ratios low enough to match the observations. Massive AGB models can produce $^{26}\text{Al}/^{27}\text{Al}$ ratios high enough via HBB, however, in this case the $^{18}\text{O}/^{16}\text{O}$ ratio is too low ($\sim 10^{-6}$) to match the observations (see Section 3.2.1). Grains with $^{18}\text{O}/^{16}\text{O} < 10^{-4}$ may have been polluted by solar material during the laboratory analysis, which would have shifted the $^{18}\text{O}/^{16}\text{O}$ ratio to higher values with respect to the true ratio of the grain. This argument was invoked to attribute a massive AGB stars origin to a peculiar Population II spinel grain, named OC2 (Lugaro et al, 2007). However, also the $^{17}\text{O}/^{16}\text{O}$ ratio presents a problem for this and similar grains because at the temperature of HBB this ratio is always much higher than observed (Boothroyd et al, 1995; Lugaro et al, 2007; Iliadis et al, 2008).

The extra-mixing phenomena mentioned in Secs. 3.3.2 and 3.6.1 have been hypothesized to operate in low-mass AGB stars below the base of the formal convective envelope to explain the composition of Population I and II grains with $^{26}\text{Al}/^{27}\text{Al}$ ratios greater than $\simeq 10^{-3}$. This idea has been investigated in detail by Nollett et al (2003) using a parametric model where the temperature (T_p), determined by the depth at which material is carried, and the mass circulation rate (M_{circ}) in the radiative region between the base of the convective envelope and the H-burning shell are taken as two free and independent parameters. This model was originally proposed to explain observations of AGB stars and grains showing deficits in ^{18}O (Wasserburg et al, 1995).

In the case of SiC grains, Al is present in the grains as a trace element in relatively large abundance, while Mg is almost absent. Again, this means that ^{26}Mg excesses represent the abundance of ^{26}Al at the time when the grains formed. Mainstream SiC grains from AGB stars show $^{26}\text{Al}/^{27}\text{Al}$ ratios between 10^{-4} and $\simeq 2 \times 10^{-3}$. Models of C-rich AGB stars, i.e., the low-mass models in the lower panel of Fig. 3.12, which do not suffer HBB and hence can reach $\text{C}/\text{O} > 1$ in their envelopes, match the observed upper value but do not cover the observed range down to the lower values (Zinner et al, 2007; van Raai et al, 2008b). It is difficult to interpret the lowest values as pollution of solar material as in this case one would expect a trend of decreasing $^{26}\text{Al}/^{27}\text{Al}$ ratios with the total Al content in the grains, which is not ob-

served. As discussed in Section 3.6.1, the main problem modelers have to consider in this context is the large uncertainty in the $^{26}\text{Al}+p$ reaction rate (van Raai et al, 2008b). The rate uncertainty results in an uncertainty of one order of magnitude in the $^{26}\text{Al}/^{27}\text{Al}$ ratios predicted for C-rich AGB stars. If the current upper limit of the rate is employed in the models, then only the lower values observed in SiC can be matched and we may need to invoke extra-mixing phenomena also to explain the Al composition of SiC grains. On the other hand, if the lower or recommended values of the rates are used, then only the higher values observed in SiC can be matched.

In conclusion, observational constraints of ^{26}Al in AGB stars provide the potential to investigate some of the most uncertain input physics in the modelling of AGB nucleosynthesis: mixing phenomena and reaction rates.

3.6.3 ^{60}Fe

The other famous long-lived radioactive nucleus ^{60}Fe (with a recently revised half life of 2.6 My, Rugel et al, 2009), of interest from the point of view of γ -ray observations, meteoritic stellar grains, and the composition of the early solar system, can be produced in AGB stars (Wasserburg et al, 2006; Lugaro and Karakas, 2008) via the neutron-capture chain $^{58}\text{Fe}(n, \gamma)^{59}\text{Fe}(n, \gamma)^{60}\text{Fe}$, where ^{59}Fe is a branching point, and destroyed via the $^{60}\text{Fe}(n, \gamma)^{61}\text{Fe}$ reaction, whose rate has been measured experimentally by (Uberseder et al, 2009). This is the same chain of reactions responsible for the production of this nucleus in massive stars (see Chapter 4, Section 3.1.2). Given that ^{59}Fe is an unstable nucleus with a relatively short half life of 44 days and with a neutron-capture cross section $\sigma \simeq 23$ mbarn (Rauscher and Thielemann, 2000), neutron densities of at least 10^{10} n/cm³ are needed for this branching point to open at a level of 20%, allowing production of the long-living ^{60}Fe . If the neutron density is higher than 10^{12} n/cm³, then 100% of the neutron-capture flux goes through ^{60}Fe .

From the description of the neutron sources in AGB stars (Section 3.5.2), it is clear that ^{60}Fe can only be produced in the convective thermal pulses, where the neutron burst released by the ^{22}Ne neutron source can reach the high neutron density required to open the branching point at ^{59}Fe . Hence, the production of ^{60}Fe in AGB stars is almost completely determined by the activation of the ^{22}Ne neutron source. The ^{13}C neutron source may instead destroy some ^{60}Fe in the intershell (Wasserburg et al, 2006).

The AGB yields of ^{60}Fe , and their ratios with the yields of ^{56}Fe , are shown in Fig. 3.14. As the temperature at the base of the convective thermal pulses increases with increasing the stellar mass and decreasing the metallicity, the amount of ^{60}Fe delivered to the interstellar medium increases, reaching up to $10^{-5} M_{\odot}$, a value comparable to that delivered by a supernova of $\simeq 20 M_{\odot}$ (Limongi and Chieffi, 2006). Ratios of the ^{60}Fe and ^{56}Fe abundances at the end of the AGB phase from the AGB neutron-capture models of (Wasserburg et al, 2006) also plotted in Fig. 3.14.

As for ^{26}Al , also in the case of ^{60}Fe stellar and nuclear uncertainties affect the results presented in Fig. 3.14 (and different choice in the model inputs are responsi-

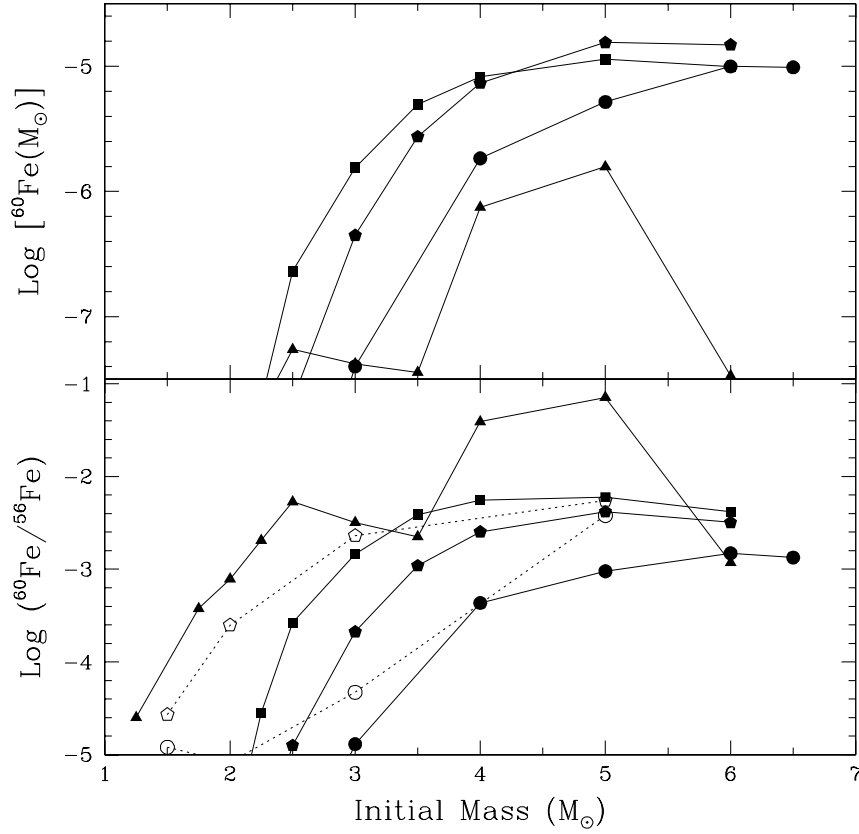


Fig. 3.14 The yields of ^{60}Fe (top panel) from Karakas and Lattanzio (2007) (see caption of Fig. 3.12 for definition of a yield) and the ratio of the yield of ^{60}Fe to the yield of ^{56}Fe (bottom panel) for stellar models of different masses and metallicities (full symbols from Karakas and Lattanzio, 2007). The symbols representing the different metallicities are the same as in Fig. 3.12. For comparison, the ratios of the abundances of ^{60}Fe and ^{56}Fe at the end of the AGB evolution computed by Wasserburg et al (2006) are also shown as open symbols.

ble for variations in the results obtained by different authors). First, the overall mass carried to the envelope via the 3rd dredge-up is essential to the determination of the envelope ^{60}Fe abundance in AGB stars. This is because ^{60}Fe is made only via neutron captures in the He-rich intershell and needs to be mixed into the envelope in order to show up at the stellar surface and to be carried to the interstellar medium by the winds. Hence, the ^{60}Fe yield is directly related to the efficiency of the 3rd dredge-up. For example, models experiencing little or no 3rd dredge-up produce a null ^{60}Fe yield. This important point applies to all long-living radioactive nuclei produced in AGB stars, except for the case of ^{26}Al , which is made via HBB directly

within the envelope. Second, the mass-loss rate affects the result as it determines the stellar lifetime and thus the number of thermal pulses and 3rd dredge-up episodes.

Nuclear physics inputs that contribute important uncertainties to the production of ^{60}Fe are the rate of the neutron source reaction $^{22}\text{Ne}(\alpha, n)^{25}\text{Mg}$, which determines how many neutrons are produced in the thermal pulses, and the neutron-capture cross section of ^{59}Fe , which is estimated only theoretically (Rauscher and Thielemann, 2000) as the short half life of this nucleus hampers experimental determinations.

3.6.4 ^{36}Cl and ^{41}Ca

Two more long-lived radioactive nuclei lighter than iron are of special interest because they are observed to be present in the early solar system and can be made by neutron captures in the intershell of AGB stars: ^{36}Cl (with half life of 0.3 Myr) and ^{41}Ca (with half life of 0.1 Myr). Differently from ^{60}Fe , production of these nuclei does not require the activation of branching points, since ^{36}Cl and ^{41}Ca are made by neutron captures on ^{35}Cl and ^{40}Ca , respectively, which are stable nuclei with relatively high solar abundances. Neutron captures also destroy ^{36}Cl and ^{41}Ca via different channels, the predominants being $^{41}\text{Ca}(n, \alpha)^{38}\text{Ar}$, with $\sigma \simeq 360$ mbarn and $^{36}\text{Cl}(n, p)^{36}\text{S}$, with $\sigma \simeq 118$ mbarn.

Neutrons coming from the ^{22}Ne neutron source are responsible for the production of ^{36}Cl and ^{41}Ca . As there are no branching points involved, this is not due to the high neutron density of this neutron flux, as it is for the production of ^{60}Fe , but to the fact that neutrons released by the ^{22}Ne in the thermal pulse affect the composition of the whole He-rich intershell material, where large initial quantities of the seed nuclei ^{35}Cl and ^{40}Ca are available. On the contrary, neutrons released by the ^{13}C neutron source affect a small fraction of the intershell material, being the ^{13}C pocket roughly $1/10^{\text{th}}$ to $1/20^{\text{th}}$ of the intershell (by mass) in the current models.

In general, to produce neutron-rich isotopes of elements lighter than iron by the *s*-process a small number of neutrons captured by seed nucleus are needed: only one in the cases of ^{36}Cl and ^{41}Ca . Hence, final abundances are determined to a higher level by the availability of seed nuclei, rather than that of free neutrons. For the light nuclei a production flux from the lighter to the heaviest elements does not occur (strictly speaking it is not correct to apply the *s*-process terminology in this case), instead, the nucleosynthetic process is very localized: neutron captures on the sulphur isotopes, for example, do not affect the abundances of the chlorine isotopes and so on. This is because neutron-capture cross section of nuclei lighter than iron are much smaller (by as much as 3 orders of magnitude) than those of typical nuclei heavier than iron. Hence, to produce nuclei heavier than iron by the *s*-process, instead, including the relatively large number of long-living radioactive nuclei lying on the *s*-process path discussed in Section 3.6.5, a production flux from the lighter to the heavier elements occurs, where many neutrons are captured by the

iron seeds and it is possible to reach up to the heaviest elements. Hence, the number of free neutrons plays a dominant role in this case.

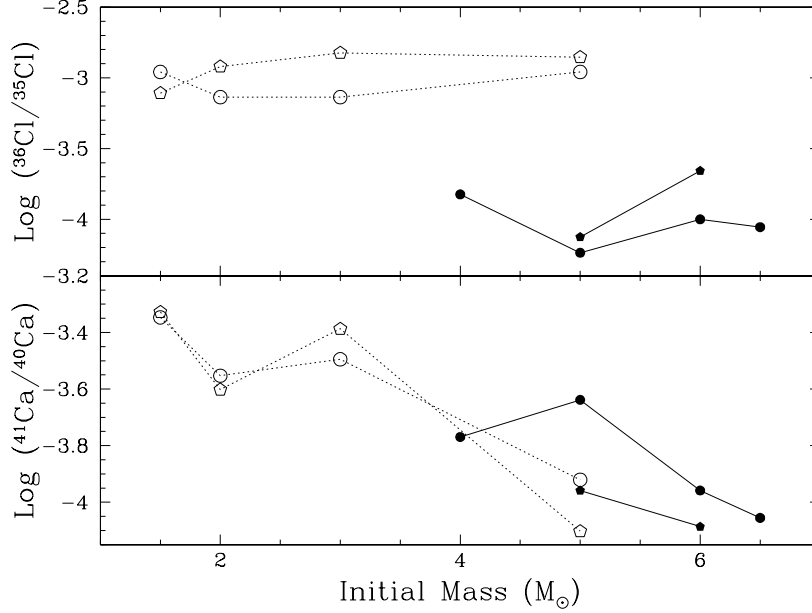


Fig. 3.15 ${}^{36}\text{Cl}/{}^{35}\text{Cl}$ and ${}^{41}\text{Ca}/{}^{40}\text{Ca}$ abundance ratios at the end of the AGB evolution computed by Wasserburg et al (2006) (open symbols) and by van Raai, Lugaro, & Karakas (unpublished results, full symbols). The symbols representing the different metallicities are the same as in Fig. 3.12.

The ${}^{36}\text{Cl}/{}^{35}\text{Cl}$ and ${}^{41}\text{Ca}/{}^{40}\text{Ca}$ abundance ratios at the end of the AGB evolution computed by Wasserburg et al (2006) and by van Raai, Lugaro, & Karakas (which are based on the same codes and stellar models of Karakas and Lattanzio, 2007) are plotted in Fig. 3.15. As in the case of ${}^{60}\text{Fe}$, the main model uncertainties affecting these results is the efficiency of the 3rd dredge-up, the mass-loss rate, and the rate of the ${}^{22}\text{Ne}(\alpha, n){}^{25}\text{Mg}$ reaction.

Moreover, while experimental estimates for the neutron-capture cross section of ${}^{36}\text{Cl}$ and ${}^{41}\text{Ca}$ are available (e.g., de Smet et al, 2006), a difficult problem is to provide a reliable set of values for the electron-capture rate of ${}^{41}\text{Ca}$, in particular as it is expected to vary significantly for different temperatures and densities relevant to stellar conditions (Chapter 9). As most electron captures in the ${}^{41}\text{Ca}$ atom occurs on electrons belonging to the electron shell closest to the nucleus (the K shell), when the temperature increases to 100 MK and all electrons have escaped the atom leaving the nucleus bare, the half life of ${}^{41}\text{Ca}$ increases by almost three orders of magnitude. However, if, still at a temperature of 100 MK, the density increases to

10^4 g/cm^3 , electrons are forced nearby ^{41}Ca nuclei and the half life decreases back to its terrestrial value. The only set of theoretical data for this reaction are those provided by Fuller et al (1982). Moreover, the temperature and density dependence of the electron-capture rate of ^{41}Ca has never been properly implemented in AGB stellar models, in particular it has not yet been solved coupled to convective motions, both in the thermal pulses and in the stellar envelope, where material is constantly carried from hotter denser regions to cooler less dense regions and viceversa. Given these considerations, we are far from an accurate determination of the abundance of ^{41}Ca made by AGB stars, although there is observational evidence of its presence in these stars from ^{41}K enrichments in hibonite stardust grains attributable to *in situ* decay of now-extinct ^{41}Ca (Nittler et al, 2008).

In summary, and in relevance to the early solar system composition of long-lived radioactive nuclei discussed in Chapter 6, AGB stars can produce some of the radioactive nuclei found to be present in the early solar system: ^{26}Al via hot bottom burning and ^{41}Ca and ^{60}Fe via neutron captures in the thermal pulse and the 3rd dredge-up. In certain mixing conditions the abundances of these nuclei can be produced by AGB stars in the same proportions observed in the early solar system (Wasserburg et al, 2006; Trigo-Rodriguez et al, 2009). On the other hand, ^{36}Cl cannot be produced in the observed amount. Uncertainties in the neutron-capture cross sections of ^{35}Cl and ^{36}Cl may play a role in this context.

Finally, a characteristic signature of the AGB stars inventory of long-living radioactive nuclei, is that, unlike supernovae (Chapter 4 and Chapter 5, Section 3), AGB stars cannot possibly produce ^{55}Mn , another nucleus of relevance to early solar system composition. This is because ^{55}Mn is a proton-rich nucleus, lying on the proton-rich side of the valley of β -stability, and thus it cannot be made by neutron captures.

3.6.5 Long-lived Radioactive Isotopes Heavier than Fe

3.6.5.1 Predicted Isotopic Abundances

The *s*-process in AGB stars produces significant abundances of six long-lived radioactive nuclei heavier than iron: ^{81}Kr , ^{93}Zr , ^{99}Tc , ^{107}Pd , ^{135}Cs , and ^{205}Pb . The survival of ^{135}Cs and ^{205}Pb in stellar environments is however very uncertain and can even be prevented because of the strong and uncertain temperature and density dependence of their half lives, decreasing by orders of magnitudes in stellar conditions and determined only theoretically (as in the case of ^{41}Ca . See detailed discussion by Mowlavi et al, 1998; Wasserburg et al, 2006, and also Appendix B). While ^{93}Zr , ^{99}Tc , ^{107}Pd , and ^{205}Pb are on the main *s*-process path and are produced by neutron captures on the stable isotopes ^{92}Zr , ^{98}Mo ¹⁴, ^{106}Pd , and ^{204}Pb , respectively, ^{81}Kr and ^{135}Cs are not on the main *s*-process path, but can be reached via the

¹⁴ followed by fast decay of ^{99}Mo , with a half life of 66 hours

activation of branching points at ^{79}Se and ^{80}Br , and ^{134}Cs , respectively (as described in Appendix B).

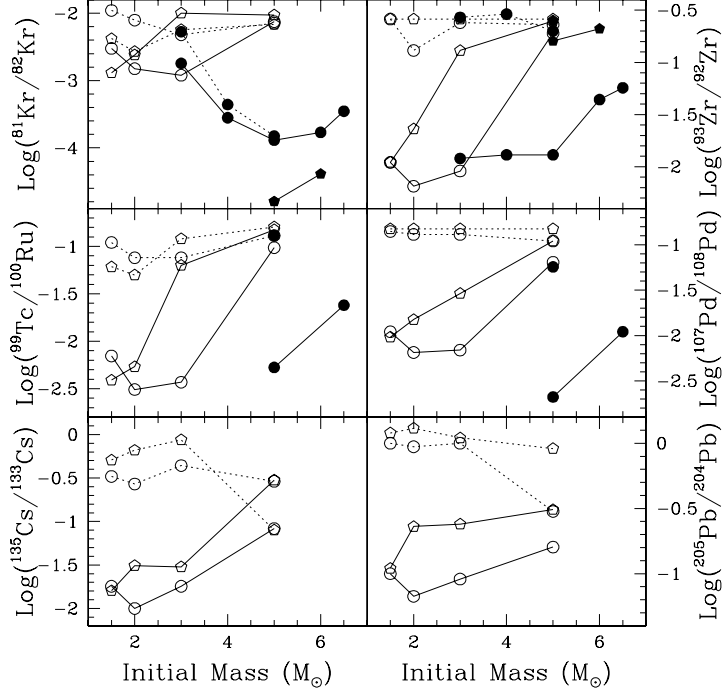


Fig. 3.16 Abundance ratios of long-lived radioactive nuclei heavier than iron, with respect to one of their nearest stable isotope, at the end of the AGB evolution computed by Wasserburg et al (2006) (open symbols) and by van Raai, Lugaro, & Karakas (unpublished results, full symbols). The symbols representing the different metallicities are the same as in Fig. 3.12. Symbols connected by the solid line represent models computed without the inclusion of the ^{13}C neutron source, symbols connected by the dotted lines represent models computed with the inclusion of the ^{13}C neutron source.

Figure 3.16 presents the abundance ratios of long-living radioactive isotopes heavier than iron produced during the s -process in AGB stars to one of their nearest stable isotopes calculated by Wasserburg et al (2006) and by van Raai et al. (unpublished results). For all ratios, except $^{81}\text{Kr}/^{82}\text{Kr}$, the inclusion of the ^{13}C neutron source for models of masses lower than $\simeq 3 - 4 M_{\odot}$, completely changes the results, since the ^{22}Ne source is not significantly activated in these low-mass stellar models. It also makes an important difference in the absolute abundance of the all isotopes involved, with very low production factors with respect to the initial value if the ^{13}C neutron source is not included (see Table 4 of Wasserburg et al, 2006). The case of $^{81}\text{Kr}/^{82}\text{Kr}$ is different in that it does not feel the inclusion of the ^{13}C neutron source

as much as the other ratios because, even for the low-mass stars, the marginal activation of the ^{22}Ne reaction in the latest thermal pulses affects the production of the s -process elements up to the first s -process peak, including Kr, and of ^{81}Kr in particular via the branching point at ^{79}Se .

For stellar models with initial masses higher than $\simeq 3 - 4 M_{\odot}$, depending on the metallicity, the ^{22}Ne neutron source is mainly responsible for the activation of the s -process and thus the production of the heavy long-lived isotopes. Hence, in these models, the inclusion of a ^{13}C neutron source typically does not make a significant difference in the final ratios, except in the case of $^{205}\text{Pb}/^{204}\text{Pb}$. This ratio is different in that it always feels the effect of the inclusion of the ^{13}C neutron source because production of the element Pb, corresponding to the third and last s -process peak, is possible only if very large neutron exposures are available ($\sim \text{mbarn}^{-1}$), which can only be produced by the ^{13}C neutron source.

It is interesting to discuss in detail the results for the $3 M_{\odot}$ stellar model of 1/3 solar metallicity, because this model represents an example of the transition between the two regimes of the s -process in AGB stars: when neutrons are provided by the ^{13}C or by the ^{22}Ne source. In this model the number of free neutrons produced by the ^{22}Ne source is higher than in the solar metallicity model of the same mass partly because the temperature in the thermal pulses is slightly higher, but mostly because there is a smaller number of nuclei present to capture neutrons. Hence, the neutron flux coming from the ^{22}Ne neutron source affects the production of the long-living isotopes up to ^{99}Tc , but not that of the long-living isotopes of higher masses: for ^{107}Pd , ^{133}Cs , and ^{205}Pb , ^{13}C is still the main neutron source.

In addition to the main effect due to the shift from the ^{13}C to the ^{22}Ne regime with changing the initial mass and metallicity of the star, smaller variations due to the marginal effect of the ^{22}Ne neutron source in the models of low-mass are always visible in the details of the production of the heavy long-living nuclei affected by the operation of the branching points activated in thermal pulses: ^{81}Kr and ^{135}Cs . For example, restricting our view to the solar metallicity models of mass lower than $4 M_{\odot}$ and computed with the inclusion of the ^{13}C neutron source, the $^{81}\text{Kr}/^{82}\text{Kr}$ ratio decreases with the stellar mass as ^{81}Kr is progressively skipped by the branching point at ^{79}Se at the higher neutron densities experienced by the higher mass models. The opposite happens for the $^{135}\text{Cs}/^{133}\text{Cs}$ ratio, which increases with the stellar mass as the branching point at ^{134}Cs becomes progressively more active.

When considering the effect of branching points on the production of heavy long-living radioactive nuclei by the s -process in AGB stars it is worth noting that ^{129}I and ^{182}Hf - two long-lived radioactive isotopes of special interest for the composition of the early solar system - are not significantly produced in AGB stars. Production of ^{129}I is not possible because the half life of ^{128}I is only 25 minutes (see Appendix B), while ^{182}Hf is produced, with $^{182}\text{Hf}/^{180}\text{Hf}$ up to $\simeq 0.02$ in the AGB envelope, via activation of the branching point at ^{181}Hf (Appendix B). This results in $^{182}\text{Hf}/^{180}\text{Hf}$ down to $\simeq 10^{-6}$ (after dilution of AGB ejecta in the interstellar medium Wasserburg et al, 1994), which is too low to explain the early solar system value of $\simeq 10^{-4}$ (see Chapter 6).

The main uncertainties affecting both sets of predictions shown in Fig. 3.16 are the detailed features of the proton diffusion leading to the production of the ^{13}C neutron source (see end of Section 3.4.1). Ratios that depend on the activation of the ^{22}Ne neutron source are also sensitive to the choice of the mass loss rate and of the $^{22}\text{Ne}(\alpha, n)^{25}\text{Mg}$ reaction rate. The treatment of branching points is also of importance in the determination of ^{81}Kr and ^{135}Cs . For example, in the case of $^{81}\text{Kr}/^{82}\text{Kr}$, the treatment of the temperature dependence of the decay rate of the branching point nucleus ^{79}Se is fundamental to the final result, as demonstrated by the fact that including the temperature dependence of these decay rate (as carried out by Wasserburg et al, 2006) produce a $^{81}\text{Kr}/^{82}\text{Kr}$ ratio two orders of magnitude larger than using the terrestrial value as constant (as done by van Raai, Lugaro, & Karakas, unpublished results).

In summary, due to the *s*-process, AGB stars are a rich source of radioactive elements heavier than Fe. The signature of this production is confirmed, e.g., by the presence of Tc observed in AGB star and in meteoritic stardust grains (as discussed further in the next section) and possibly in primitive meteoritic solar-system materials (as discussed in detail in Chapter 6).

3.6.5.2 Signatures in Stardust

The historical observation of Tc in late type giants (Section 3.5.2) was confirmed by the presence of ^{99}Tc in single stardust SiC grains at the time of their formation discovered via laboratory analysis of the Ru isotopic composition of these grains (Savina et al, 2004). Since both Tc and Ru are refractory elements, they were included in SiC grains as trace elements during grain formation. To match the observational stardust data both the contribution of ^{99}Ru and ^{99}Tc predicted by AGB stellar models to the total nuclear abundance at mass 99 must be considered. Radiogenic decay of ^{99}Tc occurs in the intershell in the absence of neutron fluxes, in the stellar envelope, and inside the grains.

On the other hand, there is no evidence for a contribution of ^{135}Cs to ^{135}Ba when comparing AGB model predictions to laboratory data of the $^{135}\text{Ba}/^{136}\text{Ba}$ ratio in single SiC grains (see Fig. 16 of Lugaro et al, 2003a). This is probably because Cs is not as refractory as Ba and thus was not included in the grains at the time of their formation.

References

- Abdurashitov JN, Bowles TJ, Cherry ML, Cleveland BT, Davis R, Elliott SR, Gavrin VN, Girin SV, Gorbachev VV, Ibragimova TV, Kalikhov AV, Khairnasov NG, Knodel TV, Lande K, Mirmov IN, Nico JS, Shikhin AA, Teasdale WA, Veretenkin EP, Vermul VM, Wark DL, Wildenhain PS, Wilkerson JF, Yants VE, Zatspein GT (1999) Measurement of the Solar Neutrino Capture Rate by SAGE and Implications for Neutrino Oscillations in Vacuum. *Physical Review Letters* 83:4686–4689, DOI 10.1103/PhysRevLett.83.4686, [arXiv:astro-ph/9907131](https://arxiv.org/abs/astro-ph/9907131)

- Abia C, Busso M, Gallino R, Domínguez I, Straniero O, Isern J (2001) The ^{85}Kr s-Process Branching and the Mass of Carbon Stars. *ApJ*559:1117–1134, DOI 10.1086/322383, *arXiv:astro-ph/0105486*
- Amari S, Gao X, Nittler LR, Zinner E, José J, Hernanz M, Lewis RS (2001a) Presolar Grains from Novae. *ApJ*551:1065–1072, DOI 10.1086/320235, *arXiv:astro-ph/0012465*
- Amari S, Nittler LR, Zinner E, Gallino R, Lugaro M, Lewis RS (2001b) Presolar SiC Grains of Type Y: Origin from Low-Metallicity Asymptotic Giant Branch Stars. *ApJ*546:248–266, DOI 10.1086/318230
- Amari S, Nittler LR, Zinner E, Lodders K, Lewis RS (2001c) Presolar SiC Grains of Type A and B: Their Isotopic Compositions and Stellar Origins. *ApJ*559:463–483, DOI 10.1086/322397
- Aoki W, Honda S, Beers TC, Sneden C (2003a) Measurement of the Europium Isotope Ratio for the Extremely Metal poor, r-Process-enhanced Star CS 31082-001. *ApJ*586:506–511, DOI 10.1086/367540, *arXiv:astro-ph/0211617*
- Aoki W, Ryan SG, Iwamoto N, Beers TC, Norris JE, Ando H, Kajino T, Mathews GJ, Fujimoto MY (2003b) Europium Isotope Ratios in s-Process Element-enhanced Metal-poor Stars: A New Probe of the ^{151}Sm Branching. *ApJ*592:L67–L70, DOI 10.1086/377681, *arXiv:astro-ph/0306544*
- Arlandini C, Käppeler F, Wisshak K, Gallino R, Lugaro M, Busso M, Straniero O (1999) Neutron Capture in Low-Mass Asymptotic Giant Branch Stars: Cross Sections and Abundance Signatures. *ApJ*525:886–900, DOI 10.1086/307938, *arXiv:astro-ph/9906266*
- Bahcall JN (2005) Solar Models and Solar Neutrinos. *Physica Scripta* Volume T 121:46–50, DOI 10.1088/0031-8949/2005/T121/006, *arXiv:hep-ph/0412068*
- Bahcall JN, Peña-Garay C (2004) Solar models and solar neutrino oscillations. *New Journal of Physics* 6:63–89, DOI 10.1088/1367-2630/6/1/063, *arXiv:hep-ph/0404061*
- Bahcall JN, Cleveland BT, Davis R Jr, Rowley JK (1985) Chlorine and gallium solar neutrino experiments. *ApJ*292:L79–L82, DOI 10.1086/184477
- Balachandran SC (2005) Anomalous Abundances in Red Giants: The Li-Rich Stars. In: T G Barnes III & F N Bash (ed) *Cosmic Abundances as Records of Stellar Evolution and Nucleosynthesis*, Astronomical Society of the Pacific Conference Series, vol 336, pp 113–+
- Bond H, Sion E, Murdin P (2000) CH Stars and Barium Stars. DOI 10.1888/0333750888/5413
- Boothroyd AI, Sackmann IJ, Wasserburg GJ (1995) Hot bottom burning in asymptotic giant branch stars and its effect on oxygen isotopic abundances. *ApJ*442:L21–L24, DOI 10.1086/187806
- BOREXINO Collaboration, Arpesella C, Bellini G, Benziger J, Bonetti S, Caccianiga B, Calaprice F, Dalnoki-Veress F, D’Angelo D, de Kerret H, Derbin A, Deutsch M, Etenko A, Fomenko K, Ford R, Franco D, Freudiger B, Galbiati C, Gazzana S, Giammarchi M, Goeger-Neff M, Goretti A, Grieb C, Hardy S, Heusser G, Ianni A, Ianni A, Joyce M, Korga G, Kryn D, Laubenstein M, Leung M, Litvinovich E, Lombardi P, Ludhova L, Machulin I, Manuzio G, Martemianov A, Masetti F, McCarty K, Meroni E, Miramonti L, Misiaszek M, Montanari D, Monzani ME, Muratova V, Niedermeier L, Oberauer L, Obolensky M, Ortica F, Pallavicini M, Papp L, Perasso L, Pocar A, Raghavan RS, Ranucci G, Razeto A, Sabelnikov A, Salvo C, Schönert S, Simgen H, Smirnov O, Skorokhvatov M, Sonnenschein A, Sotnikov A, Sukhotin S, Suvorov Y, Tarasenkova V, Tartaglia R, Testera G, Vignaud D, Vitale S, Vogelaar RB, von Feilitzsch F, Wojcik M, Zaimidoroga O, Zavatarelli S, Zuzel G (2008) First real time detection of ^7Be solar neutrinos by Borexino. *Physics Letters B* 658:101–108, DOI 10.1016/j.physletb.2007.09.054, 0708.2251
- Brandon AD, Humayun M, Puchtel IS, Leya I, Zolensky M (2005) Osmium Isotope Evidence for an s-Process Carrier in Primitive Chondrites. *Science* 309:1233–1236, DOI 10.1126/science.1115053
- Cameron AGW, Fowler WA (1971) Lithium and the s-process in Red-Giant Stars. *ApJ*164:111–114, DOI 10.1086/150821
- Castilho BV, Gregorio-Hetem J, Spite F, Barbuy B, Spite M (2000) Detailed analysis of a sample of Li-rich giants. *A&A*364:674–682
- Clayton DD (1968) *Principles of stellar evolution and nucleosynthesis*
- Clayton DD, Nittler LR (2004) Astrophysics with Presolar Stardust. *ARA&A*42:39–78, DOI 10.1146/annurev.astro.42.053102.134022

- Cleveland BT, Daily T, Davis RJ, Distel JR, Lande K, Lee CK, Wildenhain PS, Ullman J (1998) Measurement of the Solar Electron Neutrino Flux with the Homestake Chlorine Detector. *ApJ*496:505–526, DOI 10.1086/305343
- Cosner K, Iben I Jr, Truran JW (1980) The effects of unthermalized isomeric states and of a time-varying neutron flux on s-process branching ratios. *ApJ*238:L91–L96, DOI 10.1086/183265
- Cox JP, Giuli RT (1968) Principles of stellar structure
- Cristallo S, Straniero O, Gallino R, Piersanti L, Domínguez I, Lederer MT (2009) Evolution, Nucleosynthesis, and Yields of Low-Mass Asymptotic Giant Branch Stars at Different Metallicities. *ApJ*696:797–820, DOI 10.1088/0004-637X/696/1/797
- de Smet L, Wagemans C, J H, Vermote S, Van Gils J (2006) Experimental determination of the $^{41}\text{Ca}(n, \alpha)^{38}\text{Ar}$ reaction cross section. In: Ninth International Symposium on Nuclei in the Cosmos, Proceedings of Science, PoS(NIC-IX)085
- Denissenkov PA, Tout CA (2003) Partial mixing and formation of the ^{13}C pocket by internal gravity waves in asymptotic giant branch stars. *MNRAS*340:722–732, DOI 10.1046/j.1365-8711.2003.06284.x
- Despain KH (1980) A difficulty with Ne-22 as the neutron source for the solar system s-process. *ApJ*236:L165–L168, DOI 10.1086/183219
- Doherty CL, Lattanzio JC (2006) Evolution and nucleosynthesis in super-AGB stars. *Memorie della Societa Astronomica Italiana* 77:828–832
- Dorfi EA, Höfner S, Feuchtinger MU (2001) Pulsation and mass loss, pp 137–154
- Dupree AK (1986) Mass loss from cool stars. *ARA&A*24:377–420, DOI 10.1146/annurev.aa.24.090186.002113
- Ferrarotti AS, Gail HP (2002) Mineral formation in stellar winds. III. Dust formation in S stars. *A&A*382:256–281, DOI 10.1051/0004-6361:20011580
- Fleischer AJ, Gauger A, Sedlmayr E (1992) Circumstellar dust shells around long-period variables. I - Dynamical models of C-stars including dust formation, growth and evaporation. *A&A*266:321–339
- Frogel JA, Mould J, Blanco VM (1990) The asymptotic giant branch of Magellanic Cloud clusters. *ApJ*352:96–122, DOI 10.1086/168518
- Fuller GM, Fowler WA, Newman MJ (1982) Stellar weak interaction rates for intermediate mass nuclei. III - Rate tables for the free nucleons and nuclei with $A = 21$ to $A = 60$. *ApJS*48:279–319, DOI 10.1086/190779
- Gail HP, Sedlmayr E (1999) Mineral formation in stellar winds. I. Condensation sequence of silicate and iron grains in stationary oxygen rich outflows. *A&A*347:594–616
- Gallino R, Arlandini C, Busso M, Lugaro M, Travaglio C, Straniero O, Chieffi A, Limongi M (1998) Evolution and Nucleosynthesis in Low-Mass Asymptotic Giant Branch Stars. II. Neutron Capture and the s-Process. *ApJ*497:388–403, DOI 10.1086/305437
- García-Hernández DA, García-Lario P, Plez B, D’Antona F, Manchado A, Trigo-Rodríguez JM (2006) Rubidium-Rich Asymptotic Giant Branch Stars. *Science* 314:1751–1754, DOI 10.1126/science.1133706, [arXiv:astro-ph/0611319](https://arxiv.org/abs/astro-ph/0611319)
- García-Hernández DA, García-Lario P, Plez B, Manchado A, D’Antona F, Lub J, Habing H (2007) Lithium and zirconium abundances in massive Galactic O-rich AGB stars. *A&A*462:711–730, DOI 10.1051/0004-6361:20065785, [arXiv:astro-ph/0609106](https://arxiv.org/abs/astro-ph/0609106)
- Goriely S, Mowlavi N (2000) Neutron-capture nucleosynthesis in AGB stars. *A&A*362:599–614
- Guelin M, Forestini M, Valiron P, Ziurys LM, Anderson MA, Cernicharo J, Kahane C (1995) Nucleosynthesis in AGB stars: Observation of Mg-25 and Mg-26 in IRC+10216 and possible detection of Al-26. *A&A*297:183–196
- Hampel W, Heusser G, Kiko J, Kirsten T, Laubenstein M, Pernicka E, Rau W, Roenn U, Schlosser C, Wojcik M, von Ammon R, Ebert KH, Fritsch T, Heidt D, Henrich E, Stieglitz L, Weirich F, Balata M, Hartmann FX, Sann M, Bellotti E, Cattadori C, Cremonesi O, Ferrari N, Fiorini E, Zanotti L, Altmann M, von Feilitzsch F, Moessbauer R, Berthomieu G, Schatzman E, Carmi I, Dostrovsky I, Bacci C, Belli P, Bernabei R, D’Angelo S, Paoluzi L, Bevilacqua A, Cribier M, Gosset L, Rich J, Spiro M, Tao C, Vignaud D, Boger J, Hahn RL, Rowley JK, Stoener RW,

- Weneser J (1998) Final results of the ^{51}Cr neutrino source experiments in GALLEX. *Physics Letters B* 420:114–126
- Harris MJ, Lambert DL, Hinkle KH, Gustafsson B, Eriksson K (1987) Oxygen isotopic abundances in evolved stars. III - 26 carbon stars. *ApJ*316:294–304, DOI 10.1086/165201
- Herwig F (2005) Evolution of Asymptotic Giant Branch Stars. *ARA&A*43:435–479, DOI 10.1146/annurev.astro.43.072103.150600
- Herwig F, Bloeker T, Schoenberner D, El Eid M (1997) Stellar evolution of low and intermediate-mass stars. IV. Hydrodynamically-based overshoot and nucleosynthesis in AGB stars. *A&A*324:L81–L84, [arXiv:astro-ph/9706122](#)
- Herwig F, Blöcker T, Langer N, Driebe T (1999) On the formation of hydrogen-deficient post-AGB stars. *A&A*349:L5–L8, [arXiv:astro-ph/9908108](#)
- Hoffman RD, Müller B, Janka H (2008) Nucleosynthesis in O-Ne-Mg Supernovae. *ApJ*676:L127–L130, DOI 10.1086/587621, 0712.4257
- Hoppe P, Ott U (1997) Mainstream silicon carbide grains from meteorites. In: Bernatowicz TJ, Zinner E (eds) *American Institute of Physics Conference Series*, American Institute of Physics Conference Series, vol 402, pp 27–58, DOI 10.1063/1.53314
- Hoppe P, Annen P, Strebel R, Eberhardt P, Gallino R, Lugaro M, Amari S, Lewis RS (1997) Meteoritic Silicon Carbide Grains with Unusual Si Isotopic Compositions: Evidence for an Origin in Low-Mass, Low-Metallicity Asymptotic Giant Branch Stars. *ApJ*487:L101+, DOI 10.1086/310869
- Hoppe P, Besmehn A (2002) Evidence for Extinct Vanadium-49 in Presolar Silicon Carbide Grains from Supernovae. *ApJ*576:L69–L72, DOI 10.1086/342785
- Humayun M, Brandon AD (2007) s-Process Implications from Osmium Isotope Anomalies in Chondrites. *ApJ*664:L59–L62, DOI 10.1086/520636
- Iben I Jr (1975) Thermal pulses; p-capture, alpha-capture, s-process nucleosynthesis; and convective mixing in a star of intermediate mass. *ApJ*196:525–547, DOI 10.1086/153433
- Iben I Jr, Renzini A (1982) On the formation of carbon star characteristics and the production of neutron-rich isotopes in asymptotic giant branch stars of small core mass. *ApJ*263:L23–L27, DOI 10.1086/183916
- Iben I Jr, Renzini A (1983) Asymptotic giant branch evolution and beyond. *ARA&A*21:271–342, DOI 10.1146/annurev.aa.21.090183.001415
- Iben I Jr, Truran JW (1978) On the surface composition of thermally pulsing stars of high luminosity and on the contribution of such stars to the element enrichment of the interstellar medium. *ApJ*220:980–995, DOI 10.1086/155986
- Iliadis C, D'Auria JM, Starrfield S, Thompson WJ, Wiescher M (2001) Proton-induced Thermonuclear Reaction Rates for A=20–40 Nuclei. *ApJS*134:151–171, DOI 10.1086/320364
- Iliadis C, Angulo C, Descouvemont P, Lugaro M, Mohr P (2008) New reaction rate for $\text{O}16(p,\gamma)\text{F}17$ and its influence on the oxygen isotopic ratios in massive AGB stars. *Phys. Rev. C*77(4):045802, DOI 10.1103/PhysRevC.77.045802, 0803.2757
- Itoh N, Adachi T, Nakagawa M, Kohyama Y, Munakata H (1989) Neutrino energy loss in stellar interiors. III - Pair, photo-, plasma, and bremsstrahlung processes. *ApJ*339:354–364, DOI 10.1086/167301
- Izzard RG, Lugaro M, Karakas AI, Iliadis C, van Raai M (2007) Reaction rate uncertainties and the operation of the NeNa and MgAl chains during HBB in intermediate-mass AGB stars. *A&A*466:641–648, DOI 10.1051/0004-6361:20066903, [arXiv:astro-ph/0703078](#)
- Jonsell K, Barklem PS, Gustafsson B, Christlieb N, Hill V, Beers TC, Holmberg J (2006) The Hamburg/ESO R-process enhanced star survey (HERES). III. HE 0338-3945 and the formation of the r + s stars. *A&A*451:651–670, DOI 10.1051/0004-6361:20054470, [arXiv:astro-ph/0601476](#)
- Jorissen A, Van Eck S, Mayor M, Udry S (1998) Insights into the formation of barium and Tc-poor S stars from an extended sample of orbital elements. *A&A*332:877–903, [arXiv:astro-ph/9801272](#)

- Kaeppler F, Beer H, Wisshak K, Clayton DD, Macklin RL, Ward RA (1982) S-process studies in the light of new experimental cross sections - Distribution of neutron fluences and r-process residuals. *ApJ*257:821–846, DOI 10.1086/160033
- Karakas A, Lattanzio JC (2007) Stellar Models and Yields of Asymptotic Giant Branch Stars. *Publications of the Astronomical Society of Australia* 24:103–117, DOI 10.1071/AS07021, 0708.4385
- Lambert DL, Smith VV, Busso M, Gallino R, Straniero O (1995) The Chemical Composition of Red Giants. IV. The Neutron Density at the s-Process Site. *ApJ*450:302–317, DOI 10.1086/176141
- Langer N, Heger A, Wellstein S, Herwig F (1999) Mixing and nucleosynthesis in rotating TP-AGB stars. *A&A*346:L37–L40, [arXiv:astro-ph/9904257](https://arxiv.org/abs/astro-ph/9904257)
- Lattanzio JC, Wood PR (2004) Evolution, Nucleosynthesis and Pulsation of AGB stars. In: Habing HJ, Olofsson H (eds) *Asymptotic Giant Branch Stars*, *Astronomy and Astrophysics Library*, Springer-Verlag, Berlin, vol 145, pp 23–104
- Lewis RS, Amari S, Anders E (1994) Interstellar grains in meteorites: II. SiC and its noble gases. *GeoCh.Acta*58:471–494, DOI 10.1016/0016-7037(94)90478-2
- Limongi M, Chieffi A (2006) The Nucleosynthesis of ^{26}Al and ^{60}Fe in Solar Metallicity Stars Extending in Mass from 11 to 120 solar masses: The Hydrostatic and Explosive Contributions. *ApJ*647:483–500, DOI 10.1086/505164
- Lodders K, Fegley B Jr (1993) The origin of circumstellar silicon carbide grains found in meteorites. *Meteoritics* 30:661–678
- Lucatello S, Tsangarides S, Beers TC, Carretta E, Gratton RG, Ryan SG (2005) The Binary Frequency Among Carbon-enhanced, s-Process-rich, Metal-poor Stars. *ApJ*625:825–832, DOI 10.1086/428104, [arXiv:astro-ph/0412422](https://arxiv.org/abs/astro-ph/0412422)
- Lugaro M (2005) Stardust from meteorites. An introduction to presolar grains
- Lugaro M, Karakas AI (2008) ^{26}Al and ^{60}Fe yields from AGB stars. *New Astronomy Review* 52:416–418, DOI 10.1016/j.newar.2008.05.005
- Lugaro M, Davis AM, Gallino R, Pellin MJ, Straniero O, Käppeler F (2003a) Isotopic Compositions of Strontium, Zirconium, Molybdenum, and Barium in Single Presolar SiC Grains and Asymptotic Giant Branch Stars. *ApJ*593:486–508, DOI 10.1086/376442
- Lugaro M, Herwig F, Lattanzio JC, Gallino R, Straniero O (2003b) s-Process Nucleosynthesis in Asymptotic Giant Branch Stars: A Test for Stellar Evolution. *ApJ*586:1305–1319, DOI 10.1086/367887, [arXiv:astro-ph/0212364](https://arxiv.org/abs/astro-ph/0212364)
- Lugaro M, Karakas AI, Nittler LR, Alexander CMO'D, Hoppe P, Iliadis C, Lattanzio JC (2007) On the asymptotic giant branch star origin of peculiar spinel grain OC2. *A&A*461:657–664, DOI 10.1051/0004-6361:20065768, [arXiv:astro-ph/0610464](https://arxiv.org/abs/astro-ph/0610464)
- Marhas KK, Hoppe P, Ott U (2007) NanoSIMS studies of Ba isotopic compositions in single presolar silicon carbide grains from AGB stars and supernovae. *Meteoritics and Planetary Science* 42:1077–1101
- McDonald AB, Ahmad QR, Allen RC, Andersen TC, Anglin JD, Barton JC, Beier EW, Bercovitch M, Bigu J, Biller SD, Black RA, Blevis I, Boardman RJ, Boger J, Bonvin E, Boulay MG, Bowler MG, Bowles TJ, Brice SJ, Browne MC, Bullard TV, Bühler G, Cameron J, Chan YD, Chen HH, Chen M, Chen X, Cleveland BT, Clifford ETH, Cowan JHM, Cowen DF, Cox GA, Dai X, Dalnoki-Veress F, Davidson WF, Doe PJ, Doucas G, Dragowsky MR, Duba CA, Duncan FA, Dunford M, Dunmore JA, Earle ED, Elliott SR, Evans HC, Ewan GT, Farine J, Fergani H, Ferraris AP, Ford RJ, Formaggio JA, Fowler MM, Frame K, Frank ED, Frati W, Gagnon N, Germani JV, Gil S, Graham K, Grant DR, Hahn RL, Hallin AL, Hallman ED, Hamer AS, Hamian AA, Handler WB, Haq RU, Hargrove CK, Harvey PJ, Hazama R, Heeger KM, Heintzelman WJ, Heise J, Helmer RL, Hepburn JD, Heron H, Hewett J, Hime A, Howe M, Hykawy JG, Isaac MCP, Jagam P, Jelley NA, Jillings C, Jonkmans G, Kazkaz K, Keener PT, Klein JR, Knox AB, Komar RJ, Kouzes R, Kutter T, Kyba CCM, Law J, Lawson IT, Lay M, Lee HW, Lesko KT, Leslie JR, Levine I, Locke W, Luoma S, Lyon J, Majerus S, Mak HB, Maneira J, Manor J, Marino AD, McCauley N, McDonald DS, McFarlane K, McGregor G, Drees RM, Mifflin C, Miller GG, Milton G, Moffat BA, Moorhead M, Nally CW, Neubauer MS, Newcomer FM,

- Ng HS, Noble AJ, Norman EB, Novikov VM, O'Neill M, Okada CE, Ollerhead RW, Omori M, Orrell JL, Oser SM, Poon AWP, Radcliffe TJ, Roberge A, Robertson BC, Robertson RG, Rosendahl SSE, Rowley JK, Rusu VL, Saettler E, Schaffer KK, Schwendener MH, Schülke A, Seifert H, Shatkey M, Simpson JJ, Sims CJ, Sinclair D, Skensved P, Smith AR, Smith MWE, Spreitzer T, Starinsky N, Steiger TD, Stokstad RG, Stonehill LC, Storey RS, Sur B, Tafirout R, Tagg N, Tanner NW, Taplin RK, Thorman M, Thornewell PM, Trent PT, Tserkovnyak YI, van Berg R, van de Water RG, Virtue CJ, Waltham CE, Wang J, Wark DL, West N, Wilhelmy JB, Wilkerson JF, Wilson JR, Wittich P, Wouters JM, Yeh M (2002) Direct Evidence for Neutrino Flavor Transformation from Neutral-Current Interactions in SNO. In: V Elias, R Epp, & R C Myers (ed) *Theoretical Physics: MRST 2002*, American Institute of Physics Conference Series, vol 646, pp 43–58, DOI 10.1063/1.1524553
- McWilliam A, Lambert DL (1988) Isotopic magnesium abundances in stars. *MNRAS* 230:573–585
- Mowlavi N, Meynet G (2000) Aluminum 26 production in asymptotic giant branch stars. *A&A* 361:959–976
- Mowlavi N, Goriely S, Arnould M (1998) The survival of ^{205}Pb in intermediate-mass AGB stars. *A&A* 330:206–214, [arXiv:astro-ph/9711025](https://arxiv.org/abs/astro-ph/9711025)
- Nichols RH Jr, Hohenberg CM, Amari S, Lewis RS (1991) $^{22}\text{Ne-E(H)}$ and ^4He Measured in individual SiC grains using laser gas extraction. *Meteoritics* 26:377–378
- Nicolussi GK, Davis AM, Pellin MJ, Lewis RS, Clayton RN, Amari S (1997) s-process zirconium in presolar silicon carbide grains. *Science* 277:1281–1283, DOI 10.1126/science.277.5330.1281
- Nicolussi GK, Pellin MJ, Lewis RS, Davis AM, Amari S, Clayton RN (1998a) Molybdenum Isotopic Composition of Individual Presolar Silicon Carbide Grains from the Murchison Meteorite. *GeoCh.Acta* 62:1093–1104, DOI 10.1016/S0016-7037(98)00038-6
- Nicolussi GK, Pellin MJ, Lewis RS, Davis AM, Clayton RN, Amari S (1998b) Strontium Isotopic Composition in Individual Circumstellar Silicon Carbide Grains: A Record of s-Process Nucleosynthesis. *Physical Review Letters* 81:3583–3586, DOI 10.1103/PhysRevLett.81.3583
- Nittler LR, Hoppe P, Alexander CMO'D, Amari S, Eberhardt P, Gao X, Lewis RS, Strebel R, Walker RM, Zinner E (1995) Silicon Nitride from Supernovae. *ApJ* 453:L25–L28, DOI 10.1086/309743
- Nittler LR, Alexander CMO'D, Gao X, Walker RM, Zinner E (1997) Stellar Sapphires: The Properties and Origins of Presolar Al_2O_3 in Meteorites. *ApJ* 483:475–495, DOI 10.1086/304234
- Nittler LR, Alexander CMO'D, Gallino R, Hoppe P, Nguyen AN, Stadermann FJ, Zinner EK (2008) Aluminum-, Calcium- and Titanium-rich Oxide Stardust in Ordinary Chondrite Meteorites. *ApJ* 682:1450–1478, DOI 10.1086/589430, 0804.2866
- Nollett KM, Busso M, Wasserburg GJ (2003) Cool Bottom Processes on the Thermally Pulsing Asymptotic Giant Branch and the Isotopic Composition of Circumstellar Dust Grains. *ApJ* 582:1036–1058, DOI 10.1086/344817, [arXiv:astro-ph/0211271](https://arxiv.org/abs/astro-ph/0211271)
- Oberauer L (2010) Results from the solar neutrino experiment BOREXINO. *Journal of Physics Conference Series* 203(1):012081, DOI 10.1088/1742-6596/203/1/012081
- Ott U, Begemann F (1990) Discovery of s-process barium in the Murchison meteorite. *ApJ* 353:L57–L60, DOI 10.1086/185707
- Pignatari M, Gallino R, Straniero O, Reifarth R, Käppeler F, Davis AM (2004) Stellar origin of the meteoritic Xe-S anomalous component. *Memorie della Societa Astronomica Italiana* 75:182–185
- Pignatari M, Gallino R, Amari S, Davis AM (2006) Krypton in presolar mainstream SiC grains from AGB stars. *Memorie della Societa Astronomica Italiana* 77:897–902
- Podosek FA, Prombo CA, Amari S, Lewis RS (2004) s-Process Sr Isotopic Compositions in Presolar SiC from the Murchison Meteorite. *ApJ* 605:960–965, DOI 10.1086/382650
- Prombo CA, Podosek FA, Amari S, Lewis RS (1993) S-process Ba isotopic compositions in presolar SiC from the Murchison meteorite. *ApJ* 410:393–399, DOI 10.1086/172756
- Raiteri CM, Gallino R, Busso M (1992) S-processing in massive stars as a function of metallicity and interpretation of observational trends. *ApJ* 387:263–275, DOI 10.1086/171078

- Rauscher T, Thielemann FK (2000) Astrophysical Reaction Rates From Statistical Model Calculations. *Atomic Data and Nuclear Data Tables* 75:1–351, DOI 10.1006/adnd.2000.0834, arXiv:astro-ph/0004059
- Rugel G, Faestermann T, Knie K, Korschinek G, Poutivtsev M, Schumann D, Kivel N, Günther-Leopold I, Weinreich R, Wohlmuther M (2009) New Measurement of the Fe60 Half-Life. *Physical Review Letters* 103(7):072502, DOI 10.1103/PhysRevLett.103.072502
- Savina MR, Davis AM, Tripa CE, Pellin MJ, Clayton RN, Lewis RS, Amari S, Gallino R, Lugaro M (2003a) Barium isotopes in individual presolar silicon carbide grains from the Murchison meteorite. *GeoCh.Acta* 67:3201–3214, DOI 10.1016/S0016-7037(03)00083-8
- Savina MR, Pellin MJ, Tripa CE, Veryovkin IV, Calaway WF, Davis AM (2003b) Analyzing individual presolar grains with CHARISMA. *GeoCh.Acta* 67:3215–3225, DOI 10.1016/S0016-7037(03)00082-6
- Savina MR, Davis AM, Tripa CE, Pellin MJ, Gallino R, Lewis RS, Amari S (2004) Extinct Technetium in Silicon Carbide Stardust Grains: Implications for Stellar Nucleosynthesis. *Science* 303:649–652, DOI 10.1126/science.3030649
- Sedlmayr E, Dominik C (1995) Dust Driven Winds. *Space Science Reviews* 73:211–272, DOI 10.1007/BF00751238
- Siess L (2006) Evolution of massive AGB stars. I. Carbon burning phase. *A&A* 448:717–729, DOI 10.1051/0004-6361:20053043
- Siess L (2007) Evolution of massive AGB stars. II. model properties at non-solar metallicity and the fate of Super-AGB stars. *A&A* 476:893–909, DOI 10.1051/0004-6361:20078132
- Siess L, Arnould M (2008) Production of ^{26}Al by super-AGB stars. *A&A* 489:395–402, DOI 10.1051/0004-6361:200810147
- Smith VV, Lambert DL (1986) The chemical composition of red giants. II - Helium burning and the s-process in the MS and S stars. *ApJ* 311:843–863, DOI 10.1086/164823
- Snedden C, Cowan JJ, Lawler JE, Burles S, Beers TC, Fuller GM (2002) Europium Isotopic Abundances in Very Metal Poor Stars. *ApJ* 566:L25–L28, DOI 10.1086/339471, arXiv:astro-ph/0201456
- Snedden C, Cowan JJ, Gallino R (2008) Neutron-Capture Elements in the Early Galaxy. *ARA&A* 46:241–288, DOI 10.1146/annurev.astro.46.060407.145207
- Speck AK, Barlow MJ, Sylvester RJ, Hofmeister AM (2000) Dust features in the 10- μm infrared spectra of oxygen-rich evolved stars. *A&AS* 146:437–464, DOI 10.1051/aas:2000274
- Speck AK, Corman AB, Wakeman K, Wheeler CH, Thompson G (2009) Silicon Carbide Absorption Features: Dust Formation in the Outflows of Extreme Carbon Stars. *ApJ* 691:1202–1221, DOI 10.1088/0004-637X/691/2/1202, 0810.2599
- Stancliffe RJ, Chieffi A, Lattanzio JC, Church RP (2009) Why Do Low-Mass Stars Become Red Giants? *Publications of the Astronomical Society of Australia* 26:203–208, DOI 10.1071/AS08060, 0902.0406
- Terada K, Itoh K, Hidaka H, Yoshida T, Iwamoto N, Aoki W, Williams IS (2006) Eu isotope measurements on single SiC grains from the Murchison meteorite: A new probe of s-process conditions in parent Asymptotic Giant Branch stars. *New Astronomy Review* 50:582–586, DOI 10.1016/j.newar.2006.06.006
- Travaglio C, Gallino R, Amari S, Zinner E, Woosley S, Lewis RS (1999) Low-Density Graphite Grains and Mixing in Type II Supernovae. *ApJ* 510:325–354, DOI 10.1086/306551
- Treffers R, Cohen M (1974) High-resolution spectra of cool stars in the 10- and 20-micron regions. *ApJ* 188:545–552, DOI 10.1086/152746
- Trigo-Rodriguez JM, Anibal Garcia-Hernandez D, Lugaro M, Karakas AI, van Raai M, Garcia Lario P, Manchado A (2009) The Role of Massive Agb Stars in the Early Solar System Composition. *Meteoritics and Planetary Science* 44:627–641
- Überseder E, Reifarth R, Schumann D, Dillmann I, Pardo CD, Görres J, Heil M, Käppeler F, Marganiec J, Neuhausen J, Pignatari M, Voss F, Walter S, Wiescher M (2009) Measurement of the $^{60}\text{Fe}(n,\gamma)^{61}\text{Fe}$ Cross Section at Stellar Temperatures. *Physical Review Letters* 102(15):151101, DOI 10.1103/PhysRevLett.102.151101

- Uttenthaler S, Lebzelter T, Palmerini S, Busso M, Aringer B, Lederer MT (2007) Low-mass lithium-rich AGB stars in the Galactic bulge: evidence for cool bottom processing? *A&A*471:L41–L45, DOI 10.1051/0004-6361:20077879, 0707.1380
- van Raai MA, Lugaro M, Karakas AI, García-Hernández DA (2008a) Rubidium and Zirconium Production in Massive AGB Stars. In: Guandalini R, Palmerini S, Busso M (eds) *Evolution and Nucleosynthesis in AGB Stars*, American Institute of Physics Conference Series, vol 1001, pp 146–153, DOI 10.1063/1.2916957
- van Raai MA, Lugaro M, Karakas AI, Iliadis C (2008b) Reaction rate uncertainties and ^{26}Al in AGB silicon carbide stardust. *A&A*478:521–526, DOI 10.1051/0004-6361:20078307, 0712.3702
- Verhovskiy AB, Wright IP, Pillinger CT (2004) Astrophysical Significance of Asymptotic Giant Branch Stellar Wind Energies Recorded in Meteoritic SiC Grains. *ApJ*607:611–619, DOI 10.1086/383230
- Vollmer C, Hoppe P, Brenker FE (2008) Si Isotopic Compositions of Presolar Silicate Grains from Red Giant Stars and Supernovae. *ApJ*684:611–617, DOI 10.1086/589913
- Wanajo S, Nomoto K, Janka H, Kitaura FS, Müller B (2009) Nucleosynthesis in Electron Capture Supernovae of Asymptotic Giant Branch Stars. *ApJ*695:208–220, DOI 10.1088/0004-637X/695/1/208, 0810.3999
- Wasserburg GJ, Busso M, Gallino R, Raiteri CM (1994) Asymptotic Giant Branch stars as a source of short-lived radioactive nuclei in the solar nebula. *ApJ*424:412–428, DOI 10.1086/173899
- Wasserburg GJ, Boothroyd AI, Sackmann IJ (1995) Deep Circulation in Red Giant Stars: A Solution to the Carbon and Oxygen Isotope Puzzles? *ApJ*447:L37–L40, DOI 10.1086/309555
- Wasserburg GJ, Busso M, Gallino R, Nollett KM (2006) Short-lived nuclei in the early Solar System: Possible AGB sources. *Nuclear Physics A* 777:5–69, DOI 10.1016/j.nuclphysa.2005.07.015, arXiv:astro-ph/0602551
- Whittet DCB (1992) Dust in the galactic environment
- Willson LA (2000) Mass Loss From Cool Stars: Impact on the Evolution of Stars and Stellar Populations. *ARA&A*38:573–611, DOI 10.1146/annurev.astro.38.1.573
- Wood PR (1979) Pulsation and mass loss in Mira variables. *ApJ*227:220–231, DOI 10.1086/156721
- Yin QZ, Lee CTA, Ott U (2006) Signatures of the s-Process in Presolar Silicon Carbide Grains: Barium through Hafnium. *ApJ*647:676–684, DOI 10.1086/505188
- Zinner E, Amari S, Lewis RS (1991) S-process Ba, Nd, and Sm in presolar SiC from the Murchison meteorite. *ApJ*382:L47–L50, DOI 10.1086/186210
- Zinner E, Nittler LR, Gallino R, Karakas AI, Lugaro M, Straniero O, Lattanzio JC (2006) Silicon and Carbon Isotopic Ratios in AGB Stars: SiC Grain Data, Models, and the Galactic Evolution of the Si Isotopes. *ApJ*650:350–373, DOI 10.1086/506957
- Zinner E, Amari S, Guinness R, Jennings C, Mertz AF, Nguyen AN, Gallino R, Hoppe P, Lugaro M, Nittler LR, Lewis RS (2007) NanoSIMS isotopic analysis of small presolar grains: Search for Si_3N_4 grains from AGB stars and Al and Ti isotopic compositions of rare presolar SiC grains. *GeoCh.Acta*71:4786–4813, DOI 10.1016/j.gca.2007.07.012

Appendix A

Radionuclides and their Stellar Origins

Maria Lugaro¹ and Alessandro Chieffi²

We supplement this book, and in particular the discussion of stellar nucleosynthesis presented in Chapter 3, by a list of the unstable isotopes at which branching points that become relevant in the *s*-process reaction chain in AGB stars are activated. For sake of clarity and a better understanding it is advisable to go through the list with a chart of the nuclides at hand. For each branching point a brief description of its operation and its relevance in the study of the *s*-process in AGB stars is presented. All listed isotopes suffer β^- decay, unless specified otherwise. It should also be noted that usually in *s*-process conditions nuclear energy metastable levels higher than the ground state are not populated, thus the effect of these states does not need to be included in the study of branching points, except for the special cases reported in the list (see also Ward, 1977).

Branching factors (see Sect. 3.5.2) for each branching point can be calculated for a given temperature, density, and neutron density conditions referring to Takahashi and Yokoi (1987) for the β decay rates, and to Rauscher and Thielemann (2000) for the neutron capture cross section, unless advised otherwise in the description below.³

³⁵S This branching point may lead to production of the rare neutron-rich ³⁶S, whose abundance can be observed in stars via molecular lines, and may be measured in sulphur-rich meteoritic materials (for discussion and models see Mauersberger et al, 2004).

³⁶Cl and ⁴¹Ca These are both long-living nuclei produced and destroyed - mostly via (*n, p*) and (*n, α*) channels - via neutron captures in AGB stars, and discussed in detail in Section 3.6.4 of Chapter 3. While ³⁶Cl behaves as a stable nucleus during the *s*-process, the half life of ⁴¹Ca against electron captures has a strong temperature and density dependence, which could make it act as a branching

¹ Monash University, Victoria 3800, Australia

² I.N.A.F., 00133 Roma, Italy

³ Maria Lugaro thanks Roberto Gallino and Franz Kaeppeler for communicating the passion for branching points and for help with this section.

point and most importantly prevent its survival instellar environments as in the case, e.g., of the other long-living nucleus ^{205}Pb .

⁴⁵**Ca** This branching point may lead to production of the rare neutron-rich ^{46}Ca , which could be measured in Ca-rich meteoritic material.

⁵⁹**Fe** This important branching point leads to the production of the long-living radioactive nucleus ^{60}Fe . See Section 3.6.3 of Chapter 3 for a detailed description and AGB model results.

⁶³**Ni** The half life of this nucleus decreases from 100 yr to $\simeq 12$ yr at 300 MK. The associated branching point affects the production of the rare neutron-rich ^{64}Ni as well as the $^{65}\text{Cu}/^{63}\text{Cu}$ ratio.

⁶⁴**Cu** The half life of this nucleus is short, of the order of a few hours, however, this isotope is a branching point on the s -process paths as it has comparable β^+ and β^- decay rates. The branching point may affect the production of ^{64}Ni and ^{65}Cu .

⁶⁵**Zn** This nucleus suffers β^+ decay and the branching point may affect the production of ^{65}Cu .

⁷¹**Ge** This nucleus suffers β^+ decay and the branching point may affect the production of ^{71}Ga .

⁷⁹**Se** This branching point may lead to production of the long-living radioactive isotope ^{81}Kr . This production occurs when the temperature increases in the AGB thermal pulse, and the half life of ^{79}Se decreases from the terrestrial half life of 65,000 yr to roughly 4 yr at 300 MK due to population of the shorter-living isomeric state (Klay and Käppeler, 1988, and see Section 3.6.5 for model results). Operation of this branching point also affects the $^{81}\text{Br}/^{79}\text{Br}$ ratio.

⁸⁰**Br** The half life of this nucleus is short, of the order of minutes, however, it is a branching point on the s -process paths as it can decay both β^+ and β^- , with the β^- roughly ten times faster than the β^+ channel. It can affect the production of ^{81}Kr .

⁸¹**Kr** This nucleus is too long living ($T_{1/2} = 0.23$ Myr, down to 2300 yr at temperature 300 MK) to act as a branching point during the s -process and rather behaves as a stable nucleus. Its production during the s -process is discussed in detail in Section 3.6.5 of Chapter 3. Its radiogenic decay leads to ^{81}Br .

⁸⁵**Kr** The relatively long half life of ^{85}Kr (11 yr) allows this branching point to activate already at low neutron densities, $> 5 \times 10^8 \text{ n/cm}^3$. The actual operation of this branching point is complicated by the fact that roughly 40% of $^{84}\text{Kr}(n, \gamma)$ reactions during the s -process result in the production of the isomeric state of ^{85}Kr . Approximately 80% of these nuclei quickly decay into ^{85}Rb , with a half live of 4.5 hours, while the remaining 20% relax into the ground state. The production of ^{87}Rb , a very long-living isotope with half live of 48 Gyr and a magic number of neutrons $N=50$, has traditionally been attributed to the activation of the branching point at ^{85}Kr (Lambert et al, 1995; Abia et al, 2001). van Raai et al (2008) showed that the activation of the branching point at ^{85}Kr mostly results in the production of ^{86}Kr , a nucleus with a magic number of neutrons $N=50$ and a very small neutron capture cross section of only $\simeq 3.4$ mbarn. ^{86}Kr is thus more likely to accumulate than to capture the further neutron that would allow the production

of ^{87}Rb . The importance of the production of ^{86}Kr in meteoritic SiC grains and the *s*-process is discussed in Section 3.5.5 of Chapter 3.

⁸⁶**Rb** The branching point at ^{86}Rb is activated at relatively high neutron densities, above 10^{10} n/cm^3 , being the half life of this nucleus 18.7 days, and it leads directly to the production of ^{87}Rb . The importance of ^{87}Rb in *s*-process observations and models is discussed in Section 3.5.4 of Chapter 3.

^{89,90}**Sr** and ⁹¹**Y** The branching point at ^{89}Sr may produce the unstable ^{90}Sr , also a branching point producing ^{91}Sr , which quickly decays into unstable ^{91}Y . This is also a branching point, producing ^{92}Y , which quickly decays into stable ^{92}Zr . The final result of the operation of this chain of branching points is to decrease the production of ^{90}Zr and ^{91}Zr , with respect to that of ^{92}Zr . This point is discussed by Lugaro et al (2003), in relevance to the Zr isotopic ratios measured in meteoritic silicon carbide (SiC) grains from AGB stars.

⁹³**Zr** This nucleus is too long-living ($T_{1/2} = 1.5 \text{ Myr}$) to act as a branching point during the *s*-process and rather behaves as a stable nucleus (see Section 3.5.2 and Fig. 3.10 of Chapter 3), with an experimentally determined neutron-capture cross section (Macklin, 1985b). Its production during the *s*-process is discussed in detail in Section 3.6.5 of Chapter 3. Its radiogenic decay produces most of the solar abundance of ^{93}Nb . (A small fraction of ^{93}Nb is also contributed by the radiogenic decay of ^{93}Mo , $T_{1/2} = 3500 \text{ yr}$, which is not on the main *s*-process path but can be produced by neutron-capture on the relatively abundant *p*-only ^{92}Mo , 15% of solar Mo).

⁹⁵**Zr** This important branching point can lead to production by the *s*-process of ^{96}Zr if $N_n > 5 \times 10^8 \text{ n/cm}^3$. Zr isotopic ratios have been estimated in MS and S stars via molecular lines and measured in meteoritic SiC grains, providing constraints on the neutron density in the thermal pulses. This point is further discussed in Secs. 3.5.4 and 3.5.5.

^{94,95}**Nb** The half life of ^{94}Nb decreases from terrestrial 20,000 yr to $\simeq 0.5 \text{ yr}$ at 100 MK and $\simeq 9 \text{ days}$ at 300 MK. This branching point can produce the unstable ^{95}Nb , which is also a branching point producing the unstable ^{96}Nb , which quickly decays into stable ^{96}Mo . Via the operation of the ^{94}Nb branching point the ^{94}Mo nucleus is skipped during the *s*-process chain, this nucleus is in fact classified as a *p*-only nucleus.

⁹⁹**Tc** The half life of ^{99}Tc is 0.21 Myr, and decreases to 0.11 Myr at 100 MK and to 4.5 yr at 300 MK. Thus, the neutron-capture path of the branching point is mostly open, producing ^{100}Tc , which quickly decays into ^{100}Ru , thus skipping ^{99}Ru (Fig. 3.10). Then, radiogenic decay of ^{99}Tc produces ^{99}Ru . The production of ^{99}Tc is discussed in detail in Sec 3.6.5, and mentioned in Section 3.6.5.2 of Chapter 3 in relation to ^{99}Ru in meteoritic SiC grains.

¹⁰⁷**Pd** This nucleus is too long-living ($T_{1/2} = 6.5 \text{ Myr}$, down to $\simeq 700 \text{ yr}$ at 300 MK) to act as a branching point during the *s*-process and rather behaves as a stable nucleus, with an experimentally determined neutron-capture cross section (Macklin, 1985a). Its production during the *s*-process is discussed in detail in Section 3.6.5 of Chapter 3. Its radiogenic decay is responsible for production of ^{107}Ag .

¹²⁸**I** The decay half life of this nucleus is too short to allow for neutron captures, however, there is a marginal branching point here due to the fact that ¹²⁸I has both β^+ and β^- decay channels. The β^+ channel has significant temperature and density dependence and represents only a few percent of the decay rate. Nevertheless, this branching point has been investigated in detail because it affects the precise determination of relative abundances of the two *s*-only isotopes ¹²⁸Xe and ¹³⁰Xe, and because the timescale for its activation of the order of 25 minutes is comparable to that of the convective turn-over timescale of the material inside AGB thermal pulses of hours (Reifarth et al, 2004).

¹³³**Xe** May lead to production of the ¹³⁴Xe. Of interest in relation to the Xe-S component from SiC grains in primitive meteorites, as discussed in Section 3.5.5 of Chapter 3.

^{134,135,136,137}**Cs** The chain of branching points at the Cs isotopes is of particular interest because it affects the isotopic composition of the *s*-process element Ba and in particular the relative abundances of the two *s*-only nuclei ¹³⁴Ba and ¹³⁶Ba, as it is discussed in Section 3.5.5 in relation to Ba data from meteoritic SiC grains. The branching point at ¹³⁴Cs allows production of the long-living isotope ¹³⁵Cs (see Section 3.6.5 of Chapter 3 for model results). The half lives of both ¹³⁴Cs and ¹³⁵Cs have a strong theoretical temperature dependence, decreasing by orders of magnitude in stellar conditions. Specifically for the long-living ¹³⁵Cs, $T_{1/2}$ varies from terrestrial of 2 Myr down to $\simeq 200$ yr at 300 MK, while its neutron-capture cross section has been experimentally determined (Jaag et al, 1997). The branching point at ¹³⁵Cs can produce the unstable ¹³⁶Cs, which is also a branching point producing the unstable ¹³⁷Cs. With a constant half life of $\simeq 30$ yr, this is also a branching point producing the unstable ¹³⁸Cs, which quickly decays into stable ¹³⁸Ba.

¹⁴¹**Ce** This branching point may lead to production of the neutron-rich ¹⁴²Ce, thus skipping the *s*-only ¹⁴²Nd and affecting the Nd isotopic ratios, which are measured in SiC stardust grains (Gallino et al, 1997).

^{142,143}**Pr** The branching point at ¹⁴²Pr is affected by the temperature dependence of the β^- half life of ¹⁴²Pr, which increases to $\simeq 4$ days at 300 MK from the terrestrial 19 hours. The neutron-capture branch may produce the unstable ¹⁴³Pr, which is also a branching point producing the unstable ¹⁴⁴Pr, which quickly decays into ¹⁴⁴Nd. The operation of this chain of branching points may affect the isotopic composition of Nd because ¹⁴²Nd and ¹⁴³Nd are skipped by the neutron-capture flux and their abundances are decreased.

¹⁴⁷**Nd** This branching point may lead to the production of the neutron-rich “*r*-only” ¹⁴⁸Nd, which is of interest in relation to stellar SiC grain Nd data (Gallino et al, 1997).

^{147,148}**Pm** The branching point at ¹⁴⁷Pm is affected by the strong temperature dependence of the β^- decay of this nucleus, where the half life decreases from the terrestrial value of 2.6 yr down to $\simeq 1$ yr at 300 MK. The neutron-capture cross section of this nucleus is experimentally determined (Reifarth et al, 2003). When the branching is open, it produces the unstable ¹⁴⁸Pm, a branching point that may lead to production of ¹⁴⁹Pm, which quickly decays into ¹⁴⁹Sm. The

operation of this chain of branching points affects the isotopic composition of Sm, by skipping ^{147}Sm and the s -only ^{148}Sm . This is of interest in relation to stellar SiC grain Sm data (Gallino et al, 1997).

¹⁵¹**Sm** The operation of this branching point is affected by the temperature dependence of the β^- decay rate of ^{151}Sm , where the half life of this nucleus decreases from 93 yr to $\simeq 3$ yr at 300 MK. Its operation changes the $^{153}\text{Eu}/^{151}\text{Eu}$ ratio, which can be measured in stars (Section 3.5.4 of Chapter 3) and in SiC stardust grains (Section 3.5.5 of Chapter 3). Note that ^{151}Sm is one of few radioactive nuclei acting as branching points on the s -process path for which an experimental determination of the neutron capture cross section is available (Abbondanno et al, 2004; Wisshak et al, 2006).

¹⁵³**Sm** This branching point can produce the neutron-rich ^{154}Sm and affect the $^{153}\text{Eu}/^{151}\text{Eu}$ ratio.

¹⁵²**Eu** This nucleus suffers both β^- and β^+ decays, with rates showing a strong temperature dependence covering several orders of magnitude variation in stellar conditions. The β^+ decay rate also has a strong dependence on density. The operation of this branching point, in combination with that at ^{151}Sm , makes possible the production of the rare p -only isotope ^{152}Gd by the s -process.

^{154,155}**Eu** The decay rate of ^{154}Eu has a strong temperature dependence, with its half life decreasing from 8.8 yr down to $\simeq 11$ days at 300 MK. If activated, it leads to production of the unstable ^{155}Eu , a branching point also with a temperature dependence, and an experimentally determined neutron-capture cross section (Jaag and Käppeler, 1995), which may produce ^{156}Eu , which quickly decays into ^{156}Gd . The operation of this chain of branching points affects the isotopic composition of Gd, which is a refractory element present in stellar SiC grains (Yin et al, 2006).

¹⁵³**Gd** This nucleus suffers β^+ decay with a temperature dependence, where the terrestrial half life of 239 days increases with increasing the temperature by up to an order of magnitude in AGB stars conditions. The operation of this branching point may affect the $^{153}\text{Eu}/^{151}\text{Eu}$ ratio.

¹⁶³**Dy** and ^{163,164}**Ho** The nucleus ^{163}Dy is stable in terrestrial conditions, but it can become unstable inside stars: at 300 MK the half life of this isotope becomes $\simeq 18$ days. Thus, a branching can open on the s -process path, leading to the production of the unstable ^{163}Ho via β^- decay of ^{163}Dy . In this conditions, the β^+ half life of ^{163}Ho (which also has a strong temperature and density dependence) is $\simeq 12$ yr, so another branching can open on the s -process neutron capture path. Neutron captures on ^{163}Ho lead to production of the unstable ^{164}Ho , which has fast β^- and β^+ channels, both temperature dependent. The β^- channel can eventually lead to the production of ^{164}Er , a p -only nucleus, which may thus have a s -process component in its cosmic abundance.

¹⁶⁹**Er** This branching point may lead to the production of the neutron-rich ^{170}Er .

^{170,171}**Tm** The branching point at ^{170}Tm may produce the unstable ^{171}Tm , which is also a branching point (with a temperature dependence) producing the unstable ^{172}Tm , which quickly decays into ^{172}Yb . By skipping $^{171,172}\text{Yb}$ during the s -

process flux, these branching points affect the isotopic composition of Yb, which is a refractory element present in meteoritic stellar SiC grains (Yin et al, 2006).

¹⁷⁶**Lu** A branching point at ¹⁷⁶Lu is activated because of the production of the short-living (half life of $\simeq 4$ hours) isomeric state of ¹⁷⁶Lu via neutron captures on ¹⁷⁵Lu. The situation is further complicated because, at around 300 MK, the isomeric and the ground state of ¹⁷⁶Lu are connected via the thermal population of nuclear states that can act as mediators between the two. Hence, the half life of the ¹⁷⁶Lu system can decrease at such temperatures by orders of magnitude. This branching point is of importance for the production of the very long-living ground state of ¹⁷⁶Lu (half life of 380 Gyr) and of the stable ¹⁷⁶Hf, which are both *s*-only isotopes, shielded by ¹⁷⁶Yb against *r*-process production. Hence, the relative solar abundances of these two isotopes need to be matched by *s*-process in AGB stars. For details and models see Heil et al (2008); Mohr et al (2009).

¹⁷⁷**Lu** This branching point may lead to production of the unstable ¹⁷⁸Lu, which quickly decays into ¹⁷⁸Hf, thus decreasing the abundance of ¹⁷⁷Hf.

¹⁷⁹**Hf**, ^{179,180}**Ta** A branching point at ¹⁷⁹Hf may be activated on the *s*-process path because this stable nucleus becomes unstable in stellar conditions (as in the case of ¹⁶³Dy) with a β^- half life of $\simeq 40$ yr at 300 MK. This may allow the production of the unstable ¹⁷⁹Ta, which is also a branching point with a temperature-dependent β^+ decay rate, which may lead to the production of ¹⁸⁰Ta, the least abundant nucleus in the solar system (Käppeler et al, 2004), as a few percent of neutron captures on ¹⁷⁹Ta lead to production of the very long-living isomeric state of ¹⁸⁰Ta, instead of the ground state, which suffers fast β^+ and β^- decays. As in the case of ¹⁷⁶Lu, the ground and the isomeric states of ¹⁸⁰Ta can be connected via the thermal population of nuclear states that act as mediators between the two. It is still unclear if the cosmic abundance of ¹⁸⁰Ta is to be ascribed to the *s*-process or to nucleosynthetic processes in supernovae connected to neutrino fluxes.

¹⁸¹**Hf** This branching point may lead to production of the long-living radioactive nucleus ¹⁸²Hf (one of the few radioactive isotopes with an experimentally determined neutron-capture cross section available, Vockenhuber et al, 2007) whose decay into ¹⁸²W is of extreme importance for early solar system datation. The half life of ¹⁸¹Hf is relatively long in terrestrial conditions (42 days), but decreases down to 2 days at 300 MK, when the ²²Ne(α ,n)²⁵Mg reaction is activated, so the actual production of ¹⁸²Hf in AGB stars is predicted to be relatively marginal (see also Section 3.6.5 of Chapter 3).

^{182,183}**Ta** The branching point at ¹⁸²Ta is temperature dependent and may produce the unstable ¹⁸³Ta, also a branching point, producing ¹⁸⁴Ta, which quickly decays into the stable ¹⁸⁴W. These branching points may affect the isotopic composition of W, which is a refractory element that is present in stellar SiC grains (Avila et al, 2008).

¹⁸⁵**W** This branching point may produce ¹⁸⁶W, and affect the isotopic composition of W as well as the ¹⁸⁶Os/¹⁸⁸Os ratio. Its signature may be seen in data from stellar SiC grains for W and Os (Humayun and Brandon, 2007). Note that ¹⁸⁵W is one of few radioactive nuclei acting as branching points on the *s*-process path

for which an experimental determination of the neutron capture cross section is available, even though only via indirect (γ, n) studies, which have rather large uncertainties of about 30% (Sonnabend et al, 2003; Mohr et al, 2004).

- ¹⁸⁶**Re** This isotope decays in $\simeq 89$ hours, and has both β^- and β^+ decay channel. The β^- decay channel is faster by one to two orders of magnitude depending on the temperature, which also affects the β^+ decay rate. This branching point can affect the production of ¹⁸⁶Os, ¹⁸⁶W, and the very long-living ¹⁸⁷Re, whose slow decay into ¹⁸⁷Os is used as a cosmological clock (see discussion in Chapter 2).
- ¹⁹¹**Os** This branching point has a mild temperature dependence whereby the half life of ¹⁹¹Os decreases with the temperature from the terrestrial 15 days to $\simeq 8$ days at 300 MK. If activated, the neutron-capture branch can decrease the *s*-process abundances of ¹⁹¹Ir and ¹⁹²Pt and lead to production of ¹⁹²Os, thus affecting the isotopic composition of Os, which is measured in meteoritic materials (Brandon et al, 2005), and ¹⁹³Ir.
- ¹⁹²**Ir** This branching point can produce ¹⁹³Ir, and affect the *s*-process production of the rare proton-rich ¹⁹²Pt. A few percent of the decay rate of ¹⁹²Ir is made by β^+ decays.
- ¹⁹³**Pt** This isotope decays β^+ with a half life of $\simeq 50$ yr, which may affect the production of ¹⁹³Ir.
- ²⁰⁴**Tl** This branching point has a strong temperature dependence with its half life decreasing from the terrestrial value of $\simeq 3.8$ yr to $\simeq 7$ days at 300 MK, leading to production of the *s*-only ²⁰⁴Pb.
- ²⁰⁵**Pb** This nucleus is long-living in terrestrial conditions ($T_{1/2} = 15$ Myr), but its half life against electron captures has a strong temperature and density dependence, which affects its survival in stellar environments, as in the case of ⁴¹Ca. Its production during the *s*-process is discussed in detail in Section 3.6.5 of Chapter 3. Its radiogenic decay is responsible for production of ¹⁰⁵Tl.
- ²¹⁰**Bi** This temperature-dependent branching point may lead to production of the unstable ²¹¹Bi, which α decays into ²⁰⁷Tl, which quickly decays β^+ into ²⁰⁷Pb.
- ²¹⁰**Po** May produce ²¹¹Po, which quickly α decays into ²⁰⁷Pb. The α decay of ²¹⁰Po, and ²¹¹Bi above, represent the chain of reactions that terminates the *s*-process (Clayton and Rassbach, 1967; Ratzel et al, 2004).

To complete the picture we list nuclei that could be classified as potential *s*-process branching points, given that their terrestrial half life is greater than a few days, however, they do not open during the *s*-process because their half life decreases with the temperature to below a few days. These are: ¹⁰³Ru, ¹²³Sn, ¹²⁴Sb, ¹⁵⁶Eu, ^{160,161}Tb, ¹⁷⁵Yb, ¹⁹⁸Au, and ²⁰⁵Hg. Finally, we point out the special case of ¹⁵⁷Gd, a stable nucleus which becomes unstable at stellar temperatures, but not enough to open a branching point on the *s*-process path in AGB stars.

References

Abbondanno U, Aerts G, Alvarez-Velarde F, Álvarez-Pol H, Andriamonje S, Andrzejewski J,

- Badurek G, Baumann P, Bečvář F, Benlliure J, Berthoumieux E, Calviño F, Cano-Ott D, Capote R, Cennini P, Chepel V, Chiaveri E, Colonna N, Cortes G, Cortina D, Couture A, Cox J, Dababneh S, Dahlfors M, David S, Dolfini R, Domingo-Pardo C, Duran I, Embid-Segura M, Ferrant L, Ferrari A, Ferreira-Marques R, Fraiss-Koelbl H, Furman W, Goncalves I, Gallino R, Gonzalez-Romero E, Goverdovski A, Gramegna F, Griesmayer E, Gunsing F, Haas B, Haight R, Heil M, Herrera-Martinez A, Isaev S, Jericha E, Käppeler F, Kadi Y, Karadimos D, Kerveno M, Ketlerov V, Koehler P, Konovalov V, Krtićka M, Lamboudis C, Leeb H, Lindote A, Lopes I, Lozano M, Lukic S, Marganec J, Marrone S, Martinez-Val J, Mastinu P, Mengoni A, Milazzo PM, Molina-Coballes A, Moreau C, Mosconi M, Neves F, Oberhummer H, O'Brien S, Pancin J, Papaevangelou T, Paradela C, Pavlik A, Pavlopoulos P, Perlado JM, Perrot L, Pignatari M, Plag R, Plompen A, Plukis A, Poch A, Policarpo A, Pretel C, Quesada J, Raman S, Rapp W, Rauscher T, Reifarth R, Rosetti M, Rubbia C, Rudolf G, Rullhusen P, Salgado J, Soares JC, Stephan C, Tagliente G, Tain J, Tassan-Got L, Tavora L, Terlizzi R, Vannini G, Vaz P, Ventura A, Villamarin D, Vincente MC, Vlachoudis V, Voss F, Wendler H, Wiescher M, Wisshak K (2004) Neutron Capture Cross Section Measurement of ^{151}Sm at the CERN Neutron Time of Flight Facility (n-TOF). *Physical Review Letters* 93(16):161103, DOI 10.1103/PhysRevLett.93.161103
- Abia C, Busso M, Gallino R, Domínguez I, Straniero O, Isern J (2001) The ^{85}Kr s-Process Branching and the Mass of Carbon Stars. *ApJ* 559:1117–1134, DOI 10.1086/322383, arXiv: astro-ph/0105486
- Avila JN, Ireland TR, Holden P, Gyngard F, Bennett V., Amari S, Zinner E (2008) Tungsten Isotopic Compositions in Presolar Silicon Carbide Grains. *Meteoritics and Planetary Science Supplement* 43:5120
- Brandon AD, Humayun M, Puchtel IS, Leya I, Zolensky M (2005) Osmium Isotope Evidence for an s-Process Carrier in Primitive Chondrites. *Science* 309:1233–1236, DOI 10.1126/science.1115053
- Clayton DD, Rassbach ME (1967) Termination of the s-PROCESS. *ApJ* 148:69–85, DOI 10.1086/149128
- Gallino R, Busso M, Lugaro M (1997) Neutron capture nucleosynthesis in AGB stars. In: Bernatowicz TJ, Zinner E (eds) *American Institute of Physics Conference Series*, American Institute of Physics Conference Series, vol 402, pp 115–153, DOI 10.1063/1.53327
- Heil M, Winckler N, Dababneh S, Käppeler F, Wisshak K, Bisterzo S, Gallino R, Davis AM, Rauscher T (2008) $^{176}\text{Lu}/^{176}\text{Hf}$: A Sensitive Test of s-Process Temperature and Neutron Density in AGB Stars. *ApJ* 673:434–444, DOI 10.1086/523892
- Humayun M, Brandon AD (2007) s-Process Implications from Osmium Isotope Anomalies in Chondrites. *ApJ* 664:L59–L62, DOI 10.1086/520636
- Jaag S, Käppeler F (1995) Stellar (n, γ) cross section of the unstable isotope ^{155}Eu . *Phys. Rev. C* 51:3465–3471, DOI 10.1103/PhysRevC.51.3465
- Jaag S, Käppeler F, Koehler P (1997) The Stellar (n, γ) Cross Section of the Unstable ^{135}Cs . *Nuclear Physics A* 621:247–250, DOI 10.1016/S0375-9474(97)00247-9
- Käppeler F, Arlandini C, Heil M, Voss F, Wisshak K, Reifarth R, Straniero O, Gallino R, Masera S, Travaglio C (2004) Stellar neutron capture on $^{180}\text{Ta}^m$. II. Defining the s-process contribution to nature's rarest isotope. *Phys. Rev. C* 69(5):055802, DOI 10.1103/PhysRevC.69.055802
- Klay N, Käppeler F (1988) β -decay rate of ^{79m}Se and its consequences for the s-process temperature. *Phys. Rev. C* 38:295–306, DOI 10.1103/PhysRevC.38.295
- Lambert DL, Smith VV, Busso M, Gallino R, Straniero O (1995) The Chemical Composition of Red Giants. IV. The Neutron Density at the s-Process Site. *ApJ* 450:302–317, DOI 10.1086/176141
- Lugaro M, Davis AM, Gallino R, Pellin MJ, Straniero O, Käppeler F (2003) Isotopic Compositions of Strontium, Zirconium, Molybdenum, and Barium in Single Presolar SiC Grains and Asymptotic Giant Branch Stars. *ApJ* 593:486–508, DOI 10.1086/376442
- Macklin RL (1985a) Neutron capture measurements. *Nucl Sci Eng* 89:79
- Macklin RL (1985b) Neutron capture measurements on radioactive ^{93}Zr . *Ap&SS* 115:71–83, DOI 10.1007/BF00653828

- Mauersberger R, Ott U, Henkel C, Cernicharo J, Gallino R (2004) The abundance of ^{36}S in IRC+10216 and its production in the Galaxy. *A&A*426:219–227, DOI 10.1051/0004-6361:20040451, [arXiv:astro-ph/0407003](#)
- Mohr P, Shizuma T, Ueda H, Goko S, Makinaga A, Hara KY, Hayakawa T, Lui Y, Ohgaki H, Utsunomiya H (2004) s -process branching at ^{185}W revised. *Phys. Rev. C*69(3):032801, DOI 10.1103/PhysRevC.69.032801, [arXiv:astro-ph/0409642](#)
- Mohr P, Bisterzo S, Gallino R, Käppeler F, Kneissl U, Winckler N (2009) Properties of the 5^- state at 839 keV in Lu176 and the s-process branching at A=176. *Phys. Rev. C*79(4):045804, DOI 10.1103/PhysRevC.79.045804, [0903.3897](#)
- Ratzel U, Arlandini C, Käppeler F, Couture A, Wiescher M, Reifarth R, Gallino R, Mengoni A, Travaglio C (2004) Nucleosynthesis at the termination point of the s process. *Phys. Rev. C*70(6):065803, DOI 10.1103/PhysRevC.70.065803
- Rauscher T, Thielemann FK (2000) Astrophysical Reaction Rates From Statistical Model Calculations. *Atomic Data and Nuclear Data Tables* 75:1–351, DOI 10.1006/adnd.2000.0834, [arXiv:astro-ph/0004059](#)
- Reifarth R, Arlandini C, Heil M, Käppeler F, Sedyshev PV, Mengoni A, Herman M, Rauscher T, Gallino R, Travaglio C (2003) Stellar Neutron Capture on Promethium: Implications for the s-Process Neutron Density. *ApJ*582:1251–1262, DOI 10.1086/344718
- Reifarth R, Käppeler F, Voss F, Wisshak K, Gallino R, Pignatari M, Straniero O (2004) ^{128}Xe and ^{130}Xe : Testing He-Shell Burning in Asymptotic Giant Branch Stars. *ApJ*614:363–370, DOI 10.1086/422206, [arXiv:astro-ph/0405065](#)
- Sonnabend K, Mengoni A, Mohr P, Rauscher T, Vogt K, Zilges A (2003) Determination of the (n, γ) reaction rate of unstable ^{185}W in the astrophysical s-process via its inverse reaction. *Nuclear Physics A* 718:533–535, DOI 10.1016/S0375-9474(03)00835-2
- Takahashi K, Yokoi K (1987) Beta-Decay Rates of Highly Ionized Heavy Atoms in Stellar Interiors. *Atomic Data and Nuclear Data Tables* 36:375–409, DOI 10.1016/0092-640X(87)90010-6
- van Raai MA, Lugaro M, Karakas AI, García-Hernández DA (2008) Rubidium and Zirconium Production in Massive AGB Stars. In: Guandalini R, Palmerini S, Busso M (eds) *Evolution and Nucleosynthesis in AGB Stars*, American Institute of Physics Conference Series, vol 1001, pp 146–153, DOI 10.1063/1.2916957
- Vockenhuber C, Dillmann I, Heil M, Käppeler F, Winckler N, Kutschera W, Wallner A, Bichler M, Dababneh S, Bisterzo S, Gallino R (2007) Stellar (n, γ) cross sections of Hf174 and radioactive Hf182. *Phys. Rev. C*75(1):015804, DOI 10.1103/PhysRevC.75.015804
- Ward RA (1977) The Importance of Long-Lived Isomeric States in s-Process Branching. *ApJ*216:540–547
- Wisshak K, Voss F, Käppeler F, Krčička M, Raman S, Mengoni A, Gallino R (2006) Stellar neutron capture cross section of the unstable s-process branching point ^{151}Sm . *Phys. Rev. C*73(1):015802, DOI 10.1103/PhysRevC.73.015802
- Yin QZ, Lee CTA, Ott U (2006) Signatures of the s-Process in Presolar Silicon Carbide Grains: Barium through Hafnium. *ApJ*647:676–684, DOI 10.1086/505188